Characterisation of the anechoic chamber at Stellenbosch University

by

Alo-Heléne (Anneke) Bester

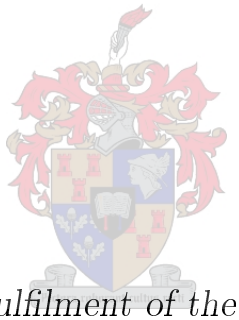

Thesis presented in fulfilment of the requirements for the degree of Master of Engineering in Electronic Engineering in the Faculty of Engineering at Stellenbosch University

Supervisor: Prof. P. Meyer

December 2019

Declaration

By submitting this thesis electronically, I declare that the entirety of the work contained therein is my own, original work, that I am the sole author thereof (save to the extent explicitly otherwise stated), that reproduction and publication thereof by Stellenbosch University will not infringe any third party rights and that I have not previously in its entirety or in part submitted it for obtaining any qualification.

Date: December 2019

Abstract

Characterisation of the anechoic chamber at Stellenbosch University

The anechoic chamber at the University of Stellenbosch is used on a weekly basis to measure and characterise antenna radiation patterns. Although excellent comparisons between measurements and simulations are achieved, the chamber itself was never characterised to establish how accurate measurements are and how large the contribution of errors is to the measurement uncertainty. The aim of this thesis is to characterise the chamber to an industry standard.

The NIST 18 term error analysis was used for this evaluation. The analysis makes use of statistical analytical methods, measurements, simulations, as well as mathematical calculations to establish the measurement uncertainties.

Errors that form part of the chamber environment and setup can influence different sections of the radiation pattern. It can either affect the radiation pattern main lobe or the sidelobes or both. During the investigation, it was determined how significant the influence of the various errors are on the different sections of the radiation pattern and how large the associated uncertainty are.

A spin-off from the study was that a mechanical calibration of the chamber setup was done and a complete guide to the calibration process is included in this document.

Uittreksel

Karakterisering van die Aneggoïese kamer van die Universiteit van Stellenbosch

(Characterisation of the anechoic chamber at Stellenbosch University)

Die aneggoïese kamer by die Universiteit van Stellenbosch word op 'n weeklikse basis gebruik om antennas te karakteriseer. Alhoewel die metingsresultate goed ooreenstem met die antenna simulasies was daar nog nooit 'n in diepte ondersoek geloods na oorsake wat die akkuraatheid van metings moontlik kan beïnvloed nie. Hierdie verhandeling se doelwit is om die kamer te karakteriseer volgens 'n industrie aanvaarde metode.

Die ondersoek maak gebruik van die NIST 18 term fout analise wat wyd aanvaar word as 'n geldige ondersoek metode. Die analise word gedoen deur statistiese analitiese metodes, metings, simulasies, asook wiskundige berekeninge om die onsekerheid in toetsresultate te kwantifiseer.

Foute wat in metings insluip kan verskillende sektore, naamlik die hoofbundel en/of die sy-lobbe van die antenna stralingspatroon beïnvloed. Daar is bepaal watter dele van 'n antenna stralingspatroon deur hierdie moontlike foute geraak word, asook hoe groot die onsekerheid is wat deur hierdie foute geïnduseer word.

'n Uitvloeiing van die ondersoek was die meganiese kalibrasie van die stelsel en 'n volledige uiteensetting van hoe so 'n kalibrasie gedoen word.

Acknowledgements

'n Tesis is nie net die student se werk nie, daar is altyd vriende, familie, kollegas en studieleiers wat agter hierdie individu staan en waarsonder dit nie moontlik sou wees om die reuse taak te voltooi nie. Ek wil graag my dank en waardering uitspreek teenoor elkeen wat 'n boodskap gestuur het, 'n woord van bemoediging geuiter het en sommer net verstaan het. Ek kan egter nie anders as om 'n paar mense uit te sonder nie.

Prof Davidson, who started me on this interesting journey. Your contribution formed the basis for the success of this thesis.

Prof Meyer, sonder jou aanmoedig en ondersteuning sou dit onmoontlik gewees het om klaar te maak. Dankie dat jy so verstommend geduldig was met jou verduidelikings waar my teorie verroes was. Jou nugter uitkyk op die lewe het gemaak dat ek nog die meeste van my varkies het.

Susan Maas, ek is so bly ek het nie hierdie paadjie alleen gestap nie. Ons gaan eendag met deernis terug dink aan hierdie tyd van klippe kou.

Alo, dat jy my heeltyd herinner het dat daar 'n begin was en 'n einde moet wees deur my aanhoudend te vra, "Hoe ver nog?".

Hanco, jou alternatiewe motiewe dat ek moet klaar maak, was vir my 'n aansporing! Nou kan ons bou!

Dankie Nicola vir al die koppies rooibostee, dit het die laat aande baie makliker gemaak.

Nico, baie dankie vir jou geduld, hulp, aanmoediging, bemoediging en natuurlik my mooi prentjies! Ek kan nie vir jou genoeg dankie sê nie. Jy is net so 'n groot anker in my lewe.

Aan my Hemelse Vader, daar is geen twyfel dat hierdie net moontlik was alleen deur U genade. Dit was 'n interessante, maar goeie paadjie waarop U my gelei het.

Contents

Declaration i

Abstract ii

Uittreksel iii

Acknowledgements iv

Contents v

List of Figures vii

List of Tables x

Nomenclature xi

1 Introduction 1
- 1.1 US chamber history . . . 1
- 1.2 Motivation . . . 3
- 1.3 Metrics evaluated . . . 3
- 1.4 Summary of results . . . 4
- 1.5 Layout of thesis . . . 5

2 Introduction to antenna measurements 6
- 2.1 Basic antenna parameters . . . 6
  - 2.1.1 Reflection coefficient . . . 6
  - 2.1.2 Gain and directivity . . . 7
  - 2.1.3 Radiation patterns . . . 10
  - 2.1.4 Polarisation . . . 12
- 2.2 Basic antenna measurement methods . . . 14
  - 2.2.1 Reflection coefficient measurement . . . 14
  - 2.2.2 Realised gain measurement methods . . . 14
  - 2.2.3 Radiation pattern measurements . . . 17
- 2.3 Introduction to error analysis . . . 22
  - 2.3.1 Measurement uncertainty . . . 22

2.3.2 Statistical analysis . . . 25
2.4 Causes of measurement errors . . . 29
2.4.1 Probe/illuminator related errors . . . 29
2.4.2 Mechanical related errors . . . 36
2.4.3 Absolute power level related errors . . . 37
2.4.4 Processing related errors . . . 38
2.4.5 RF sub-system . . . 40
2.4.6 Environmental related errors . . . 40

3 Error Analysis of US anechoic chamber 42
3.1 Probe/illuminator related errors . . . 43
3.1.1 Probe pattern correction for the SNF-scanner . . . 43
3.1.2 Probe polarisation purity . . . 46
3.1.3 Probe alignment . . . 46
3.2 Mechanical related errors . . . 47
3.2.1 The Hansen study . . . 48
3.2.2 Implication of the Hansen study on the mechanical related errors . . . 49
3.2.3 Calibration and evaluation of the US SNF-scanner . . . 50
3.3 Absolute power level related errors . . . 58
3.3.1 Gain standard . . . 59
3.3.2 Normalisation constant . . . 59
3.3.3 Impedance mismatch error . . . 60
3.3.4 Absolute gain methods evaluation and results . . . 60
3.4 Processing related errors . . . 62
3.4.1 Aliasing . . . 62
3.4.2 Measurement area truncation . . . 65
3.5 RF sub-system . . . 65
3.5.1 Receiver amplitude linearity . . . 65
3.5.2 System phase error . . . 67
3.5.3 Leakage and crosstalk . . . 70
3.5.4 Receiver dynamic range . . . 72
3.6 Environmental related errors - reflections . . . 76
3.6.1 Probe structure reflections . . . 77
3.6.2 Chamber reflection . . . 82
3.6.3 Environmental related errors - random amplitude/phase errors . . . 84

4 Conclusion 87

Bibliography 91

List of Figures

1.1 Original cylindrical near-field data acquisition system at US [1] . . 2
1.2 Spherical near-field scanner at the US Antenna Test Range 2

2.1 The connection between directivity, gain and realised gain 8
2.2 Coordinate system for antenna analysis [2] 10
2.3 Highlighting various parameters of a radiation pattern [2] 11
2.4 Different formats of a radiation pattern [2] 12
2.5 Standard set-up for gain measurements 15
2.6 Different field regions of an antenna (a slightly modified version of Balanis' figure [2]) 18
2.7 Power amplitude distribution of a Marconi X-band horn in the different field regions as described in figure 2.6 19
2.8 Outdoor far-field range geometries, drawings from IEEE Recommended Practice for Near-Field Antenna Measurements [3] 20
2.9 Data acquisition grid, drawings from IEEE Recommended Practice for Near-Field Antenna Measurements [3] 21
2.10 Two examples of different configurations of CATR's 21
2.11 Error locus 23
2.12 Upper and lower band uncertainty 24
2.13 Fix error influence on uncertainty of signal level 24
2.14 Standard deviation, highlighting the confidence level associated with σ, 2σ and 3σ 27
2.15 The effect of peak misalignment and normalisation on the calculated RMS-value of the E/S-distribution 28
2.16 Transformed far-field radiation patterns of a PNF-scan (X-band horn) with pattern and probe polarisation correction applied 32
2.17 Probe pattern influence on AUT's pattern 34
2.18 Illustration of the importance of probe correction on PNF-scans vs. SNF-scans 35
2.19 Probe alignment errors 36
2.20 SNF-scanner axis configuration 37

3.1 Probe radiation patterns of different types of probes 44

3.2 AEL 2-18 GHz horn measured with two different probes, with and without probe correction turned on 45
3.3 AEL 2-18 GHz, measured with different types of probes 46
3.4 The potential errors listed by Hansen [4] 49
3.5 Laser calibration 53
3.6 Laser mounted in chamber to calibrate the system 54
3.7 Evaluation and adjustment of pol- and ϕ-stage 55
3.8 Electrical alignment script's output - forward and reverse horizontal cut 57
3.9 Electrical alignment script results 58
3.10 Repeated measurement, difference between measurement 1 and sequential measurements 59
3.11 Comparison 2 and 3 antenna measurement method 61
3.12 EMCO Model 3115 measured and published results 62
3.13 NSI-RF-RGP10 - varied distances and methods 63
3.14 Over- and under-sampling compared with the recommended sampling density 64
3.15 The effect of data truncation in the near-field is visible in the far-field radiation patterns 66
3.16 The difference between the 360 degrees span measurement and various narrower spans 67
3.17 RX Linearity test, AEL 2-18 GHz Horn 68
3.18 Variation and standard deviation of phase over time 69
3.19 Variation and standard deviation of amplitude over time 69
3.20 Near-field-amplitude and -phase comparison of measurements 1, 2 and 3 71
3.21 Far-field pattern comparison, with near-field phase variation as source for pattern differences 72
3.22 Leakage measurements 73
3.23 System dynamic range, AEL 2-18 GHz Horn 74
3.24 System block diagram, displaying as an example the measured gain/loss values of the system at 2 GHz 75
3.25 Multiple reflections, where S is the direct signal, R the reflected signal from the Rx-antenna and R' portion of the R that is reflected from the Tx-antenna 78
3.26 Multiple reflections measurement set-up 78
3.27 Azimuth and elevation patterns of 750 MHz, 1.5 GHz and 3 GHz for an increased distance from the probe 79
3.28 Amplitude variation of various frequencies over an incremental distance of 400 mm 80
3.29 Amplitude variation at 0° and 45°, measurements were done over a distance of 400 mm with increments of 25 mm 81
3.30 The azimuth patterns with minimum and maximum amplitude at boresight. The difference between the patterns is also displayed. . . 82

3.31 Chamber reflection measurements set-up 83
3.32 Variation in the pattern with the AUT and the probe simultaneously translated by $\frac{1}{4}\lambda$ 84
3.33 Repetitive measurements to determine whether random errors are present in the system 86

List of Tables

2.1 E/S with signal level of 0 dB 26
2.2 NIST 18 term error 30
2.3 AUT probe pattern correction 33

3.1 NIST 18 term error. 43
3.2 PNA-X specification - stability over temperature 70
3.3 The measured leakage when firstly Tx-port and then the Rx-port were terminated. The associated uncertainty for the main and a -30 dB sidelobe level for each scenario are listed. 73
3.4 Measured dynamic range, a noise floor of -114 dBm is used for calculations 76
3.5 NSI2000-software output: amplitude, phase and signal-to-noise readings during the stepped attenuation measurements 77
3.6 Structure reflections 82
3.7 Chamber reflections 85

Nomenclature

Acronyms

AUT	Antenna under test
CATR	Compact antenna test range
FF	Far-field
FSL	Free space loss
FSPL	Free space path loss
HPBW	Half power beamwidth
IFBW	Intermediate frequency bandwidth
MRE	Maximum radial extent
NF	Near-field
NIST	National Institute of Standards and Technology
PDF	Power density function
PNF	Planar near-field
OEWG	Open-ended waveguide
RMS	Root mean square
SNF	Spherical near-field
S/N	Signal-to-noise ratio
SL	Sidelobe
US	University of Stellenbosch
VNA	Vector network analyser

Constants

c =	$3.00\text{x}10^{8}$ m/s
π =	3.14

Notations

Amp	Amplitude
Az	Azimuth
dB	Decibel

$dist$	Distance
El	Elevation
E/S	Error-to-signal
S/E	Signal-to-error
Rx	Receive
Tx	Transmit
σ	Standard deviation
λ	Wavelength

Chapter 1

Introduction

For antenna measurements, a number of methods are generally used. These include far-field range measurements, compact range measurements, and near-field range measurements.

Near-field scanning has been done for the last 70 years according to Yaghjian [5]. In the infant stages (1950-1961), experimental measurements with no probe correction were done. Steady progress was made during the period from 1961-1975. Probe correction was introduced and the first probe corrected near-field scan was done in 1965 at the United States of America's National Bureau of Standards. The technology was progressively transferred to research facilities and private industry. The result was that during the period of 1975-1985 more than 50 near-field scanners were built throughout the world. It was also during this time period that research on antenna near-field scanning at the University of Stellenbosch started [1][6][7].

1.1 US chamber history

The first near-field scanner at the US was built during 1984 [1]. The data acquisition was done in a cylindrical manner, with the probe moving up and down while the antenna under test was rotated. The original block diagram can be seen in figure 1.1 as it was presented at one of the first SAIEE joint symposiums on antennas and propagation and microwave theory [1].

The area in which the anechoic chamber of the University was built, was originally earmarked for a sound analysis chamber. The interest in that particular field was declining, but near-field antenna measurements, on the other hand, was an exciting and growing field of interest in the microwave and antenna community. Under the supervision of Prof John Cloete, an anechoic chamber was constructed, which included cylindrical, planar and far-field measurement capabilities.

Up until 2000, the chamber was systematically upgraded and the range capabilities were improved. This included upgrading the HP 8514B S-parameter

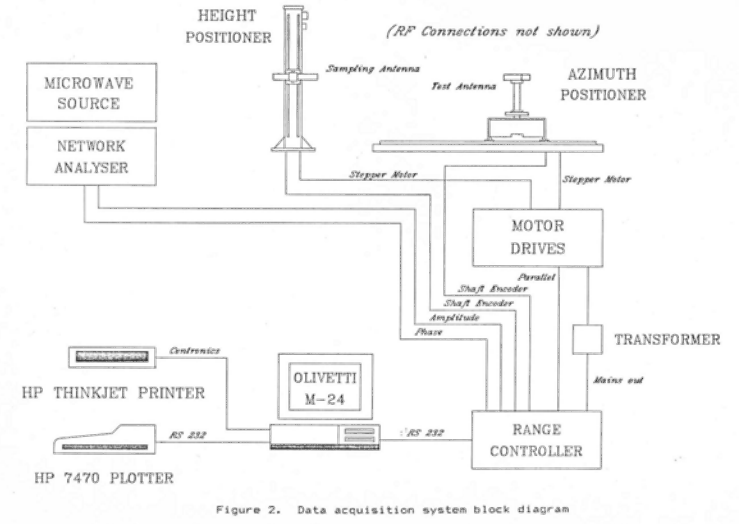

Figure 1.1: Original cylindrical near-field data acquisition system at US [1]

test set and controlling the positioner with Matlab software [1][8]. However, thereafter a time period followed in which not much investment was made in keeping up with the latest technology. This is partly due to the expensive nature of RF and microwave equipment. The measuring facility was placed in jeopardy when the HP8510 vector network analyzer (VNA), the backbone of the system, was discontinued by the manufacturer and support was ended in 2009.

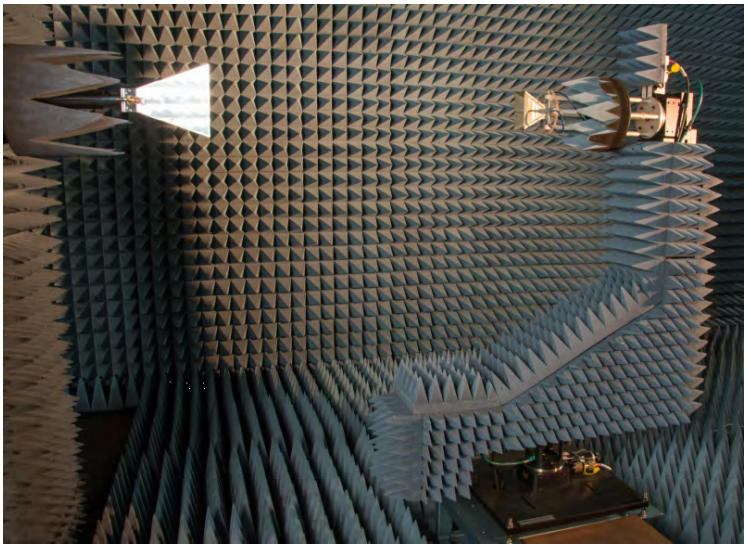

Figure 1.2: Spherical near-field scanner at the US Antenna Test Range

In 2014 funds from the National Research Foundation (NRF) became available and a significant upgrade was done by replacing the HP8510 with the

Keysight PNA-X instrument. The addition of a spherical near-field scanner opened up new measurement opportunities that were previously impossible at the US test range. Commercial software from NSI Technologies Inc. formed part of the upgrade. The process and detail of the upgrade are discussed at length in an article written by David Smith, that was published by the South African Institute of Electrical Engineers [9].

The capabilities at present include a spherical near-field scanner (SNF, shown in figure 1.2) and a planar near-field (PNF) scanner. The facility can also measure far-field pattern cuts. The frequency range covers the frequency band from 0.75 - 26.5 GHz. SNF-scans can be done over the full range, but planar near-field scans are only possible from 3.85 GHz upwards; the constraint being suitable probes for PNF-scans at the lower frequency spectrum.

1.2 Motivation

The objective of measuring an antenna in an anechoic chamber is to simulate a free-space environment. A free-space environment is an ideal space where there are no reflections from outside components. If an antenna can be measured in free-space, the antenna characteristics can be measured in isolation. This is however not the case in any measuring facility, indoors or outdoors. The accuracy of the measurement is compromised by factors such as ground reflections, chamber reflections, equipment constraints and mechanical errors [10][11][12].

Therefore, when measuring antennas in an antenna measuring range, the question of accuracy and measurement uncertainty is of prime importance. Originally, antenna measurements were done in far-field ranges, and when near-field ranges were developed, their results and accuracy were viewed with doubt. To address the problem, range assessment techniques were developed to qualify the uncertainty of measurements [10].

In the little more than thirty years existence of the antenna measuring facility at the University of Stellenbosch, a thorough investigation into the performance of the facility was never done. The motivation for this thesis is to evaluate the performance of the chamber with respect to a known industry standard. When completed, it should give confidence in measurements done at the facility and it also highlight possible limitations and problem areas that are exposed during the assessment.

1.3 Metrics evaluated

The evaluation of the measuring facility uses the U.S. National Institute of Standards and Techonology (NIST) 18-term uncertainty analysis as basis [3][10][13][14][15].

Categories of errors that are investigated are:

- Probe/illuminator related errors
- Mechanical/positioner related errors
- Absolute power level related errors
- Processing related errors
- RF sub-system related errors
- Environmental related errors

Each of these categories is broken down into possible aspects that can contribute to errors that lead to uncertainty in the measurements. The thesis chapters will take an in depth look into these parameters, and evaluate the chamber at Stellenbosch in terms of this set.

1.4 Summary of results

A short summary of the thesis results is discussed below. In all, the study, using an industry standard as a reference, showed that antennas can be measured accurately above 1.5 GHz in the anechoic chamber at Stellenbosch. As always, accurate, reliable measurements can only be made, if care is taken with the set-up and the measurement guidelines are followed.

Probe/illuminator related errors

Probe pattern related errors have potentially the biggest influence on the cross-polarisation patterns. It is observed that when there is an option between the open-ended-waveguide-probe and the wide band horn probe, NSI-RF-RGP10, the former is a better option because the beamwidth is wider and as a result has less of an influence on the results.

Mechanical related errors

It is clear from the research done that mechanical related errors have a limited effect on the measurements, but alignment is important and errors can be introduced when it is not done accurately. The converse, however, also holds true. Errors can be avoided if the mechanical alignment is done with care and precision.

Absolute power level related errors

Realised (not relative) gain is measured at the US measuring facility. Consequently, only the normalisation constant error term from the NIST18-term

error analysis is applicable to the evaluation, and it has very little influence on the outcome of the gain. The absolute gain measurements using the two- and three-antenna method were investigated and it can be concluded that the gain level can be measured within 1 dB of the published gain values of the antenna under test.

Processing related errors

Process related errors do not contribute to uncertainty in the measurements as long as the aliasing and area truncation requirements are adhered to.

RF sub-system

The investigation into the RF sub-system highlighted two important aspects. The first is that phase stability is a critical aspect when data acquisition is done. The results are much more sensitive to phase changes than amplitude changes. The second point of interest is that it is necessary to add an amplifier when the frequency is above 8.2 GHz to increase the dynamic range.

Environmentally related errors

It can be concluded that structural reflections are by far the largest contributor to uncertainty and at the lower the frequency the more so. We recommend that spherical near-field scans are not done for antennas with an operating frequency below 1.5 GHz. If this recommendation is ignored and a SNF-scan is attempted, it would be wise to increase the separation distance between the mounting structures.

1.5 Layout of thesis

The objective of this thesis is to analyse the performance of the antenna measuring facility of the University of Stellenbosch. In chapter 2 some basic antenna theory and definitions are included to help the reader to follow the rest of the dissertation. In the same chapter, a general overview of error analysis and causes of measurement errors are given as background information.

In chapter 3, the NIST18-term error analysis test results are presented and discussed. In some instances where tests were not applicable, alternative procedures were presented and performed in order to do a comprehensive assessment of the measuring facility.

The last chapter summarises the results of the NIST18-term error analysis and gives concluding remarks.

Chapter 2

Introduction to antenna measurements

Antennas form integral parts of communication systems. Different applications need different types of antennas and there is a wide range of antenna designs available. A development procedure will typically take the following steps: The purpose and application of the antenna will be considered; Antenna types, that meet the application will be examined; Polarisation, directivity and gain will be taken into account. When the options are narrowed down, a design will be done using available software packages. While analysis software has become very accurate, the final step in any antenna design is the verification through measurement. The above mentioned parameters can be measured very accurately using a combination of a calibrated vector network analyser and an anechoic room.

The following chapter will give an overview of antenna parameters and basic measurement methods. The area of error analysis and causes of measurement errors will also be explored.

2.1 Basic antenna parameters

The following parameters are some of the most important parameters to quantify an antenna: gain, directivity, radiation patterns, polarisation, and reflection coefficient.

2.1.1 Reflection coefficient

Within systems it is important that power is transferred efficiently from one subsystem to the next. Effective power transfer takes place when the input impedance of an antenna and the impedance of the system match. The IEEE antenna standard definitions [16] state that **input impedance (of an antenna)** is "The impedance presented by an antenna at its terminals." The

reflection coefficient, Γ is given by the following formula:

$$\Gamma = \frac{Z_{IN} - Z_o}{Z_{IN} + Z_o} \tag{2.1.1}$$

where Z_{IN} is the input impedance and Z_o is the system impedance. For example, if the system impedance is 50Ω and the input impedance is 75 Ω, a reflection coefficient of -0.2 result. Such a level of reflection has the following influence:

Return loss:

$$\begin{aligned} RL|_{dB} &= -20log_{10}|\Gamma| \\ &= 13.98\, dB \end{aligned}$$

Transmission loss:

$$\begin{aligned} TL|_{dB} &= -10log_{10}(1 - |\Gamma|^2) \\ &= 0.18\, dB \end{aligned}$$

Power reflected:

$$\begin{aligned} P_R|_{\%} &= 100|\Gamma|^2 \\ &= 4\% \end{aligned}$$

Power transmitted:

$$\begin{aligned} P_T|_{\%} &= 100|1 - |\Gamma|^2| \\ &= 96\% \end{aligned}$$

This example makes it clear that an impedance mismatch can have a large influence in the overall performance of a system.

2.1.2 Gain and directivity

Absolute gain and directivity are interdependent and the difference between them is the loss in the system. The dependency is displayed in figure 2.1.

For further clarification on figure 2.1, the IEEE definitions [16] for parameters are repeated below.

Directivity of an antenna in a given direction: "The ratio of the radiation intensity in a given direction from the antenna to the radiation intensity averaged over all directions.

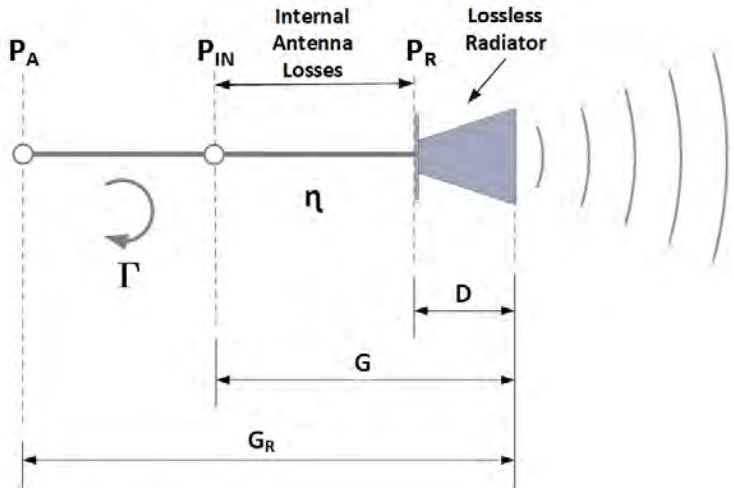

Figure 2.1: The connection between directivity, gain and realised gain

The labels in figure 2.1 are:
P_A: Power available
P_{IN}: Power accepted by antenna
P_R: Power radiated by antenna
Γ: Reflection coefficient
η: Radiation efficiency
D: Directivity
G: Absolute gain
G_R: Realised gain

NOTE 1 The average radiation intensity is equal to the total power radiated by the antenna divided by 4π.

NOTE 2 If the direction is not specified, the direction of maximum radiation intensity is implied."

Absolute gain or gain in a given direction: "The ratio of the radiation intensity in a given direction to the radiation intensity that would be produced if the power accepted by the antenna was isotropically radiated.

NOTE 1 Gain does not include losses arising from impedance and polarisation mismatches and does not depend on the system to which the antenna is connected.

NOTE 2 The radiation intensity corresponding to the isotropically radiated power is equal to the power accepted by the antenna divided by 4π.

NOTE 3 If an antenna is without dissipative loss, then in any given direction its gain is equal to its directivity.

NOTE 4 If the direction is not specified, the direction of maximum radiation intensity is implied.

NOTE 5 The term absolute gain is used in those instances where added

emphasis is required to distinguish gain from relative gain: for example, absolute gain measurements."

Realised gain: "The gain of an antenna reduced by its impedance mismatch factor."

Impedance mismatch factor: "The ratio of the power accepted by an antenna to the power incident at the antenna terminals from the transmitter.
NOTE 1 The impedance mismatch factor is equal to one minus the magnitude squared of the input reflection coefficient of the antenna."

Radiation efficiency: "The ratio of the total power radiated by an antenna to the net power accepted by the antenna from the connected transmitter."

Directivity has the characteristic that it can be calculated from the spherical pattern of the antenna. Gain on the other hand must be measured separately.

Absolute gain is always smaller than directivity as can be seen in figure 2.1. The difference between the two parameters is the efficiency of the antenna. An efficiency of less than 100% is caused by losses in the antenna.

Realised gain is in most instances a more desirable parameter than absolute gain, because internal loss is difficult to measure in isolation. Realised gain takes the internal loss, as well as the transmission loss from the impedance mismatch into account. The realised gain therefore can be measured. This is done with a separate measurement from pattern measurements, such as the gain replacement or absolute gain measurement methods. This is discussed at length in section 2.2.2.

When considering directivity and gain, it is also important to take note of the concept of partial directivity and partial gain. Partial directivity/gain is the result of antenna polarisation (an in-depth explanation of polarisation is given below). To accommodate the term partial directivity, the IEEE definition of directivity is rewritten as: "**Directivity, partial (of an antenna for a given polarisation):** In a given direction, that part of the radiation intensity corresponding to a given polarisation divided by the total radiation intensity averaged over all directions." To calculate the total directivity or gain, the sum of the partial directivity/gain for any two orthogonal polarisations can be done. This is especially relevant for antennas where the cross-polarisation component is large with regards to the co-polarised component as in the case of circularly polarised antennas.

2.1.3 Radiation patterns

The IEEE definition [16] for **radiation pattern (antenna patterns)** is the following: "The spatial distribution of a quantity that characterises the electromagnetic field generated by an antenna." The pictures used in this section are taken from Balanis' Antenna Theory [2]. A standard coordinate system that is used to describe antenna patterns is shown in figure 2.2. This is also the coordinate system that is applicable to the radiation patterns produced at the measuring facility of the University of Stellenbosch.
The radiation pattern is a graphical representation of the distribution of either the amplitude of the electric field at a constant radius or the amplitude of the power density at a constant radius. In the case of a reciprocal antenna, the distribution of how susceptible the antenna is to receive energy would be the same as for the radiation pattern for how energy is distributed when the antenna is used as a transmit antenna.
In figure 2.3a the power amplitude distribution is displayed in a three-dimensional format. Two-dimensional cuts can be seen in figure 2.4. The amplitude plot of the electric field (2.4a) and the power distribution (2.4b) are displayed in a two-dimensional format. It is common to display the power pattern in logarithmic-scale [dB]. By doing this, small differences in patterns can be highlighted. It is also standard practice to normalise the patterns to their maximum peak value.

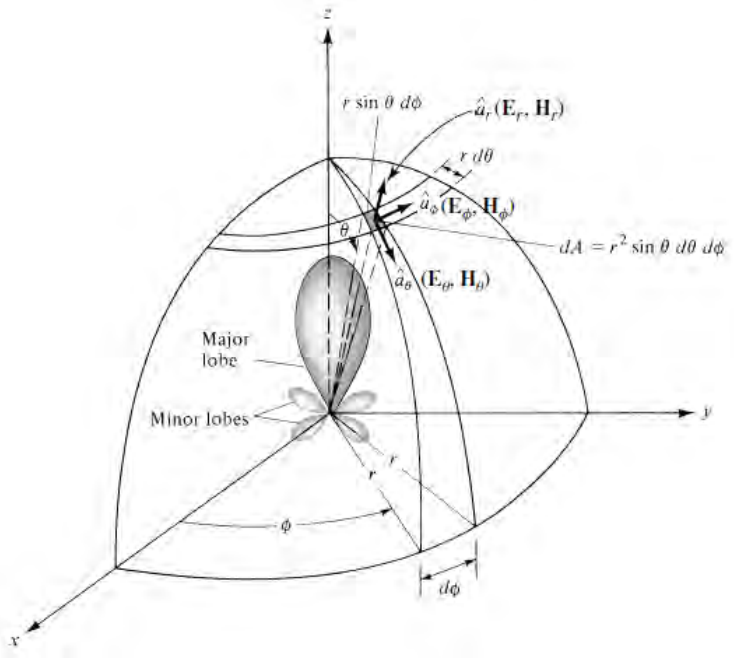

Figure 2.2: Coordinate system for antenna analysis [2]

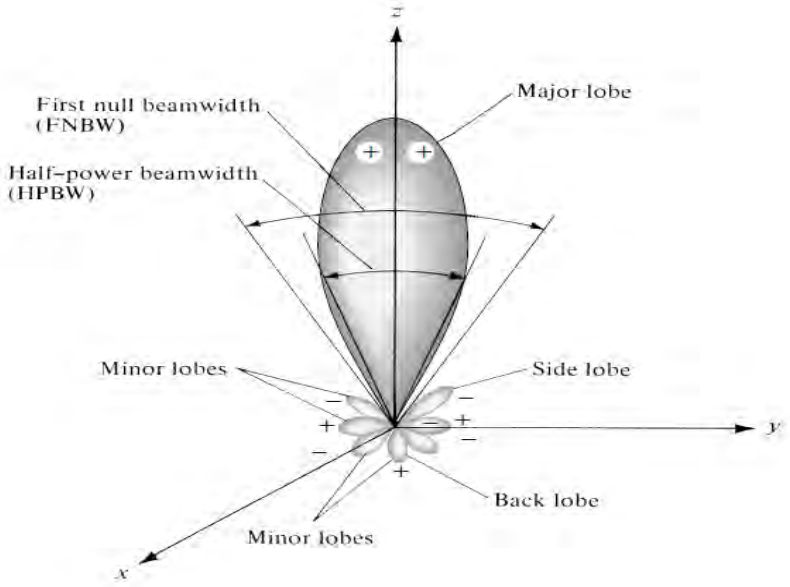

(a) 3D representation of antenna patterns

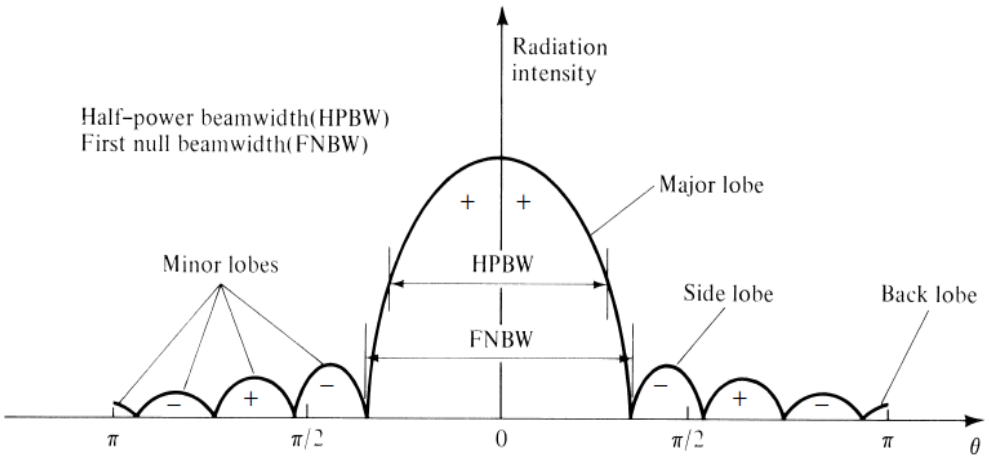

(b) Cartesian plot of an antenna pattern cut

Figure 2.3: Highlighting various parameters of a radiation pattern [2]

Typical information obtained from a radiation pattern is the half-power beamwidth (HPBW), the position of the nulls in the pattern and also the sidelobe level, as shown in figure 2.4. It is important to note that the half-power beamwidth, which is measured in degrees, is the same in all three plots. The main lobe of the antenna pattern contains the most energy. In most cases it is desirable that the sidelobes (the smaller lobes) be as low as possible in relation to the main beam. Radiation pattern cuts can also be plotted as either cartesian plots, as seen in figure 2.3b or as polar plots, as seen in figure 2.4. The same information is displayed in different formats, depending on the application or preference of the interested party.

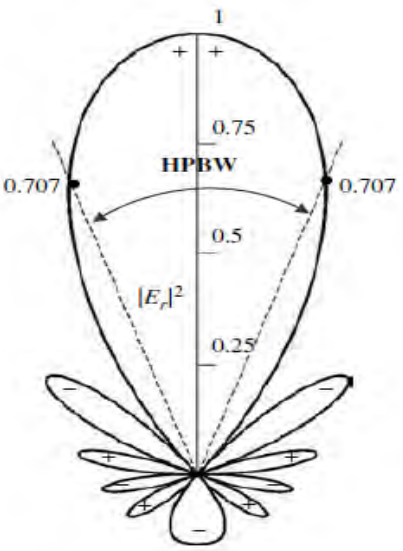

(a) Field pattern, linear scale

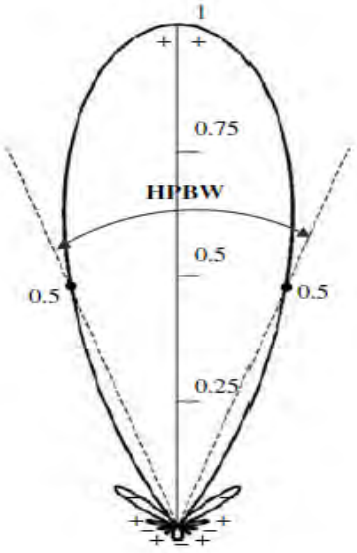

(b) Power pattern, linear scale

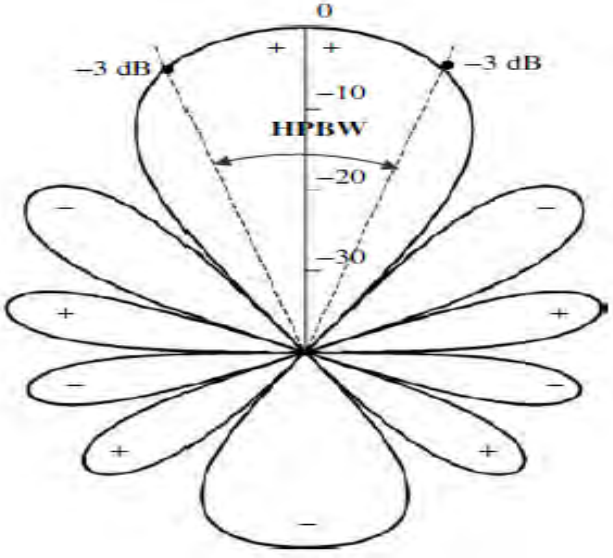

(c) Power pattern [dB]

Figure 2.4: Different formats of a radiation pattern [2]

2.1.4 Polarisation

Polarisation of a wave refers to the direction of the electric field vector. When the vector is fixed in a specific orientation, the wave polarisation is defined as linear [17].

The IEEE standard definition for antenna terms [16] defines **wave polarisation** as follows: "Polarisation of a wave radiated by an antenna in a specified direction: In a specified direction from an antenna and at a point in its far field, the polarisation of the (locally) plane wave that is used to represent the

radiated wave at that point."
The total electric field for a wave travelling in the positive z-direction can be written as:

$$\bar{E} = (E_1\hat{x} + E_2\hat{y})e^{-jk_0z} \tag{2.1.2}$$

When we consider the above equation it is easy to explain the different types of polarisation. In the case when E_1 and E_2 are both real, the polarisation would be linear. If either E_1 or $E_2 = 0$, the wave is linearly polarised and aligned either with $\hat{x}$ or $\hat{y}$. This would be a horizontally- or vertically polarised antenna. The polarisation of antennas are in some cases slanted. The angle at which the polarisation of the antenna is tilted can be calculated with:

$$\phi = tan^{-1}\Big(\frac{E_2}{E_1}\Big) \tag{2.1.3}$$

If $E_1 = +jE_2 = E_0$ and E_0 is real and positive, we can rewrite equation 2.1.2 as

$$\begin{aligned}\bar{E} &= (E_1\hat{x} + E_2\hat{y})e^{-jk_0z} \\ &= E_0(\hat{x} - j\hat{y})e^{-jk_0z}\end{aligned}$$

In the time domain this is

$$\bar{\mathcal{E}}(z,t) = E_0\Big[\hat{x}cos(\omega t - k_0z) + \hat{y}cos(\omega t - k_0z - \frac{\pi}{2})\Big]$$

At $z = 0$ the equation simplifies to

$$\bar{\mathcal{E}}(z,t) = E_0\Big[\hat{x}cos(\omega t) + \hat{y}sin(\omega t)\Big] \tag{2.1.4}$$

The electrical field vector in equation 2.1.4 represent a circularly polarised wave with an angular velocity of ω. Depending on whether $E_2 = +j$ or $-j$, the wave would be left- or right-hand polarised respectively. An elliptical polarisation would occur when $|E_1| \neq |E_2| \neq 0$.

A travelling wave's polarisation in the far-field is defined by the antenna's polarisation. Therefore, if the travelling wave is linearly polarised, the transmitting antenna is also be linearly polarised. In the same way a right-hand circular polarised antenna launches a right-hand circular wave into free-space. The orientation of the antenna polarisation would also be identical to the orientation of the E-field of the travelling wave. A linearly polarised antenna, mounted horizontally, produces a horizontal linear polarised wave.
The IEEE standard definition [16] for **antenna polarisation** is: "In a given

direction from the antenna, the polarisation of the wave transmitted by the antenna. *Note:* When the direction is not stated, the polarisation is taken to be the polarisation in the direction of maximum gain."

The concepts of co- and cross-polarisation are important when antenna measurements are done. If the polarisation of two antennas, i.e. the probe and the AUT (antenna under test) align, the measurement is called a co-polarised measurement. This results in maximum power transfer. If one of the two antenna's polarisations is orthogonal to that of the other, the least amount of power transfer takes place. This orientation of these antennas' polarisation with respect to each other is referred to as cross-polarised.

2.2 Basic antenna measurement methods

2.2.1 Reflection coefficient measurement

Reflection coefficients can be measured with a vector network analyser (VNA). A network analyser has the ability to measure the transmitted and reflected waves from a network and is able to calculate and display the scattering matrix of the device under test. In the case of antenna measurements, the reflection coefficient is the primary measurement of interest.

Accurate measurements are possible because the VNA applies error correction to compensate for internal errors such as directional coupler mismatch, imperfect directivity and reflection tracking.

2.2.2 Realised gain measurement methods

There are basically two types of measurement that can be carried out to determine the gain of an antenna. The first method is the gain replacement method, while the second is the absolute gain method.

The gain replacement method is used when a calibrated antenna is available. To characterise standard gain antennas, the absolute gain method is used, because one does not need any prior knowledge of the antenna measured. Absolute gain measurements are considered the most accurate way to determine the gain of an antenna. It is, however, the most time-consuming method. According to Balanis [2], the most suitable antennas to use as standard gain antennas are $\frac{1}{2}\lambda$ dipoles and pyramidal horn antennas. The dipole has good polarisation purity, which is a requirement for standard gain antennas, but a dipole's beamwidth is wide which may have an influence on the measurement if the measurement is not done in a free-space environment. The standard gain horn, commonly referred to as a "standard horn", on the other hand, has a somewhat elliptical axial ratio and the cross-polarisation com-

ponent might influence the measurement, but since it has a highly directive beam, the environment plays less of a role in the measurement.

As previously stated, a gain replacement measurement can only be done, when one has a standard gain antenna. The measuring facility at the University of Stellenbosch does not have any standard gain antennas to utilise for these type of measurements, and although the software of the measuring facility has the capability of implementing the gain replacement technique it is, therefore not possible to perform such a measurement at present.

As an improvement to our in-house capabilities, it is proposed that where possible the probe antennas are measured with great precision, using the three-antenna gain method and used as standard gain antennas. If the replacement method is used instead of the three-antenna gain method, it would be much less time-consuming.

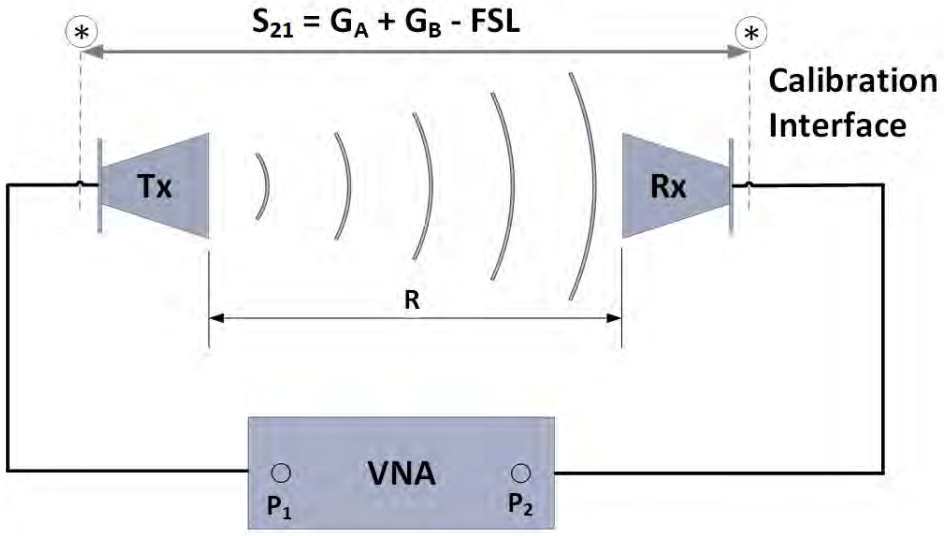

Figure 2.5: Standard set-up for gain measurements

To perform an absolute gain measurement it is required that the separation distance between the two AUT's be large enough that the measurements are done in the far-fields of both of the antennas. The far-field distance is calculated using equation 2.2.1, where R is the far-field distance and D the largest structural dimension of the two AUT's.

$$R \geq \left(\frac{2D^2}{\lambda}\right) \tag{2.2.1}$$

The absolute gain methods are based on the Friis transmission formula, equation 2.2.3. The Friis formula consists of the following components: the gain of each antenna, (G_A and G_B), the relation of the receive power to the

transmit power ($\frac{P_{Rx}}{P_{Tx}}$, the S21-parameter measured) and the free-space loss (FSL, equation 2.2.2).

$$FSL = \left(\frac{\lambda}{4\pi R}\right)^2 \tag{2.2.2}$$

$$\frac{P_{Rx}}{P_{Tx}} = \left(\frac{\lambda}{4\pi R}\right)^2 G_A G_B \tag{2.2.3}$$

We can rewrite the equation expressed in dB as:

$$\begin{aligned} S21|_{dB} &= 10log(\tfrac{\lambda}{4\pi R})^2 + G_A|_{dB} + G_B|_{dB} \\ G_A|_{dB} + G_B|_{dB} &= S21|_{dB} - 20log(\tfrac{\lambda}{4\pi R}) \\ G_A|_{dB} + G_B|_{dB} &= S21|_{dB} + 20log(\tfrac{4\pi R}{\lambda}) \end{aligned} \tag{2.2.4}$$

Equation 2.2.4 form the basis of the gain calculations when the two- and three-antenna gain method is used.

The two-antenna gain method can only be used when two identical antennas are available. Equation 2.2.4 then reduces to the following:

$$Gain|_{dB} = \frac{S21|_{dB} + 20log(\frac{4\pi R}{\lambda})}{2} \tag{2.2.5}$$

If two identical antennas are not available, a three-antenna gain method can be used to determine the gain. Three-antenna gain method measurements are done by pairing the antennas in unique combinations. For each combination, the distance between the antennas must be measured and the free space loss calculated separately. The measurement results in three Friis equations, with three unknown gains. If the dB-units of equation 2.2.4 are omitted for clarity, it simplifies to:

$$G_A + G_B = S21_{AB} + 20log(\tfrac{4\pi R_{AB}}{\lambda})$$

The loss of each measurement can be combined as follows:

$$\begin{aligned} Loss_{AB} &= S21_{AB} + 20log(\tfrac{4\pi R_{AB}}{\lambda}) \\ Loss_{AC} &= S21_{AC} + 20log(\tfrac{4\pi R_{AC}}{\lambda}) \\ Loss_{BC} &= S21_{BC} + 20log(\tfrac{4\pi R_{BC}}{\lambda}) \end{aligned}$$

The three-antenna gain method equations can be written as:

$$\begin{aligned} G_A + G_B &= Loss_{AB} \quad (1) \\ G_A + G_C &= Loss_{AC} \quad (2) \\ G_B + G_C &= Loss_{BC} \quad (3) \end{aligned}$$

Rewrite (1) as:

$$G_A = Loss_{AB} - G_B \tag{4}$$

Substitude (4) into (2):

$$Loss_{AB} - G_B + G_C = Loss_{AC} \tag{5}$$

Rewrite (5) as:

$$-G_B + G_C = Loss_{AC} - Loss_{AB} \tag{6}$$

Add (3) and (6):

$$\begin{aligned} 2G_C &= Loss_{BC} + Loss_{AC} - Loss_{AB} \\ G_C &= \frac{1}{2}(Loss_{BC} + Loss_{AC} - Loss_{AB}) \end{aligned} \tag{7} \qquad (2.2.6)$$

Substitute (7) into (3) and (1), the gain is given by:

$$G_B = Loss_{BC} - G_C \tag{2.2.7}$$

$$G_A = Loss_{AB} - Loss_{BC} + G_C \tag{2.2.8}$$

Equations 2.2.6 - 2.2.8 solve the three unknown gains of the three antennas used in the measurement.

2.2.3 Radiation pattern measurements

Three field regions can be identified around an antenna, namely the reactive near-field, the radiating near-field and the far-field region. This is illustrated in figure 2.6.

According to the standard definitions of terms for antennas [16], the **reactive near-field region** is "the portion of the near-field region immediately surrounding the antenna wherein the reactive field predominates."

The **radiating near-field region** is "the portion of the near-field region of an antenna between the far field and the reactive portion of the near-field region, wherein the angular field distribution is dependent upon the distance from the antenna."

Lastly the **far-field region** is defined as "the region of the field of an antenna where the angular field distribution is essentially independent of the distance from a specified point in the antenna's region."

The general accepted formulas for an indication of where the boundaries occur are:

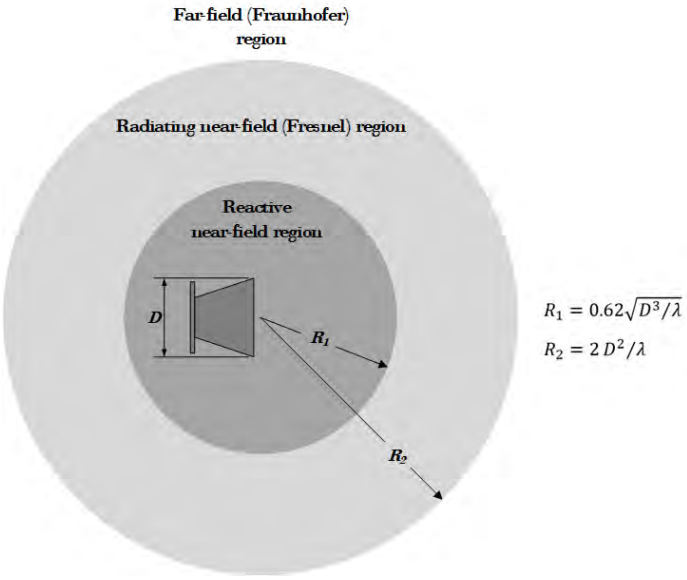

Figure 2.6: Different field regions of an antenna (a slightly modified version of Balanis' figure [2])

$$R_1 = 0.62\sqrt{\frac{D^3}{\lambda}} \tag{2.2.9}$$

$$R_2 = \frac{2D^2}{\lambda} \tag{2.2.10}$$

where D is the largest dimension of the antenna.

Figure 2.7 shows the magnitude of the E-field on a cross-section perpendicular to the direction of propagation, at different distances from the source. In this case, the source is a 80 mm x 80 mm horn. The transitions between the various regions are not abrupt, but are significantly different in each one. Figures 2.7a and 2.7b show that the amplitude field distribution is mainly located at the aperture of the horn. The amplitude drops sharply outside the 80 mm region. As the observation distance increases, the radiating area enlarges and the amplitude taper is less severe (figure 2.7c and 2.7d). At the stage where the distance is large enough for the field to be considered far-field, the distance from the antenna has no influence on the field distribution, and the shape of the radiation pattern remains the same as seen in figures 2.7e and 2.7f.

Antenna radiation patterns are measured at antenna test ranges. There are many different types of test ranges that can be classified into different categories. These categories include indoor and outdoor ranges, near-field and far-field ranges, and also reflective, free-space and compact ranges.

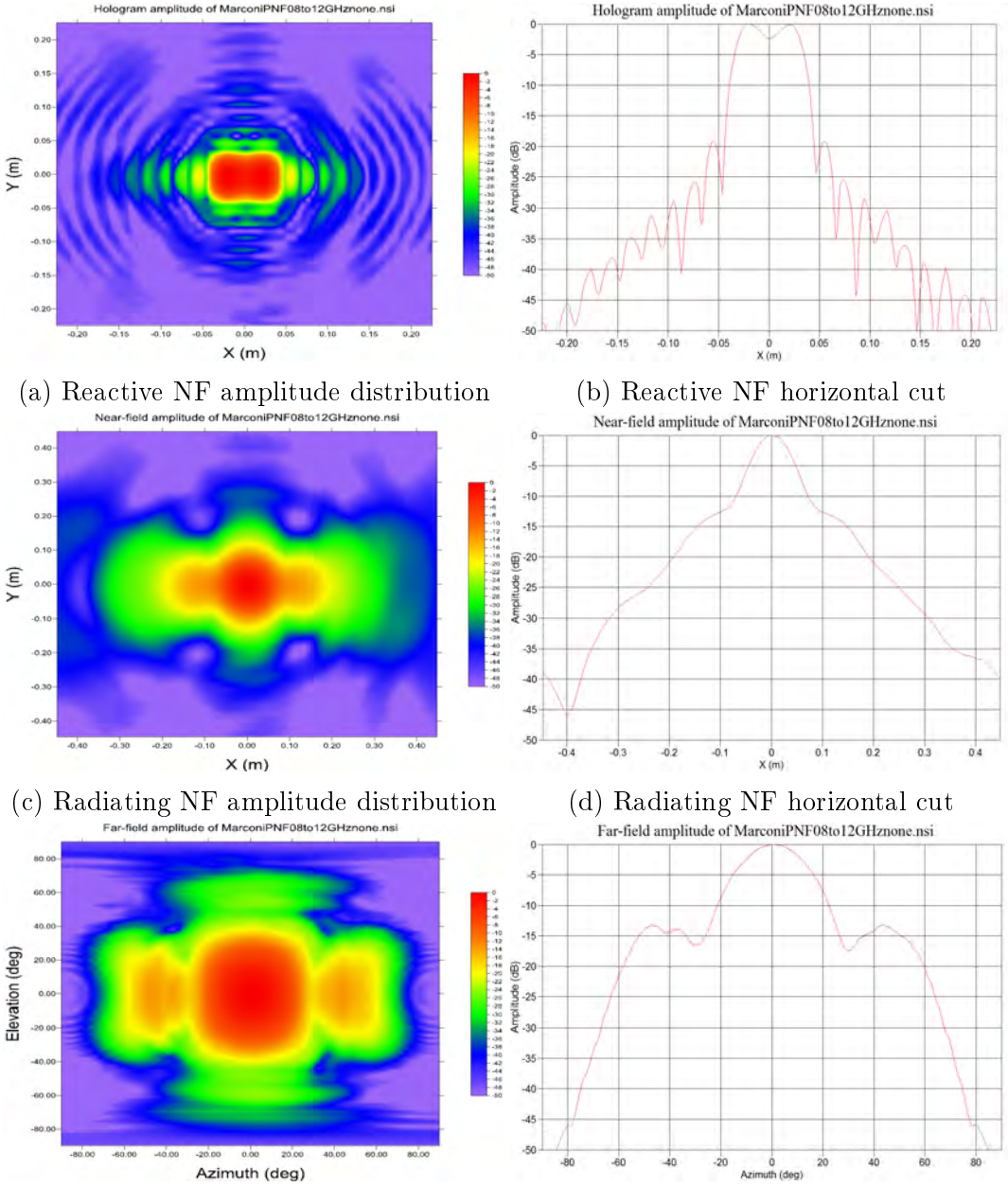

(a) Reactive NF amplitude distribution

(b) Reactive NF horizontal cut

(c) Radiating NF amplitude distribution

(d) Radiating NF horizontal cut

(e) FF amplitude distribution

(f) FF horizontal cut

Figure 2.7: Power amplitude distribution of a Marconi X-band horn in the different field regions as described in figure 2.6

For the purpose of this discussion, the ranges will be divided into the main categories of near- and far-field ranges, with some additional properties from other categories highlighted.

Far-field range characteristics are such that the separation distance between the probe and AUT's is large enough that the AUT is mounted in the far-field of both the AUT and the probe. The far-field implies that the AUT radiation

pattern does not change with added distance. Figure 2.8 shows two types of far-field ranges, a reflective and a slant range. Both these antenna ranges are also outdoor ranges.

There is however a major difference in the design strategy of these two ranges. The reflective range is carefully designed to create an area in which there constructive interference from the signal that is reflected from the ground. This produces an approximate plane wave in the area were the AUT is measured. This area is referred to as a quiet zone [18]. A different approach is applied to the slant range, where the reflections from the ground are minimised by pointing the first null of the source antenna's radiation pattern to the ground. This type of range is called a free-space range and it simulates a free-space environment. The goal of a free-space range is to create a region in space where the influence of the surrounding environment on the measurement is minimised [2].

Another way of attempting to create a free-space environment is the anechoic chamber. Anechoic chambers are indoor ranges which are lined with absorbing material. In anechoic chambers, both near- and far-field measurements can be performed. Refer to Balanis' handbook on antenna theory [2] or the IEEE standard for antenna measurements [18] for a comprehensive study of the different types of anechoic chambers.

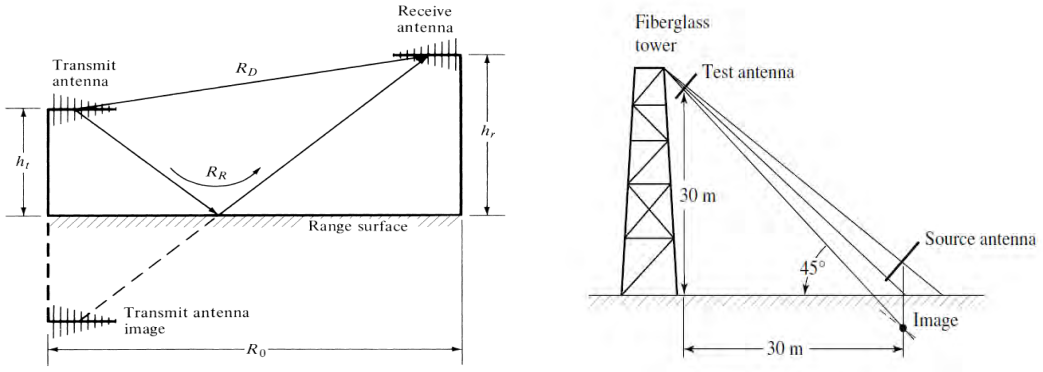

(a) Reflective range (b) Slant range

Figure 2.8: Outdoor far-field range geometries, drawings from IEEE Recommended Practice for Near-Field Antenna Measurements [3]

Near-field ranges differ from far-field ranges because the measurement can be done in the near-field of the antenna under test. The measured near-field pattern is then mathematically transformed to the far-field pattern. The separation distance between the probe and the AUT is consequently vitally important because the field distribution has not settled and is changing with increased distance[2]. The distance parameter forms part of the mathematical transformation of the pattern from the near-field to the far-field.

The most common near-field ranges are: planar scanners, where the data is acquired over a flat surface, in a rectangular grid; cylindrical scanners, where the data acquisition surface is bent around the antenna in the form of a cylinder; and spherical scanners, with data acquired on a spherical surface. These three near-field scanners, with the different data acquisition patterns, are presented in figure 2.9.

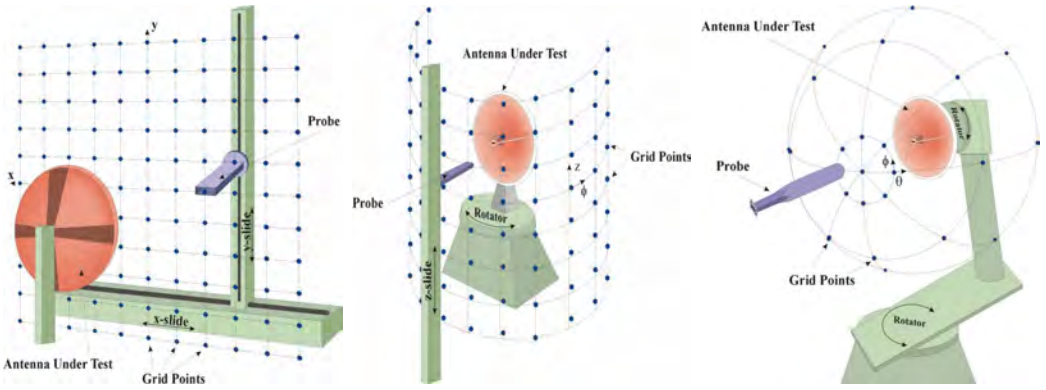

(a) Planar near-field (b) Cylindrical near-field (c) Spherical near-field

Figure 2.9: Data acquisition grid, drawings from IEEE Recommended Practice for Near-Field Antenna Measurements [3]

A type of range that combines both the free-space environment and far-field topology, is a compact antenna test range (CATR). To imitate the far-field conditions, where a uniform plane wave illuminates the AUT, a parabolic reflector is utilised as seen in figure 2.10. Because of this configuration, the size of the range reduces to much smaller than a traditional outdoor range and therefore the free-space environment can be achieved by placing the AUT, source antenna and the reflector in an anechoic chamber [2].

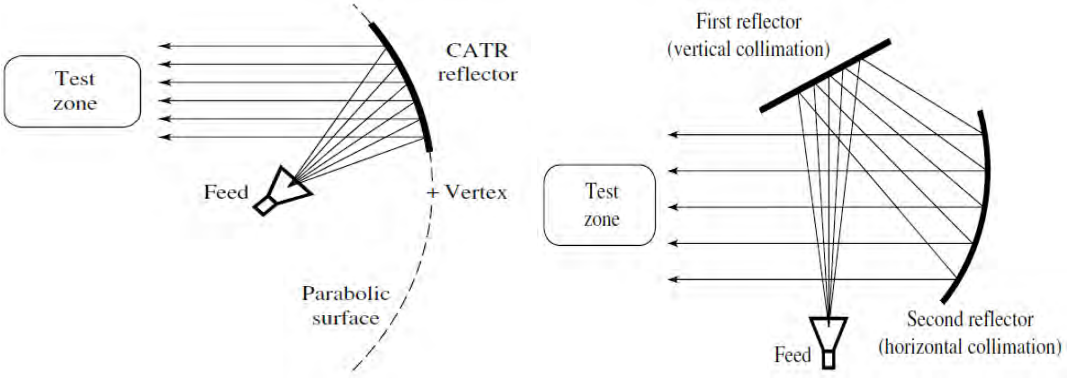

Figure 2.10: Two examples of different configurations of CATR's

There is not an antenna measuring range that is an ideal solution for all circumstances. Far-field, outdoor ranges, can accommodate a large number of different types of antennas, especially with regards to size and weight, but because it is outdoors it makes it more susceptible to conditions, such as weather, vegetation, and the local wildlife [2][10]. Large areas are needed to build such a facility. The National Antenna Test Range (NATR), north of Pretoria has a microwave range of 500 m [19], but even the extended range would in some instances not give enough distance to be able to perform far-field measurements for some antennas. For example, if an antenna's largest dimension is 3 m and the operating frequency is 10 GHz, the far-field distance is calculated as 600 m. This problem can be solved by doing near-field measurements.

Near-field ranges, however, are expensive and the software to do the measurement and near- to far-field transformation is complex. The mechanical operation and data acquisition must be synchronised and can be complicated. The positional accuracy and repeatability are also of extremely high importance. The controlled environment has, nevertheless, big advantages over the outdoor ranges.

Every measurement is unique and the type of measurement suited for the AUT depends on the antenna's operating frequency, physical size and weight, and sometimes even on the structural strength of the antenna.

2.3 Introduction to error analysis

When any measurement is done there is always uncertainty associated with the measurement. This section explains the origin of uncertainty, and will derive formulas to calculate uncertainty. A statistical tool is presented that can be used to evaluate and compare measurements in order to derive the uncertainty. In the IEEE document, Recommended Practice for Near-Field Antenna Measurements [3] it is stated that, "Without a statement of uncertainty, measurement results cannot be compared. Thus, a measurement is not truly complete without a statement of uncertainty."

2.3.1 Measurement uncertainty

The methodology for the uncertainty measurements are described in multiple sources, but the references that were primarily consulted here were Theory and Practice of Modern Antenna Range Measurements by Parini et al. [10] and IEEE's Recommended Practices for Near-Field Antenna Measurements [3].

A self-comparison approach is taken whereby one parameter at a time is changed and notable differences in the pattern are observed. We can assume that differences are the result of a change in the set-up and therefore we can calculate an error.

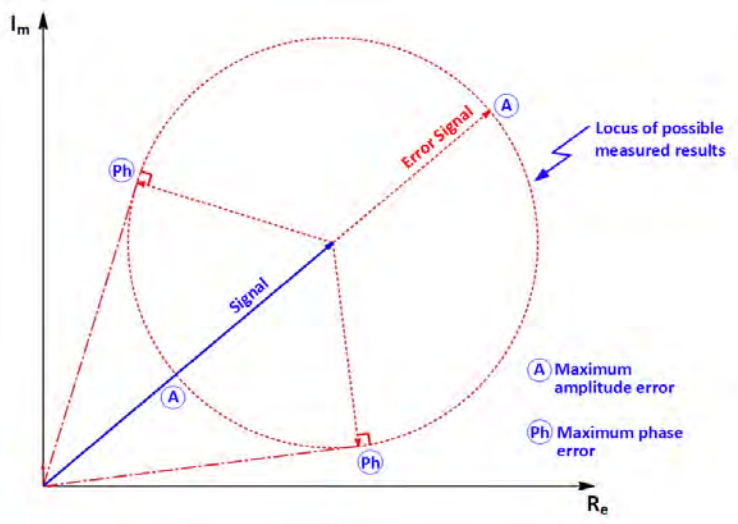

Figure 2.11: Error locus

When measuring a signal, the biggest error in amplitude occurs when the signal is in phase or 180° out of phase with the error, as can be seen in figure 2.11. The error vector describes an area of uncertainty around the measured value. The maximum and minimum magnitude of a measured value can be expressed in terms of the true magnitude of the signal (S) and the magnitude of the error (E). It can be expressed in dB as both S and E are referenced to a 1 V signal, the error (E) is assumed to be smaller than S, the signal.

$$Measured|_{dB} = 20log(S \pm E) \tag{2.3.1}$$
$$= 20log(S \pm \frac{S}{S/E})$$
$$= 20log(S) + 20log(1 \pm \frac{1}{S/E}) \tag{2.3.2}$$

Here, the two values of "Measured" are the minimum and the maximum measured values. The first term is the actual signal and the second term the error component of the measurement. Uncertainty can therefore be defined as the minimum and the maximum error.

$$Uncertainty|_{dB} = 20log(1 \pm 10^{-\frac{S/E(dB)}{20}}) \tag{2.3.3}$$

The largest phase error occurs between a tangential line on the locus of the area of uncertainty and the signal measured, as can be seen in figure 2.11. The maximum phase error can be calculated with:

$$\theta_{Max} = \pm arcsin(E/S) \tag{2.3.4}$$

These formulas can be used to create an envelope around measured data to indicate the uncertainty. When a measurement envelope is displayed on the

graph, we can assume that the true value lies within the envelope's boundaries. The upper- and lowerbound uncertainties are plotted in figure 2.12.

$$Upperbound|_{dB} = 20log(1 + 10^{-\frac{S/E|_{dB}}{20}}) \tag{2.3.5}$$

$$Lowerbound|_{dB} = 20log(1 - 10^{-\frac{S/E|_{dB}}{20}}) \tag{2.3.6}$$

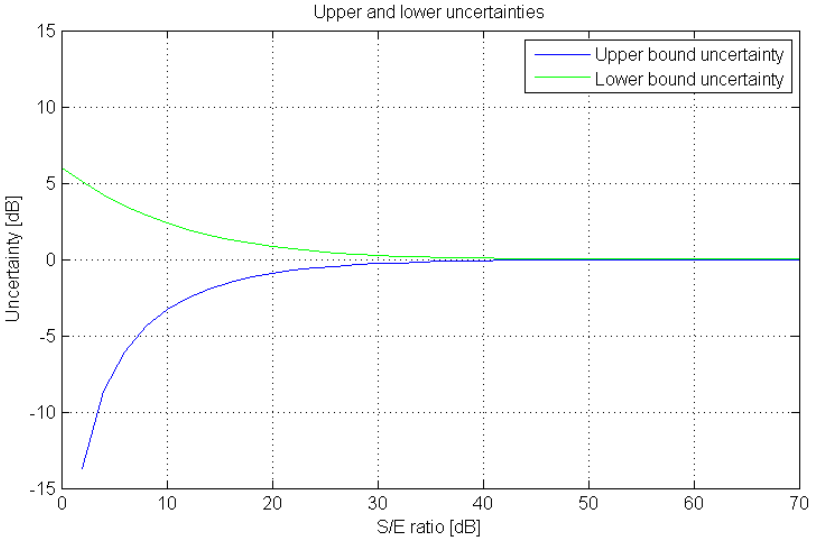

Figure 2.12: Upper and lower band uncertainty

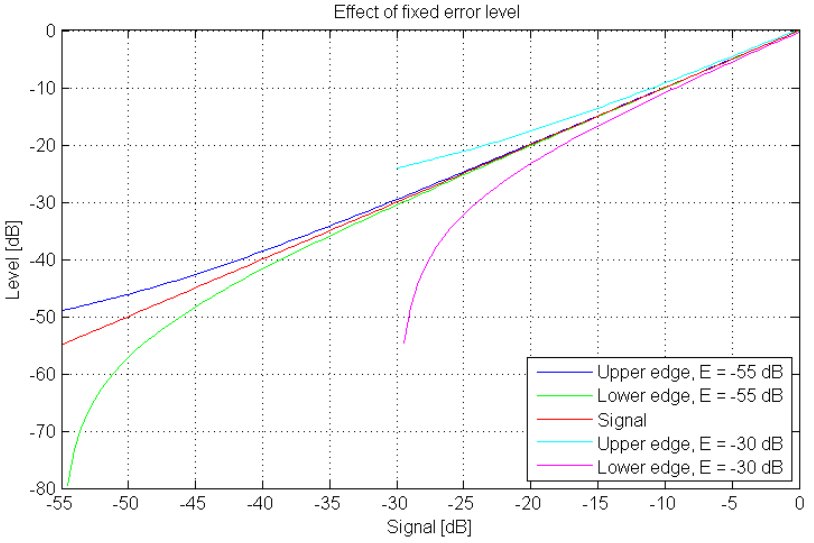

Figure 2.13: Fix error influence on uncertainty of signal level

It is also important to note that when the signal level decreases, the uncertainty increases for a fixed error level. This is illustrated in figure 2.13.

The inverse to S/E-ratio can also be used and for the remainder of this thesis this will be done. The E/S-ratio has a negative dB value. The term becomes increasingly larger, as the error component of the relation approaches the signal level. Intuitively one knows that uncertainty would increase if the error's amplitude would become comparable in value with the amplitude of the signal. Therefore using the E/S-ratio makes interpretation of the data easier.

Equations 2.3.5 and 2.3.6 can therefore be rewritten in term of E/S:

$$UpperboundUncertainty|_{dB} = 20log(1 + 10^{\frac{E/S|_{dB}}{20}}) \tag{2.3.7}$$

$$LowerboundUncertainty|_{dB} = 20log(1 - 10^{\frac{E/S|_{dB}}{20}}) \tag{2.3.8}$$

These equations can be rewritten as:

$$E/S|_{dB} = 20log(10^{\frac{UpperboundUncertainty|_{dB}}{20}} - 1) \tag{2.3.9}$$

$$E/S|_{dB} = 20log(1 - 10^{\frac{LowerboundUncertainty|_{dB}}{20}}) \tag{2.3.10}$$

Table 2.1 lists the upper- and lowerbound uncertainties for different E/S-levels assuming a signal level of 0 dB.

2.3.2 Statistical analysis

Newell and Hindman [14] propose in their article about antenna pattern comparison a statistical method to calculate the E/S-level and derive uncertainty from it. The statistical tool that forms the basis of this analytical method is standard deviation. Standard deviation, which is denoted by σ and formulated by equation 2.3.11, quantify how spread-out data values in a dataset are.

$$\sigma = \sqrt{\frac{1}{N}\sum_{i=1}^{N}(x_i - \overline{x})^2} \tag{2.3.11}$$

where N is the number of elements in the sample taken and $\overline{x}$ is the average or the mean of the data set and given by

$$\overline{x} = \frac{1}{N}\sum_{i=1}^{N} x_i \tag{2.3.12}$$

To calculate the E/S-distribution, two far-field antenna patterns, both in dBi can be subtracted from each other. The subsequent result represents the

E/S (S = 0 dB)	Upperbound Uncertainty	Lowerbound Uncertainty
0	6.021	$-\infty$
-5	3.876	-7.177
-10	2.387	-3.302
-15	1.422	-1.701
-20	0.828	-0.915
-25	0.475	-0.503
-30	0.270	-0.279
-35	0.153	-0.156
-40	0.086	-0.087
-45	0.049	-0.049
-50	0.027	-0.028
-55	0.015	-0.015
-60	0.009	-0.009
-65	0.005	-0.005
-70	0.003	-0.003
-75	0.002	-0.002
-80	0.001	-0.001

Table 2.1: E/S with signal level of 0 dB

E/S-distribution over the cut of interest. However, there is typically a large difference in amplitude over the angular range, which makes this result less useful. By calculating the RMS-value of the distribution, an estimate is obtained that represents the E/S-distribution over the full range. The calculated RMS-value is also the standard deviation of the E/S-distribution, because the E/S-distribution is viewed as a probability density function (PDF) or a distribution of uncertainty, and according to Newell and Hindman [14], the PDF's mean ($\overline{x}$) is zero. The formula to calculate the RMS-value can be seen in equation 2.3.13. If equations 2.3.11 and 2.3.13 are compared, keeping in mind that $\overline{x}$ equals zero, it can be seen that this statement holds true.

$$RMS = \sqrt{\frac{1}{N}\sum_{i=1}^{N} x_i^2} \tag{2.3.13}$$

Another way to look at standard deviation is to observe that 68% of the data fall within σ of the mean, as shown in figure 2.14. Therefore σ gives us an associated confidence level of 68% in the calculated E/S-level. To increase the confidence level in the E/S-level and ultimately the uncertainty value, multiples of σ can be used. When the E/S-level is in units of decibels, 6 dB can be added for 2σ, which would render a confidence level of 95.45%. Likewise 9.5 dB can be added to the RMS-level, resulting in a 99.7% confidence level.

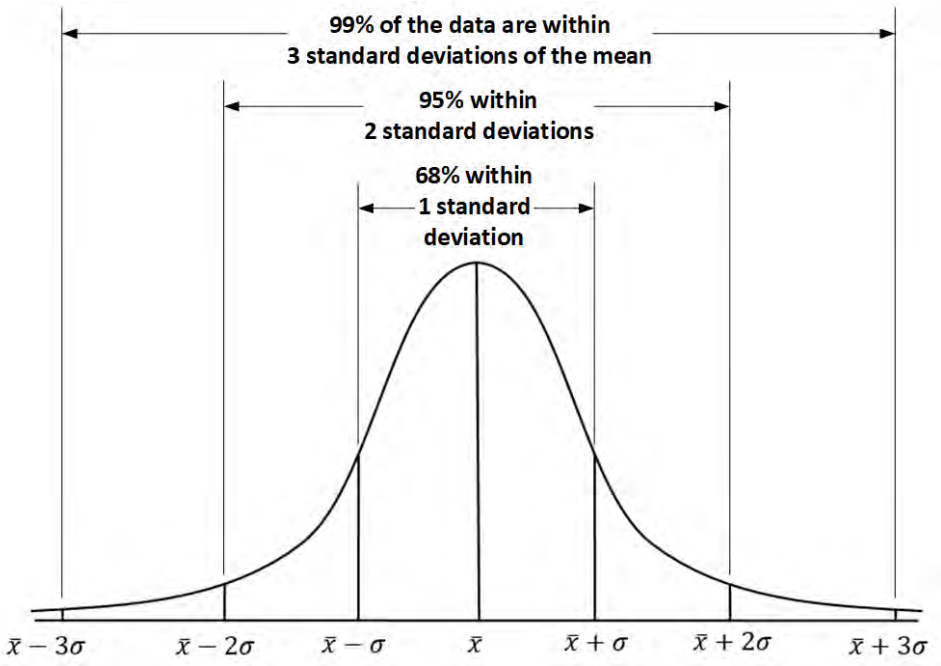

Figure 2.14: Standard deviation, highlighting the confidence level associated with σ, 2σ and 3σ

When comparing antenna patterns to establish the E/S-level, the errors can be divided in three categories: errors that influence only the main beam; errors that influence only the sidelobes; and errors effecting both regions.

Newell and Hindman [14] elaborate on this topic in their article. Firstly, errors that are present in the main beam angular range, influence the following antenna pattern parameters: peak gain, beamwidth, beam pointing, and directivity. The second category deals with errors that occur mainly in the angular range, excluding the main beam angles, these errors influence parameters associated with sidelobes and cross-polarisation. Lastly, when errors occur over the extended angular range, all the parameters mentioned in the first two categories can be affected.

In some instances when radiation patterns are compared by the proposed method, large errors can be induced when main beams are only slightly misaligned, as shown in Figure 2.15a (re-illustrating the sinc example in section 8.4 of Parini [10]). This would raise the E/S-level and incorrect uncertainty levels would result.

It is necessary to normalise the patterns because the difference in amplitude would also elevate the RMS-value. The effect of normalisation can be seen in figures 2.15a and 2.15b whereby normalising the patterns the RMS-value lowered from -32.46 dB to -34.66 dB.

An obvious angular misalignment can be handled in two ways. The first is to use the built-in function of the NSI2000-software and align the angular

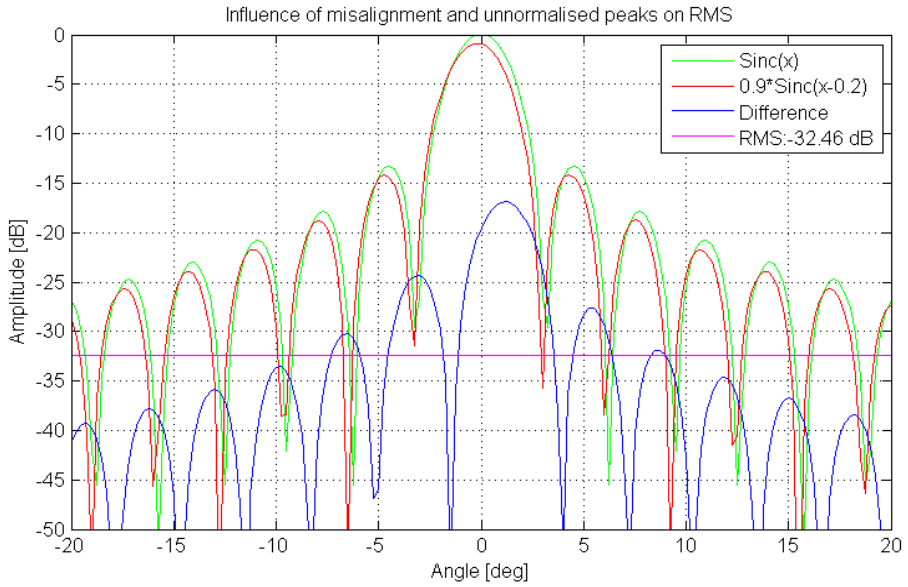

(a) Misaligned, unnormalised patterns cause an elevated RMS-value

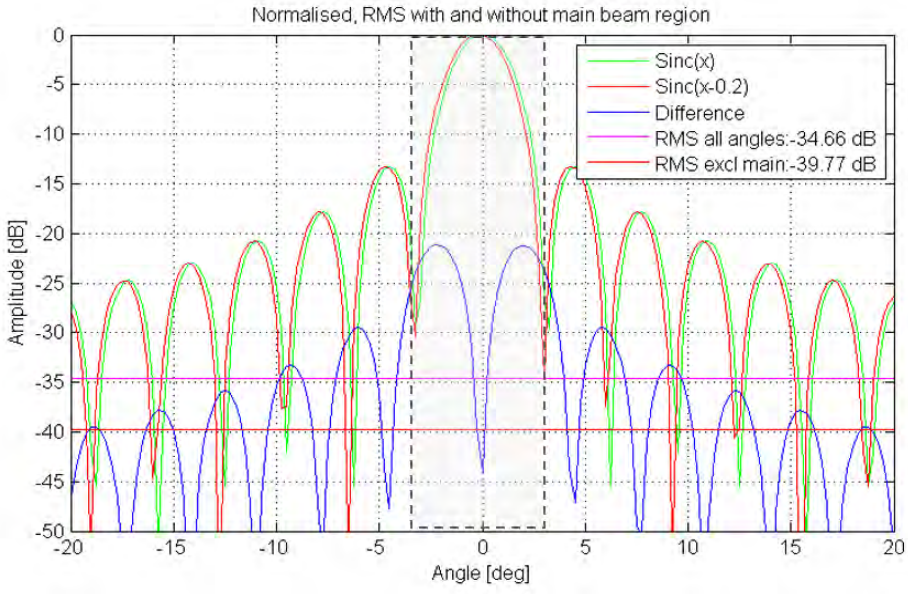

(b) The effect of nomalisation and misalignment compensation on the RMS-value

Figure 2.15: The effect of peak misalignment and normalisation on the calculated RMS-value of the E/S-distribution

peak offset of the main beam by adding an offset to one of the patterns. When the E/S-level is recalculated it will render a much lower, but more accurate RMS-value. The second alternative procedure is to compare the two regions of interest separately [14]. The first step would be to obtain the main beam's parameters (gain, directivity, beamwidth, and far-field peak) for each pattern and compared them individually. The second step would be to calculate

the E/S-level, excluding the E/S-distribution data of the main beam angular range. This would give a more realistic estimate of the uncertainty level. The effect of excluding the E/S-distribution data in the main beam area when an apparent misalignment is present is illustrated in figure 2.15b. By applying this technique an RMS-value of -39.77 dB is obtained.

To summarise, the pattern comparison procedure for errors associated with the sidelobe region includes the following steps:

- Normalise the peaks of the main beam to get relative and not absolute sidelobe levels.
- Exclude the main beam region E/S-distribution from the data used to calculated the E/S-level to remove pattern misalignment.
- To improve the confidence level multiples of the σ can be used.

The following formula is used to calculated uncertainty when a specific sidelobe level is compared to the calculated E/S-level:

$$SidelobeUncertainty|_{dB} = 20log(1 + 10^{\frac{(E/S|_{dB} - SLL|_{dB})}{20}}) \tag{2.3.14}$$

It is important when analysing and comparing measurements, that the data and results be scrutinised and the correct approach be taken to get the most realistic measurement of error and ultimately uncertainty.

2.4 Causes of measurement errors

As discussed, near-field antenna measurements are done in an anechoic chamber and has associated errors that come with measurements. The NIST 18 term error budget of an anechoic chamber is an industry standard to evaluate a chamber's performance. The error budget gives a list of factors that could influence the measurement accuracy. The error terms can be grouped into six categories, namely probe related errors, mechanical/positioner related errors, power level related errors, processing related errors, RF subsystem related errors and environmental related errors. Table 2.2 gives a breakdown of each category.

2.4.1 Probe/illuminator related errors

When performing a scan, the probe's pattern forms part of the measurement and the measured data is not the true reflection of the AUT's actual radiation pattern. This error category can be divided into three groups, each associated with an aspect of the probe that influences the data. These are the probe's pattern, the probe's polarisation purity and mechanical alignment of the probe.

#	**Source of Error**	**Category**
1	Probe relative pattern	Probe/Illuminator related errors
2	Probe polarisation purity	Probe/Illuminator related errors
3	Probe alignment error	Probe/Illuminator related errors
4	Spherical scanner alignment	Mechanical/Positioner related errors
5	Pol-stage alignment	Mechanical/Positioner related errors
6	Inter-stage vector alignment	Mechanical/Positioner related errors
7	Gain standard	Absolute power level related errors
8	Normalisation constant	Absolute power level related errors
9	Impedance mismatch error	Absolute power level related errors
10	Aliasing	Processing related errors
11	Measurement area truncation	Processing related errors
12	Receiver amplitude linearity	RF sub-system related errors
13	System phase error	RF sub-system related errors
14	Leakage and crosstalk	RF sub-system related errors
15	Receiver dynamic range	RF sub-system related errors
16	Multiple reflections	Environmental related errors
17	Chamber Reflection	Environmental related errors
18	Random Amp/Phase Errors	Environmental related errors

Table 2.2: NIST 18 term error

To characterise an antenna fully and in order to perform a near- to far-field transformation, two data sets are necessary. A measurement in which the probe and the AUT's E-fields are aligned and a second measurement where the probe is rotated by 90°, resulting in the E-fields being orthogonal to each other [11][10]. The two expressions that describe the measurements are:

$$I_c = A_c E_c + A_x E_x \tag{2.4.1}$$
$$I_x = A_c E_x + A_x E_c \tag{2.4.2}$$

Where:
I_c: measured co-polarised response (probe orientated horizontally)
I_x: measured cross-polarised response (probe orientated vertically)
A_c: true co-polarised AUT response
A_x: true cross-polarised AUT response
E_c: probe's co-polarised response
E_x: probe's cross-polarised response

Note that at some measuring facilities, two different probes or a dual-port probe is used for the two measurements, but at the US anechoic chamber only

one probe is used for both measurements, and rotated to measure the two polarisations.

To extract the AUT's response the equations can be written in matrix format and the AUT's co- and cross-polarisation can be extracted.

$$\begin{bmatrix} I_c \\ I_x \end{bmatrix} = \begin{bmatrix} E_c & E_x \\ E_x & E_c \end{bmatrix} \begin{bmatrix} A_c \\ A_x \end{bmatrix}$$

$$\begin{bmatrix} A_c \\ A_x \end{bmatrix} = \frac{1}{\Delta} \begin{bmatrix} E_c & -E_x \\ -E_x & E_c \end{bmatrix} \begin{bmatrix} I_c \\ I_x \end{bmatrix}$$

$$\frac{1}{\Delta} = E_c^2 - E_x^2$$

The term, $\frac{E_x}{E_c}$ is referred to as polarisation purity (ρ) and is an indication of how linear the probe polarisation is.

$$\begin{aligned} A_c &= \frac{E_c I_c - E_x I_x}{E_c^2 - E_x^2} \\ &= \frac{\frac{E_c I_c}{E_c^2} - \frac{E_x I_x}{E_c^2}}{1 - \frac{E_x^2}{E_c^2}} \end{aligned}$$

because $E_x^2 \ll E_c^2$, the term $\frac{E_x^2}{E_c^2} \approx 0$. Incorporating this and by adding the polarisation ratio (ρ) of the probe, the above term reduces to:

$$A_c \approx \frac{I_c}{E_c} - \rho \frac{I_x}{E_c} \tag{2.4.3}$$

In the same manner A_x can be derived:

$$\begin{aligned} A_x &= \frac{E_c I_x - E_x I_c}{E_c^2 - E_x^2} \\ &= \frac{\frac{E_c I_x}{E_c^2} - \frac{E_x I_c}{E_c^2}}{1 - \frac{E_x^2}{E_c^2}} \end{aligned}$$

If the assumtion that $\frac{E_x^2}{E_c^2} \approx 0$ is applied and ρ is added, the equation reduces to:

$$A_x \approx \frac{I_x}{E_c} - \rho \frac{I_c}{E_c} \tag{2.4.4}$$

The first term in equations 2.4.3 and 2.4.4 describes the influence of the probe radiation pattern on the measurement. The second term in the above equations give the amount of power leaking through because of the cross-polarised component of the probe. This is best explained by an example. Figure 2.16 shows the results of a planar near-field scan done on an X-band horn antenna. An open-ended-waveguide probe(NSI-RF-WR90) was used for the measurement and the probe's radiation pattern is also displayed on the graphs. Table 2.3 contains data extracted from the graphs in order to highlight certain aspects of the probe correction.

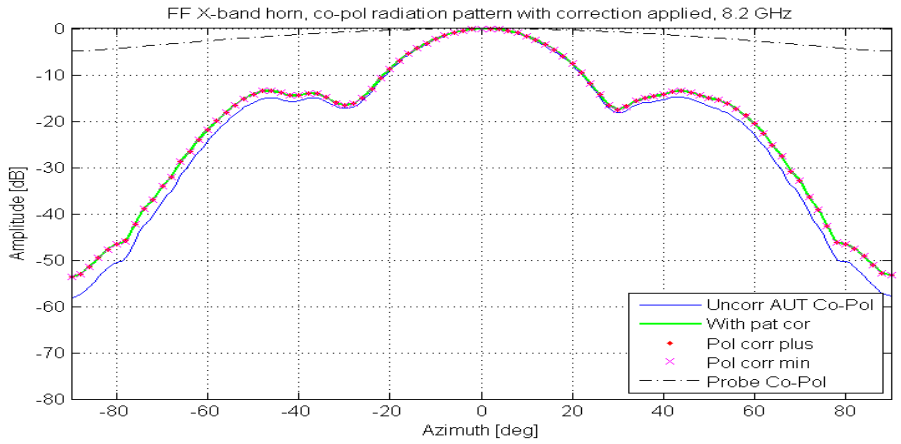

(a) Co-polarised pattern, with firstly pattern correction ($\frac{I_c}{E_c}$) and then polarisation correction ($\rho\frac{I_x}{E_c}$) applied. The probe co-polarisation pattern is also displayed.

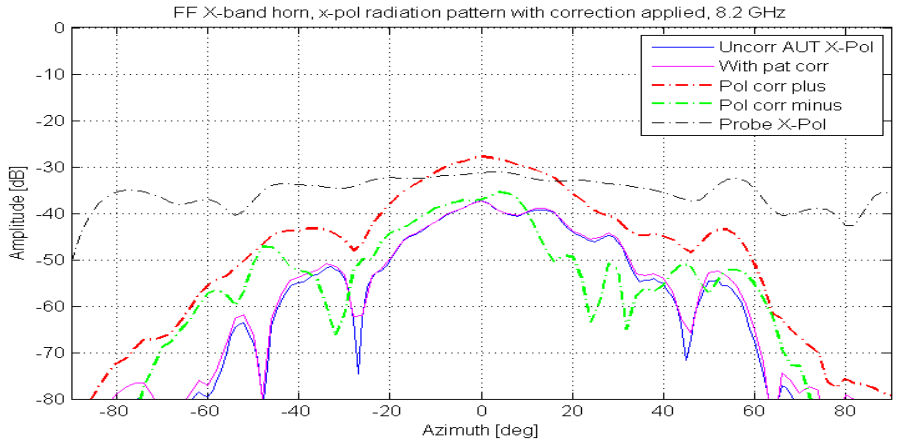

(b) Cross-polarised pattern, with pattern correction ($\frac{I_x}{E_c}$). Polarisation correction ($\rho\frac{I_c}{E_c}$) is added and subtracted to indicate the pattern limits. The probe cross-polarisation pattern is also displayed.

Figure 2.16: Transformed far-field radiation patterns of a PNF-scan (X-band horn) with pattern and probe polarisation correction applied

Co-Polarisation measurement results								
θ	I_c [dB]	I_x [dB]	E_c [dB]	E_x[dB]	$\frac{I_c}{E_c}$ [dB]	$\rho\frac{I_x}{E_c}$ [dB]	$\frac{I_c}{E_c}+\rho\frac{I_x}{E_c}$	$\frac{I_c}{E_c}-\rho\frac{I_x}{E_c}$
-60°	-24.15	-79.48	-2.35	-36.92	-21.80	-111.69	-21.79	-21.80
-30°	-17.24	-53.93	-0.69	-34.69	-16.54	-87.24	-16.54	-16.55
0°	0.00	-37.44	0.00	-31.28	0.00	-68.71	0.01	0.00
30°	-18.18	-46.09	-0.69	-33.89	-17.50	-78.60	-17.49	-17.50
60°	-22.87	-67.50	-2.36	-34.58	-20.51	-97.36	-20.51	-20.51
X-Polarisation measurement results								
θ	I_c [dB]	I_x [dB]	E_c [dB]	E_x[dB]	$\frac{I_x}{E_c}$ [dB]	$\rho\frac{I_c}{E_c}$ [dB]	$\frac{I_x}{E_c}+\rho\frac{I_c}{E_c}$	$\frac{I_x}{E_c}-\rho\frac{I_c}{E_c}$
-60°	-24.15	-79.48	-2.35	-36.92	-77.12	-56.36	-55.60	-57.19
-30°	-17.24	-53.93	-0.69	-34.69	-53.24	-50.54	-45.77	-62.01
0°	0.00	-37.44	0.00	-31.28	-37.44	-31.27	-27.80	-37.14
30°	-18.18	-46.09	-0.69	-33.89	-45.40	-50.70	-41.63	-52.21
60°	-22.87	-67.50	-2.36	-34.58	-65.14	-52.73	-50.86	-55.11

Table 2.3: AUT probe pattern correction

As can be seen in figure 2.16a, the AUT co-polarisation pattern is dominated by the first term in equation 2.4.3 ($\frac{I_c}{E_c}$) and the second term ($\rho\frac{I_x}{E_c}$) has little or no influence in the corrected pattern.

On the other hand the cross-polarisation pattern (figure 2.16b is mainly influenced by the second term of equation 2.4.4. The polarisation correction term is added, but can also be subtracted to apply the correction because the phase is unknown. This results in an upper and lower limit of the cross-polarisation pattern and the actual pattern would be somewhere in between.

The influence of the probe's radiation pattern on the co-polarisation and cross-polarisation pattern of the AUT is even better presented in Table 2.3 than in figure 2.16.

Probe relative pattern

In the process of a near-field scan, the probe can either move across the aperture of the AUT (planar near-field-scan (PNF-scan)) or the AUT can rotate in a sphere (spherical near-field-scan (SNF-scan)) in front of the probe. At the data acquisition points where the two antenna main beams are not exactly aligned, the probe's radiation pattern start "corrupting" the data measured. This is illustrated in figure 2.17. The probe and the AUT radiation patterns both contribute to the measurement, and pattern correction needs to be applied to the probe's influence and extract only the data that is relevant to the the AUT. This is explained in the previous section and is done by applying the first term of equations 2.4.3 and 2.4.4 to the measured data.

As can be seen in figure 2.17, larger errors will occur during PNF-scans than during SNF-scans, because when boresight (front on) measurements are done, no pattern correction is necessary, as is the case for SNF-scans with

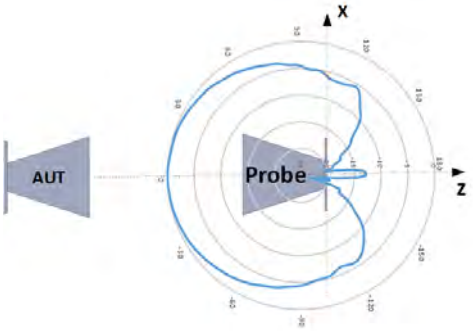

(a) PNF-scan: AUT and probe aligned

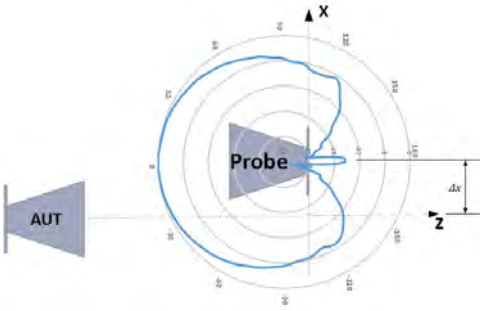

(b) PNF-scan: Probe moved by Δx

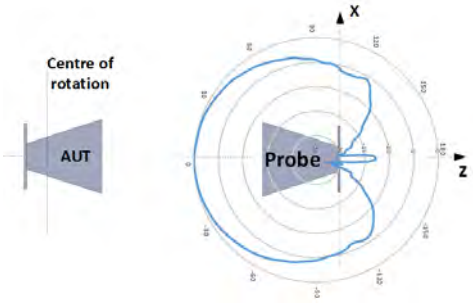

(c) SNF-scan: AUT and probe aligned

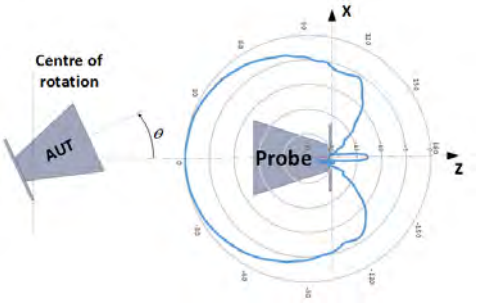

(d) SNF-scan: AUT rotated through θ

Figure 2.17: Probe pattern influence on AUT's pattern

the AUT mounted on the centre of rotation. For the PNF-scan, however, the probe moves in a plane in front of the AUT. The result is that most acquisition points are at a delta distance from the (0,0) position and an error in amplitude measurement is created.

This is illustrated in figure 2.18 where a X-band horn is measured with a PNF-scan and the measurement repeated with a SNF-scan. The transformation for both measurements are done with and without probe correction and the RMS-value is taken of the difference. It can be seen that the error is extremely small for the SNF-scan and much larger for the PNF-scan. According to Parini et al. [10] probe correction is in some instances not done for SNF-scans and from the above example it can be seen why it may be omitted.

Probe polarisation purity

The second aspect to consider is the fact that the probe's cross-polarisation component is not infinitely small. Therefore, some power is leaking through as a result of the cross-polarisation component of the probe. As mentioned in the introduction of this section, the term describing the probe co-cross polarisation relationship is called polarisation purity and represented by the symbol, ρ. It forms part of equations 2.4.3 and 2.4.4 and has a particularly large influence in the cross-polarisation pattern.

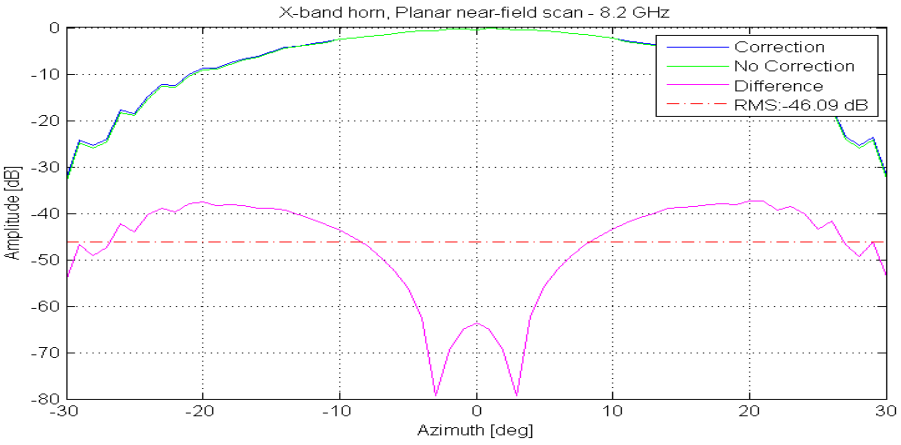

(a) X-band horn measured with a PNF-scan

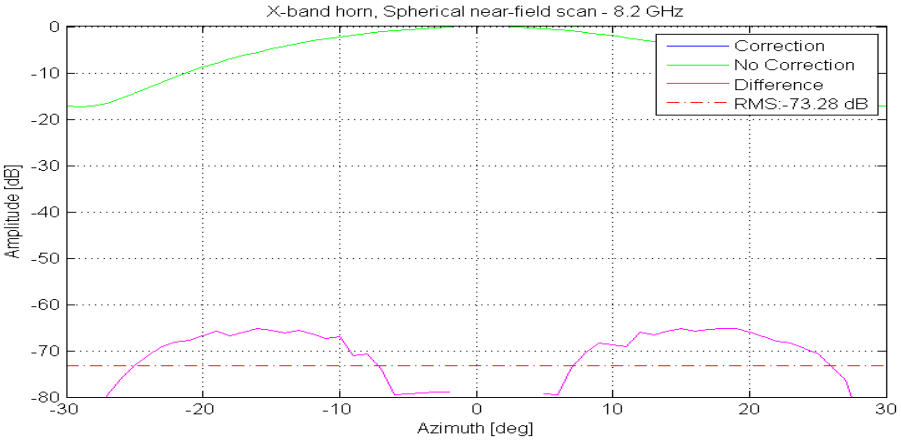

(b) X-band horn measured with a SNF-scan

Figure 2.18: Illustration of the importance of probe correction on PNF-scans vs. SNF-scans

Probe alignment

Another contributor to probe or illuminator errors is probe misalignment. There are two possibilities to consider - firstly if the probe's aperture is not orthogonal to the axis on which the antenna and the probe is aligned, an axial pointing misalignment results (figure 2.19a); secondly a rotation in the probe's aperture will have the effect that the probe polarisation vector is misaligned with respect to the defined axis (figure 2.19b).

The result of these types of misalignments is that the radiation pattern data used for the pattern correction does not correlate with the probe's radiation pattern used for the measurement. Another aspect is that the rotation of the probe around the polarisation-axis will cause sampling of unwanted field components. (*Note*: The probe is mounted on a rotatable stage to be able to measure co- and cross-polarisation components. This stage is commonly

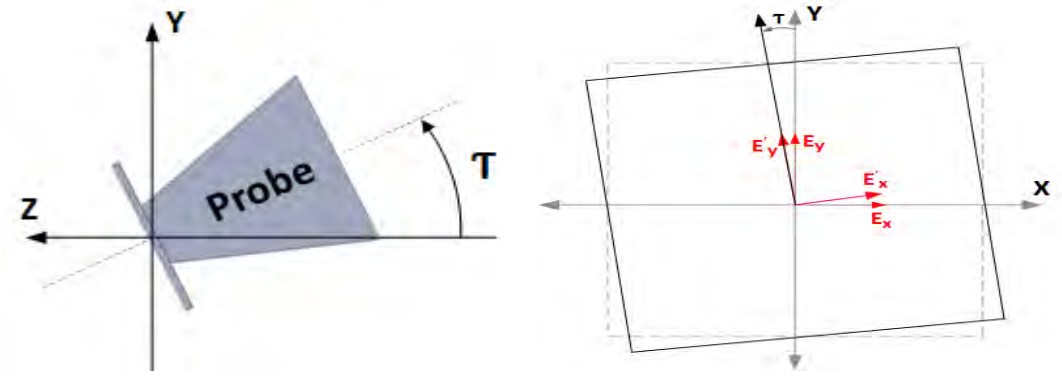

(a) Probe axial pointing misalignment (b) Probe polarisation tilt misalignment

Figure 2.19: Probe alignment errors

known as the pol-stage and the axis of rotation associated with it, the pol-axis.

As was the case in the previous sections, the error due to probe misalignment is more acute for PNF-scans than for SNF-scans. This is true because the broad beamwidths of probes makes the SNF-scanners more immune to small misalignments.

2.4.2 Mechanical related errors

When spherical near-field to far-field transformations are done, the assumption is made that the data was captured over a perfect spherical surface. Mechanical misalignment will result in a less than perfect sphere. It is therefore critical that the alignment of the spherical near-field scanner is within specification and with minimum deviations from the ideal positions.

The spherical near-field scanner at US has three rotational stages. Each of these stages should be aligned vertically and horisontally and also aligned to each other.

Spherical scanner alignment

The sphere on which the data of the AUT is captured, is formed by two rotational axes, the θ-axis and the ϕ-axis, as seen in figure 2.20. The θ-axis is vertical and should be in line with gravitational vector. The ϕ-axis on the other hand is horizontal and normal to the gravitational vector. These two vectors should be intersecting and orthogonal to each other. If these criteria is met, a perfect sphere will form when the AUT are rotated.

Polarisation-stage alignment

A complete data set required for the near- to far-field transformation is composed of two measurements. In the case of linearly polarised antennas a

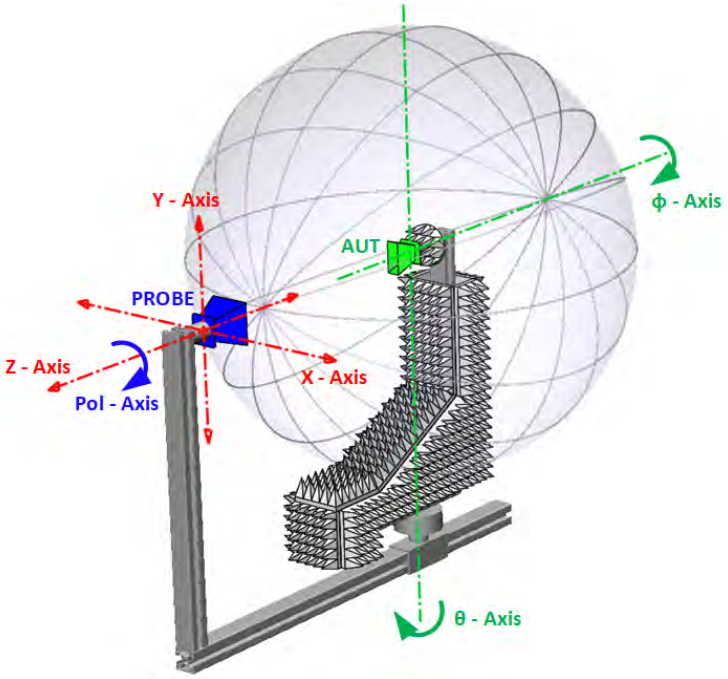

Figure 2.20: SNF-scanner axis configuration

co-polarisation measurement as well as a cross-polarisation measurement are taken. When doing an SNF-scan of a circular polarised antenna, two data sets are also recorded, one with the linearly polarised probe's E-field horizontal and another with the same probe's E-field in a vertical position. The probe must therefore be able to rotate through at least 90°. The pol-axis should be horizontal and normal to the gravitational axis.

Inter-stage pointing vector alignment

It is important that the ϕ-axis of the AUT and the pol-axis of the probe are aligned. If the ϕ-stage and the pol-stage are vertically and horizontally aligned, but the pol-axis does not originate on (x,y)=(0,0), the pol-axis would be parallel to the ϕ-axis. Hansen [4] discuss the influence of mechanical errors in chapter 6 of his book and according to the author a misalignment of the inter-stage pointing vector will cause a smaller aperture over which the samples are taken. This will result in a small error in directivity, but it can also have an influence on the sidelobe level.

2.4.3 Absolute power level related errors

The errors associated with the absolute power level influence only the absolute peak gain of the antenna under test and not any relative measurements such as sidelobe level or cross-polarisation. It can therefore be omitted if gain uncertainty is not done [10].

Gain standard

This term only applies to gain measurements methods where the probe is the gain standard or the antenna under test gain is calculated by comparing it to a standard gain horn. These type of techniques are referred to as gain replacement methods (discussed in section 2.2.2). As mentioned in the indicated section, the University of Stellenbosch's measuring facility does not own standard gain horns or calibrated probes. The gain is measured by direct measuring techniques, such as the two and three antenna methods. This uncertainty is therefore not applicable to the facility under evaluation.

Normalisation constant

The normalisation constant combine all the possible amplitude errors. This error results from, amongst other things, connector repeatability, receiver linearity and amplitude drift. It can be measured by performing repeated measurements. The differences between the measurements can be used to calculated the uncertainty.

Impedance mismatch error

The input impedances of the AUT, the probe and the network cables differ. When the gain replacement method is used to measure the gain of the AUT there is a difference in the combination of each connection's reflection coefficient. This leads to a difference in the amount of power that gets transferred for each connection. This should be taken into account if this specific gain method is used for gain measurements.

On the other hand, when the absolute gain method is used, the loss, as a result of the impedance mismatch, forms part of the measurement, the reason being that a response calibration is done at the antenna ports, which then becomes the calibrated interface. When a particular antenna is connected to these interfaces, the same mismatch is seen every time and this forms part of the particular antenna's measurement as illustrated in figure 2.1. Thus, using the absolute gain method, realised gain and not absolute gain is the result.

As mentioned before, at the US measuring facility, gain is only measured with the absolute gain method (two or three antenna method). Consequently, the impedance mismatch error become irrelevant for the chosen measurement method.

2.4.4 Processing related errors

Aliasing

Aliasing errors occur when the spatial sampling density of a signal is too low and not enough information about the signal is gathered to reconstruct it.

There are two different sampling options to take into account when aliasing errors in a near-field measuring system is considered. Firstly, when dealing with linear sampling, as in the case of planar near-field scanning or the elevation axis of a cylindrical near-field scanner, the Nyquist theorem must be adhered to.

The Nyquist theorem stipulates that to prevent aliasing, a signal must be sampled at a minimum of $\frac{\lambda}{2}$ intervals, where λ is the wavelength of the highest frequency. For linear scans, this would be the minimum distance between sampling points.

However, in the case of angular sampling, the angular sampling density is specified as [3][20]:

$$\Delta\theta = \Delta\phi = \frac{360^\circ}{2N+1} \tag{2.4.5}$$

where N is the minimum number of spherical modes and defined by,

$$N = \left(\frac{2\pi MRE}{\lambda}\right) + 10 \tag{2.4.6}$$

with 10 a safety factor to ensure that all modes are captured.

The MRE is defined as the minimum radius of a sphere, with its center at the origin of the θ/ϕ-coordinate system, that completely encapsulates the AUT. When the number of samples as specified in equation 2.4.6 is taken, the sample density is large enough to capture all the spherical wave modes that contribute to the spherical wave expansion beyond the reactive region [10][3]. By obtaining a sufficient number of modal coefficients, spherical wave expansion can be applied and the AUT's far-field can be determined [21].

Measurement area truncation

Far-field transformation can only be done if all the energy of the AUT is captured when a near-field scan is done [15]. This, however, is not possible. For example, when a PNF-scan is done, the scan-area would have to stretch to infinity to capture all the energy. The question is therefore not whether there is measurement area truncation, it is, how much truncation is allowed before it influences the near- to far-field transformation? The recommendation is that the scan area should at least be large enough to capture the energy to at least -30 dB, preferably -40 dB below the peak value [3]. This holds true for PNF- as well as SNF-scans. This limits the antennas that can be measured with PNF-scans to directive antennas. Although it is easier to achieve this recommendation with a SNF-scan, the operator should keep in mind that a portion of the AUT is concealed from the probe by the mounting structure during the full sphere scan.

2.4.5 RF sub-system

Receiver amplitude linearity

An important specification of the receiver is the ability to measure accurately and linearly over a large range of amplitude values. This is referred to as receiver amplitude linearity [10]. The receiver amplitude linearity is determined by the linearity of the network analyser.

System phase error

Near- to far-field transformations require both amplitude and phase information. The phase stability of the system is influenced by the movement of the cables, the rotary joints and the phase stability of the receiver itself [10][3].

Leakage and crosstalk

Leakage and crosstalk refer to a scenario where some of the received signal is from a source other than the AUT's transmitted signal [3][10]. The unwanted signal has three main sources - the first originates from crosstalk between the measurement and reference channels; the second from the system such as badly shielded cables, connections and malfunctioning joints; the third from biasing errors in the receiver's detector [22].

Receiver dynamic range

The Agilent PNA-X network analyser datasheet defines the system dynamic range as "the maximum leveled output power minus the noise floor" [23]. However, all the components of the measuring facility need to be taken into account when the dynamic range of the system is determined because the losses in the rest of the system lessen the maximum received power. Therefore the specification of the network analyser is an inadequate definition to determine the dynamic range of a measuring facility. Consequently, the dynamic range of the measuring facility can be re-defined as the difference between the maximum possible input the receiver can obtain, after the losses of the system are taken into account, and the minimum receiver input signal that the receiver is able to distinguish from the noise floor [10].

2.4.6 Environmental related errors

By using an anechoic chamber as an environment for the spherical near-field scanner, an ideal free-space environment is aimed for. This is unfortunately only achievable in theory because the AUT and probe need to be mounted onto something, and although the walls and floors are covered with absorbing material, there are limits to its absorbing performance, especially with regards to low frequencies. The absorbing material's specification is also made on the

assumption the incident wave is perpendicular to the absorbing material and the performance changes when the angle is anything other than 90°.

Multiple reflections

Probe structure reflections are the result of multiple reflections between the structures that hold the AUT and the probe in position as well as the AUT and the probe themselves [10][24]. For near-field measurements, the separation distance between AUT and the probe is small. The possibility exists that some of the transmitted signal will be reflected back from the receive antenna's structure and then again to the transmit antenna's structure. This reflected signal could bounce back and forth between the antennas. The antenna will receive these reflected signals and depending on the distance and the wavelength, the signals will either add or subtract to the primary transmitted signal and change the net result.

Chamber reflection

Chamber reflection is also known as room scattering. These reflections occur not between the probe and the AUT, but between the AUT and the environment such as the walls and floor. It is the added signal, which originate from multipath, to the direct signal. Where multipath is defined by Slater [11], as "multiple propagation paths between stationary objects".

Random amplitude/phase errors

This random error is a combination of all variations in amplitude and phase that might occur when there are no changes made to the system [10][3]. This error and the uncertainty associated with it can, therefore, be viewed as the absolute minimum error that is measurable, and can be considered the error floor of the system.

Chapter 3

Error Analysis of US anechoic chamber

In chapter 2 possible errors that can occur in antenna measurements are discussed. This chapter will systematically evaluate these errors. Newell [25] and Yaghjian [24] state that the evaluation can not simply be done by measuring near-field patterns and comparing them with a set of measured far-field patterns because both measured patterns contain uncertainties. Evaluation measurements, therefore, have to be done in such a way that a given change between two measurements, would enable the extraction of the error under investigation. The NIST 18 term error analysis is a method widely used to evaluate measurement errors and consequently determine the associated measurement uncertainty. This method not only uses measurements as a tool for evaluation, but error equations and computer simulations also form part of the assessment. The evaluation method for the different error terms is indicated in Tabel 3 [3][10][25].

The analysis can also be grouped into errors that can be associated with the main beam area and errors that have a bigger influence on the sidelobes. This distinction is also highlighted in Table 3.

#	**Source of Error**	**Evaluate with**	**Impact**
Probe/Illuminator related errors			
1	Probe relative pattern	Measurement	Sidelobe
2	Probe polarisation purity	Measurement	Cross-pol
3	Probe alignment error	Simulation	Sidelobe, Cross-pol
Mechanical/Positioner related errors			
4	Spherical scanner alignment	Simulation	Sidelobe, Cross-pol
5	Pol-stage alignment	Simulation	Sidelobe

#	**Source of Error**	**Evaluate with**	**Impact**
6	Inter-stage pointing vector alignment	Simulation	Sidelobe
Absolute power level related errors			
7	Gain standard	N/A	N/A
8	Normalisation constant	Measurement	Gain
9	Impedance mismatch error	N/A	N/A
Processing related errors			
10	Aliasing	Measurement Error Equation	Gain, Sidelobe
11	Measurement area truncation	Measurement	Sidelobe
RF sub-system related errors			
12	Receiver amplitude linearity	Measurement	Sidelobe
13	System phase error	Measurement	Sidelobe
14	Leakage and crosstalk	Measurement	Low impact
15	Receiver dynamic range	Measurement	Gain, Sidelobe
Environmental related errors			
16	Multiple reflections	Measurement	Gain, Sidelobe
17	Chamber Reflection	Measurement	Gain, Sidelobe
18	Random Amp/Phase Errors	Measurement	Low impact

Table 3.1: NIST 18 term error.

3.1 Probe/illuminator related errors

3.1.1 Probe pattern correction for the SNF-scanner

As described in section 2.4.1, and shown in figure 2.17, pattern correction is more of an issue when a planar near-field scan is done, compared with when a spherical near-field scan is performed. However, for a full evaluation, pattern correction for SNF-scans must be evaluated, specifically on how much the probe's radiation pattern influences the far-field result of an SNF-scan.

The co- and cross-polarisation patterns of two probes (overlapping in frequency from 4 to 6 GHz) were measured and are displayed in figure 3.1. The NSI-RF-WR187 is an open-ended-waveguide probe and the NSI-RF-RGP10

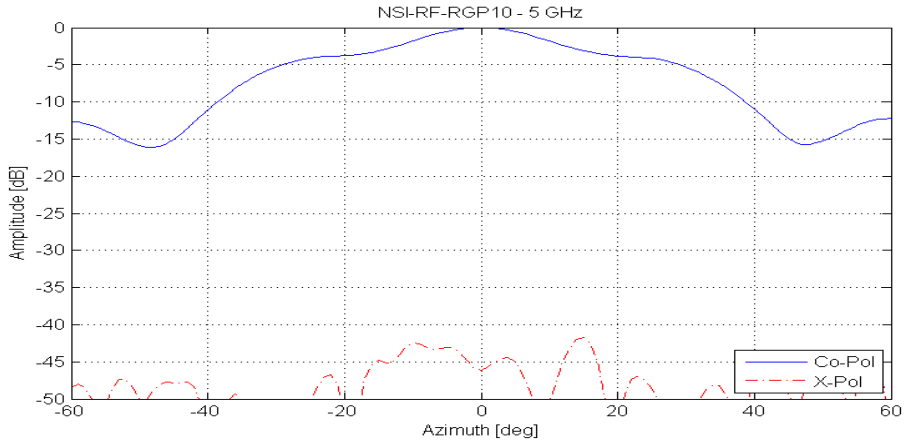

(a) NSI-RF-RGP10 Azimuth co- and cross-polarisation patterns

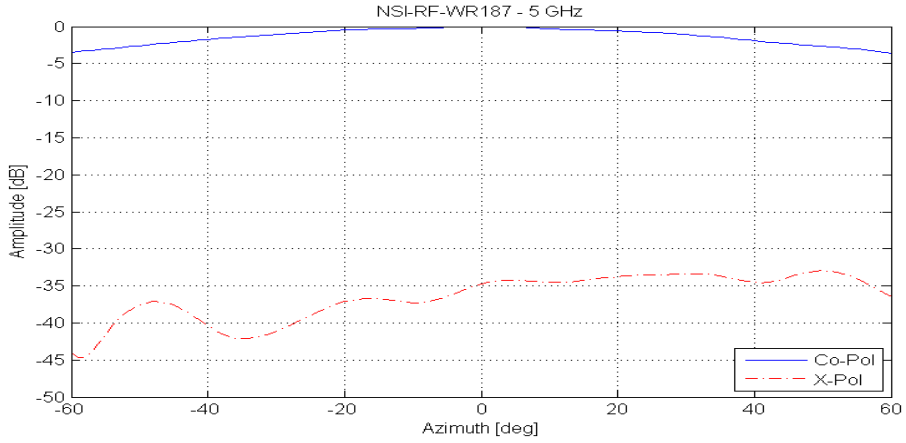

(b) NSI-RF-WR187 Azimuth co- and cross-polarisation patterns

Figure 3.1: Probe radiation patterns of different types of probes

is a wide frequency-band ridge-guide horn probe. As seen in figure 3.1, the beamwidths of these two antennas differ significantly.

The NSI2000-software has an option to do a transformation with or without probe correction. The AUT was measured with both probes and the transformations done with the pattern correction option turned on and off for both. The results are displayed in figure 3.2. Small differences in the transformed patterns with and without correction are observed. When the patterns are subtracted from each other and an RMS-value is calculated, the RMS-value of the NSI-RF-RGP10 (horn probe) measurement is larger than that of the open-ended-waveguide measurement. This implies that correction done for the NSI-RF-RGP10 (horn) is more critical than for the NSI-RF-WR187 (open-ended-waveguide). This is exactly the reason why the horn probe is unsuitable for PNF-scans because of it's narrow beamwidth.

To conclude the investigation of the effect of the probe radiation pattern

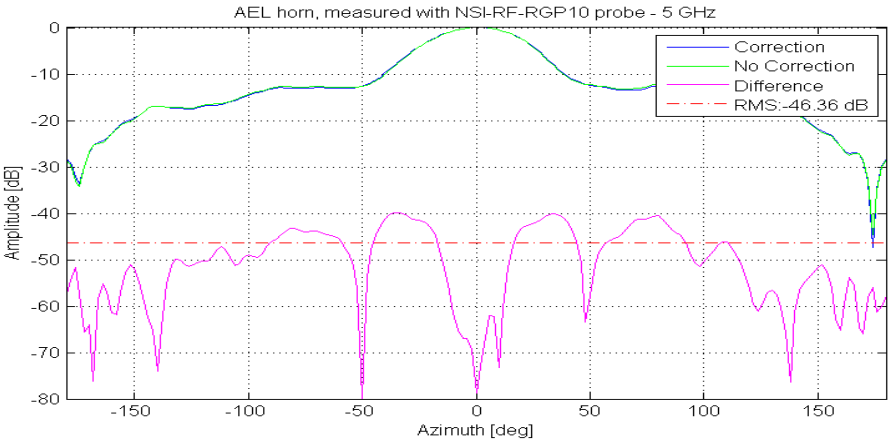

(a) AUT measured with NSI-RF-RGP10

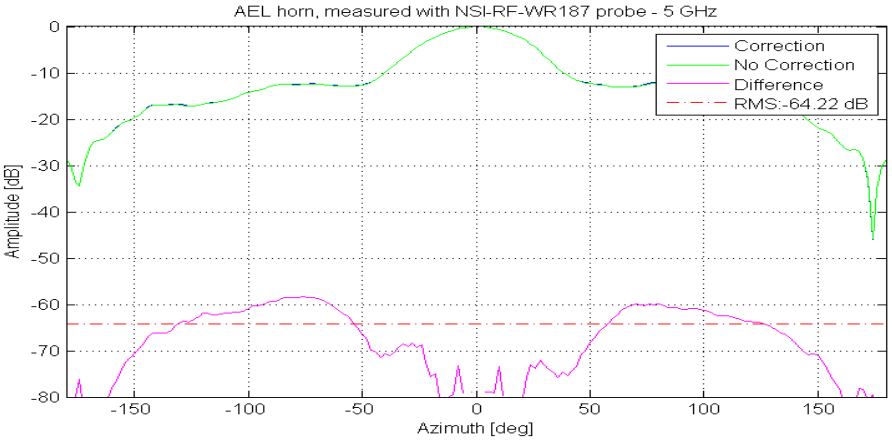

(b) AUT measured with NSI-RF-WR187

Figure 3.2: AEL 2-18 GHz horn measured with two different probes, with and without probe correction turned on

on SNF-scans, consider the probe corrected radiation patterns of an AEL 2-18 GHz horn displayed in figure 3.3. This result gives an indication of how little difference the type of probe makes in a spherical near-field scan. The RMS-value of the difference between the two measurements was calculated as -47.32 dB. This indicates an uncertainty of 0.037 dB for the main beam and 1.109 dB for a -30 dB sidelobe. This difference in pattern measurement can probably be more attributed to the repeatability of a measurement set-up rather than errors due to probe correction. A more in-depth investigation into AUT alignment will be done in the section dealing with mechanical alignment errors.

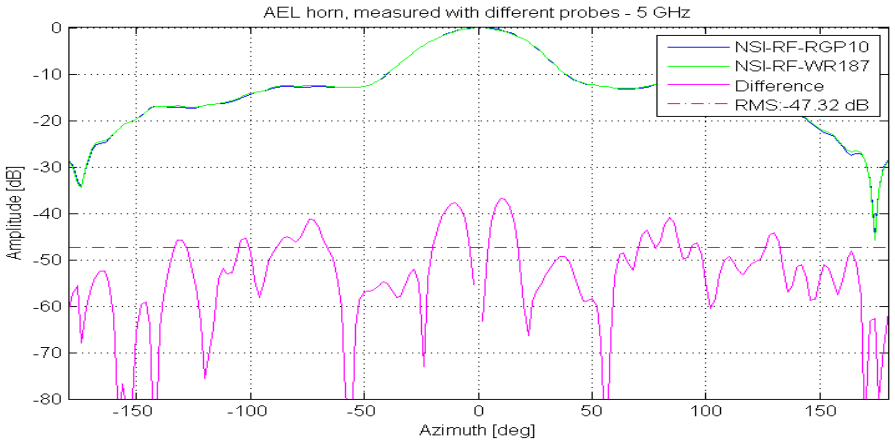

Figure 3.3: AEL 2-18 GHz, measured with different types of probes

3.1.2 Probe polarisation purity

As discussed in section 2.4.1, polarisation purity typically only has an influence on the cross polarisation patterns. The effect of the polarisation is also more acute at lower levels of sidelobes, and unlike pattern correction, which mainly influences only PNF-scans, polarisation correction is applicable to SNF-scans as well.

At the measuring facility of Stellenbosch University a whole range of probes is available for measurements. For the frequency band of 0.75 - 3.85 GHz, only SNF-scans are done, since the available probe is the NSI-RF-RGP10 horn. From 3.85 GHz upwards, OEWG-probes are used and both SNF- and PNF-scans can be done.

The cross-polarised level of the NSI-RF-RGP10 is specified at $<$ -25 dB, but measured much lower as seen in figure 3.1. The OEWG-probes were measured at $<$-30 dB. No probe cross-polarisation correction is done by the NSI2000-software for OEWG-probes. The cross-polarisation is assumed to be infinitesimally small and a theoretical value of -300 dB is used.

The cross-polarised patterns that the NSI2000 software produces when OEWG-probes are used, must be viewed as uncorrected cross-polarised radiation patterns. It is clearly illustrated in figure 2.16b that the cross-polarised pattern changes significantly when polarisation correction is applied.

3.1.3 Probe alignment

Probe axial misalignment

Probe axial misalignment produces a shift in the angular pattern of the probe. According to Parini et al. [10] only a small portion of the probe pattern illuminates the AUT when a SNF-scan is done. This is illustrated in figure 2.17c and 2.17d, and since the probe's beamwidth is wide, especially when a co-

polarisation measurement is done, it seldom has an influence on the accuracy of the results.

To calculate how large the effect of the probe misalignment is, the slope of the probe pattern can be multiplied by the angular uncertainty [10]. The slope of the co-polarisation pattern of the open-ended-waveguide probe can be seen in figure 3.1b and it is estimated at 0.06 dB/° and if an axial misalignment of ±0.5° is assumed, the uncertainty is calculated at ±0.03 dB.

To confirm that the influence of the probe axial misalignment is extremely small, reference is made to the Hansen study 3.2.1 in section 3.2.1. This is reference in the next section that deals with mechanical errors, but it is also applicable to probe alignment. Hansen induced a 0.1λ error in a simulation and calculated what the effect this would have on the far-field radiation patterns. His results are reproduced in figure 3.4. Item (5): Pol-axis horizontal misalignment and (6): Pol-axis vertical misalignment deal with probe axial misalignment. As can be seen, the effect of a probe axial misalignment on the radiation pattern is very small.

Probe tilt misalignment

To align probes and antennas at the measuring facility at the University of Stellenbosch, a Starrett 98-6 6-inch precision level is used. The accuracy of the level is specified as 0.42 mm/m or 0.024°. Once again reference is made to the Hansen study (figure 3.4, (7) Probe axial rotation) and again an error larger than what we can achieve in alignment accuracy, is introduced.

The effect is only visible in the cross-polarisation pattern and negligible in the co-polarisation patterns. If the set-up is done with precision, the probe alignment should be of very little concern, especially in co-polarisation patterns.

3.2 Mechanical related errors

The success of near-field measurements is based on the accurate sampling of data at specific positions. Therefore, the basis on which transformations are done, rests on the assumption that data is sampled on a perfect sphere containing the antenna. The sphere's radius and distance of the centre to the probe, are known [26].

An in-depth study of the effects of mechanical errors on the transformed patterns and gain was done by Hansen and will be discussed here. Furthermore, the SNF-scanner was evaluated to determine whether it is within the manufacturer's specifications and allowed tolerances. If this is the case, we can conclude that the SNF-scanner should render reliable results.

3.2.1 The Hansen study

It is difficult to assess the errors due to mechanical misalignment. Parini et al. [10] used finite element analysis to predict the deformation in the mechanical structures onto which the antenna and probe are mounted. The deformations were introduced in simulations to see what the effect on the radiation patterns was. However, the SNF-scanner configuration in Parini's investigation is different from the scanner at the University of Stellenbosch and therefore results are not directly applicable.

Hansen [4], in his book on spherical near-field antenna measurements, followed a similar route, but did not analyse the mechanical structure separately. He inserted one misalignment error at a time into a simulation to examine what effect that particular inaccuracy has on the transformed patterns. He did his evaluation on the same type of spherical near-field scanner that is used at the University of Stellenbosch. The results would therefore be a good indication of what can be expected under similar circumstances.

The potential errors are listed by Hansen [4] as:

1. Non-intersection of the ϕ- and the θ-axis. A lateral displacement of the ϕ-axis.

2. Horizontal misalignment of the ϕ-axis when $\theta = 0°$. There is a offset angle between the z-axis and the ϕ-axis vector. In other words the ϕ-stage interface is not parallel to the x-y plane on which the probe is mounted.

3. Vertical misalignment of the ϕ-axis when $\theta = 0°$. The ϕ-axis vector is not perpendicular to the gravitational vector.

4. Incorrect maximum radial extent (MRE). The MRE is the radius of the sphere that encapsulate the antenna. The origin of the sphere is the intersection of the ϕ- and the θ-axis.

5. Horizontal displacement of the probe. The pol- and ϕ-axis are parallel to each other on the horizontal plane.

6. Vertical displacement of the probe. The probe has a vertical offset on the vertical plane.

7. The probe has an axial rotation.

8. Inaccuracies in the positions of the sampling points.

A D = 30λ reflector antenna is used for the simulations and small errors of 0.1λ or $0.1°$ were introduced into the model. The results of Hansen's study are shown in figure 3.4.

Hansen's mechanical misalignment study		Main Beam			First null	First side lobe	Cross-polar lobe
		Directivity	Cross-polar level	Beam width	Position	Level	Level
Reference far-field values		38.4 dBi	-∞ dB	2.25°	2.95°	-26.8 dB	-48.2 dB
Mechanical inaccuracies	Offset	Change in dB	Increased to (dB)	Change in degrees	Change in degrees	Change in dB	Change in dB
1. Non-intersecting axes (ϕ- & θ-axis)	0.1λ	0.07	—	0.02	0.02	0.07	0.05
2. ϕ-axis horizontal depointing	0.1°	0.03	—	—	—	1.2	0.03
3. ϕ-axis vertical depointing	0.1°	—	-75	—	—	—	—
4. MRE incorrect	0.1λ	—	—	—	—	0.14	—
5. Pol-axis horizontal misalignment	0.1λ	0.04	—	—	0.01	1.6	0.03
6. Pol-axis vertical misalignment	0.1λ	—	—	—	—	—	—
7. Probe axial rotation	0.1°	—	-55	—	—	—	0.15
8. Angular resolution	±0.03°	—	—	—	—	0.11	0.09

Figure 3.4: The potential errors listed by Hansen [4]

3.2.2 Implication of the Hansen study on the mechanical related errors

The mechanical errors of NIST18-term analysis can be correlated with the Hansen study that was discussed in the previous section. The aim of this section is to highlight which errors do apply and conclude how they influence uncertainty.

Spherical Scanner alignment: There are three components to consider when one looks at spherical misalignment: Firstly the non-intersection of the θ- and ϕ-axis, secondly the horizontal alignment of the ϕ-axis which should be orthogonal to the gravitational vector, and thirdly the θ-axis alignment to the gravitational vector.

These aspects relate to (1) non-intersection of the θ- and ϕ-axis, (2) horizontal misalignment of the ϕ-axis and (3) vertical misalignment of the ϕ-axis. The vertical misalignment of the ϕ-axis produces the same error as when the θ-axis is not parallel to the gravitational vector.

When considering the errors induced in the Hansen study, it is clear that all three factors have almost no influence on the main beam. When the θ-axis is not vertical it increases the cross polarisation level to a measurable value of -55 dB for an added error of 0.1°. If the ϕ-axis is not horizontal it has the largest effect and in particular on the first sidelobe level which is changed by 1.2 dB. For this reason, because the alignment error causing this change, are small, care should be taken with the alignment of the spherical scanner.

Polarisation-stage alignment: The polarisation-stage misalignment refers to the probe alignment, items (5) and (6) in the Hansen study. Small errors can be expected in the main beam, but the horizontal pol-axis misalignment can introduce a significant error in the sidelobe level.

Inter-stage pointing vector alignment: Item (5) refers to the horizontal displacement of the probe. The result is that the pol-axis and the ϕ-axis are parallel, but not on top of each other. In other words, the inter-stage vectors are not aligned. Hansen mentions in his discussion of the results that it not only affects the sidelobe level, but the beamwidth becomes narrower as seen from the table in the first null position that changes. This is small, however in relation to the sidelobe level that changes by 1.6 dB, which is a rather significant change.

3.2.3 Calibration and evaluation of the US SNF-scanner

The approach taken in this assessment of the mechanical related errors was to evaluate the hardware set-up and check whether it is within the allowed tolerances. This was done by using calibration and measuring techniques proposed by NSI-MI Technologies. An electrical alignment script is available with the NSI-software and this tool was used to fine tune the alignment.

The following steps were taken to calibrate and align the spherical nearfield scanner:

1. Prepare the facility for calibration by indexing the linear- and rotation-axis.
2. Calibrate the laser with the manufacturer's procedure.
3. Determine the centre of rotation of the SNF-scanner.
4. Establish the height of the ϕ-stage. The height of the ϕ-stage is at a fixed position and therefore also determines the height of the pol-axis.
5. Set the height (y-axis) of the pol-axis to the height of the ϕ-axis.
6. The position of the pol-axis on the x-axis should coincide with the ϕ-axis.
7. Adjust the direction in which the pol-stage is pointing.
8. Align the ϕ-stage horizontally and vertically with the z-axis and the gravitational vector .
9. Fine-tune the alignment with the electrical alignment tool.

Pre-calibration preparation:

Before the calibration procedure is started, it is important to index all the axes. Indexing entails moving the axes of the system to their respective zero positions. This is necessary because if any adjustments need to be done to the

system when it is calibrated, it is necessary to start from a known position.

As mentioned in chapter 2, the measuring facility does not only have a spherical near-field scanner, but also a planar near-field scanner and the option of far-field measurements. These different scanners are all integrated. The probe of the SNF-scanner is also the probe of the PNF-scanner. This is shown in figure 2.20.

The x- and y-axis zero position is the position of the probe of the SNF-scanner. These axes have hard stops, implemented with a limit switch at the furthest point on the negative axes. An index offset is pre-programmed in the NSI-software. When the x-axis is indexed, the tower on which the pol-stage is mounted moves slowly in a negative direction towards the limit switch. When the switch is touched, the tower moves back with a predetermined offset distance. This is the $x = 0$ position.

The $y = 0$ indexing is done much in the same way, except that the tower is stationary and the pol-stage move in a negative direction on the y-axis until it hits the y-axis limit switch. The pol-stage then travels back the pre-set distance to the $y = 0$ position.

The three rotational axes (θ-, ϕ- and pol-axis) all have soft limits. These axes are able to rotate much further than 360°. The zero positions of the ϕ- and pol-axis rotational axes are not that critical, because during measurements the AUT's and the probe's levels must always be fine-tuned with the precision level. It does however make sense that the zero position is close to the middle of the angular range in order to avoid hitting a limit switch during measurement. The θ-axis' zero position on the other hand, is critical, because it determine the ϕ-axis direction on the horizontal plane.

The indexing of the rotational axes is done in the same manner as the x- and y-axis and this is done by using the NSI-software indexing option. The selected stage rotates slowly in a negative direction, until it gets to the the soft limit and then rotates back by a pre-determined angle.

Laser calibration:

One of the critical tools used in the evaluation process of the chamber is a Bosch GPL5E 5-point laser. A check was done to ensure the performance of this instrument was within specification. The evaluation was done in accordance with the manufacturer's instructions. The three axes of importance to our evaluation of the SNF-scanner are the two lateral axes and the vertical axis from the laser to the ground.

To check whether the lateral beams are aligned, the laser is mounted on a tripod and shone onto a wall a distance away, as can be seen in figure 3.5a. The position of the beam marked on a piece of paper. The laser is rotated through 180° and the position of the beam is marked again. The vertical difference in height between the beam positions is recorded. It is worthwhile to note that an increased distance accentuates the difference in height.
The manufacturer specifies an allowable error of 0.3 mm/m. The following results were recorded:

$$\begin{aligned} \text{Distance measured: A} &= 12.3 \text{ m} \\ \text{Acceptable error} &= \text{A x } 0.3 \text{ mm/m} \\ &= 3.7 \text{ mm} \\ \text{Height measurement: d} &= 2.5 \text{ mm} \end{aligned}$$

The vertical beam orthogonality was checked by placing a mirror on the ground to reflect the beam back to the laser. The height of the laser was also increased to maximise the beam travelling distance. The distance between the incoming and the outgoing beam was measured as seen in figure 3.5b.
When applying the manufacturers formula the following result was recorded:

$$\begin{aligned} \text{Distance measured: B} &= 1.95 \text{ m x } 2 = 3.9 \text{ m} \\ \text{Acceptable error} &= \text{B x } 0.3 \text{ mm/m} \\ &= 1.17 \text{ mm} \\ \text{Difference measured: d} &= 1 \text{ mm} \end{aligned}$$

The laser's performance was evaluated according to the manufacturer's calibration procedure and it was found to be within specification.

Centre of rotation:

When making reference to the centre of rotation, it is the θ-stage's centre of rotation that is referred to. This point is determined by a 4-point technique. A piece of cardboard is placed over the θ-stage and the laser is pointed to the proximity of the centre of rotation. The SNF-scanner is rotated to four positions, 0°, 90°, 180° and 270°. At each angle the position of the laser is marked. The intersection of connecting lines between the 0° and 180° positions and the 90° and 270° positions, is the centre of rotation.
The laser is then set to a position where the vertical beam of the laser points to this intersection.

Height of the ϕ-stage:

As mentioned in the introduction of section 3.2.3, the height of the ϕ-stage determines the height of the SNF-scanner. Therefore the next step is to align the

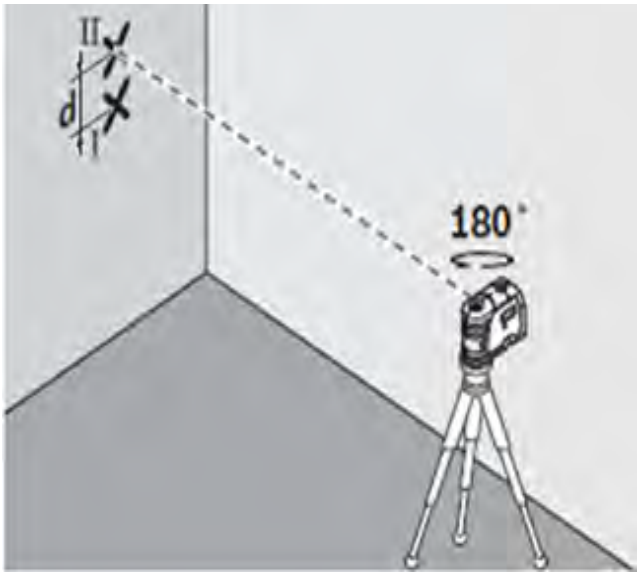

(a) Lateral beams evaluation

(b) Vertical beam evaluation

Figure 3.5: Laser calibration

horizontal beam of the laser with the height of the ϕ-stage, while at the same time keeping the vertical beam pointing to the θ-axis' centre of rotation. The alignment of the horizontal axis of the ϕ-stage is not important at this point of the calibration. It will be set later in the process. A custom made target plate is fitted to the ϕ-stage and the height of the laser adjusted accordingly. The set-up is displayed in figure 3.6. It is very important that the laser is not moved after the vertical and horizontal position is established.

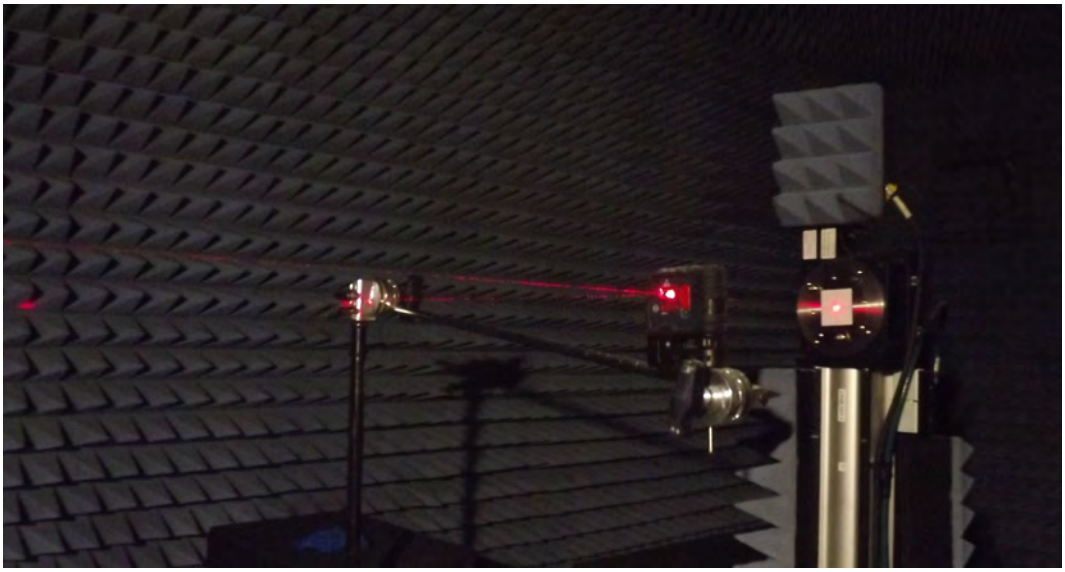

Figure 3.6: Laser mounted in chamber to calibrate the system

Height of the pol-stage:

The height of the pol-stage is set by placing the target-plate in the centre of the pol-stage and moving the pol-stage up or down on the PNF-scanner's y-axis until the target plate is vertically aligned with the lateral beam of the laser. The target-plate mounted on the pol-stage with the laser directed to the plate can be seen in figure 3.7a. The lateral beams of the laser indicate the centre-line of the the range. The index-offset of the NSI-software needs to be adjusted with the delta offset on the y-axis. The procedure to accomplish this can be found in the NSI2000 software manual [15].

Horizontal position of the pol-stage:

As discussed in the pre-calibration preparation, the probe can be moved on the x-axis of the PNF-scanner. The pre-set index offset of the x-axis can be modified in the same manner as the y-axis offset if it is found that the pol-stage does not align horizontally with the range centre line.

Optimise the pol-stage pointing:

For a perfectly aligned pol-stage, its interface surface must be flat with respect to the x/y-plane. To perform this check, the target plate is replaced by a mirror. An available script "TestMove.bas" allows the operator to continuously rotate the pol-axis and observe to the pattern of the reflected laser beam in the window of the laser. Shim stock can be used to adjust the pol-stage tilt in order for the reflected beam to form a circle with its centroid around the outgoing of the laser. The allowable radius of the circle is 10 mm.

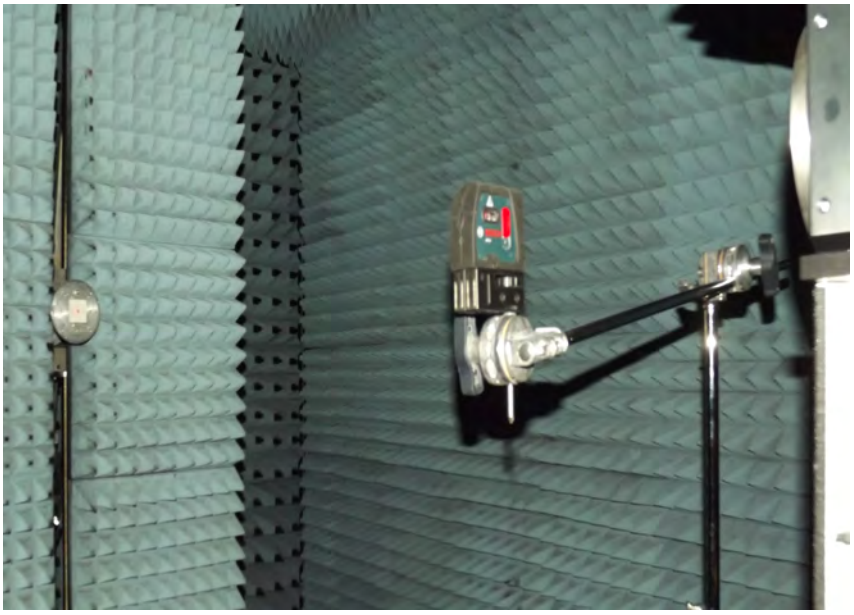

(a) Target mounted on the Pol-stage

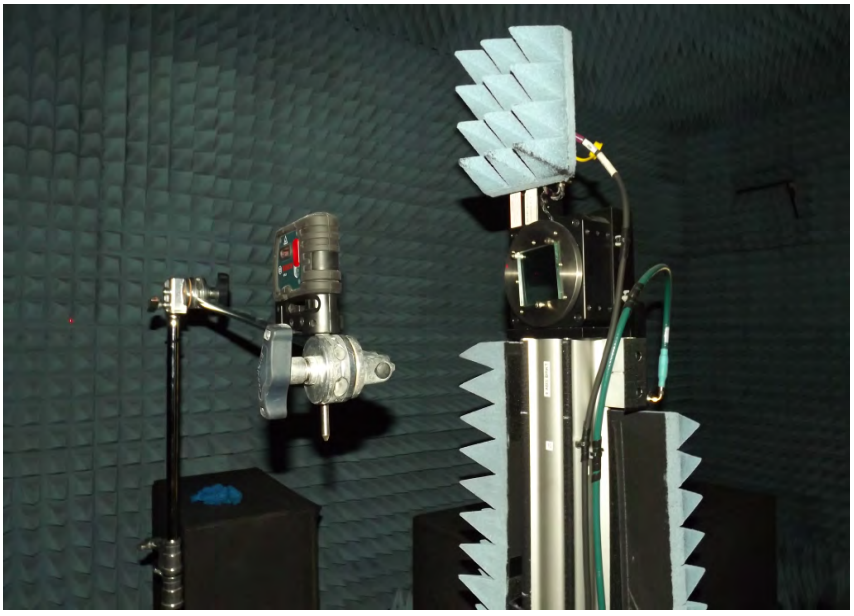

(b) Mirror mounted on the ϕ-stage

Figure 3.7: Evaluation and adjustment of pol- and ϕ-stage

ϕ-stage alignment:

The ϕ-axis must be parallel to the centre-line of the system, intersecting the θ-axis and also be normal to the gravitation vector. The ϕ-stage target plate is replaced by the mirror. The index offset of the θ-stage needs to be recorded for later use. By running the "TestMove.bas"-script, the ϕ-stage is put in a continuous mode of rotation. The reflected beam pattern can be observed on

the laser. Rotate the θ-axis until the centre of the circle is horizontally aligned with the outgoing beam from the laser. The tilt of the stage can be adjusted by losing the four bolts of the ϕ-stage and placing shim stock underneath it. It is only necessary to modify the vertical tilt. The horizontal alignment is accomplished by rotating the θ-stage. When the trajectory of the incoming beam is within the allowed radius of 5.08 mm of the outgoing beam, the ϕ-stage's alignment is within the allowed specification. The θ-axis index offset is changed to the sum of the original value plus the value of the new position. This new index offset is saved as part as the NSI2000-software default values.

Electrical alignment:

An electrical alignment technique was developed and presented at the 1998 AMTA symposium by Newell and Hindman [27]. It was incorporated in a script that forms part of the NSI2000-software. This script is able to detect the following two aspects of mechanical misalignment:

- θ-stage zero error: the ϕ-stage vector is not pointing directly into the pol-stage vector when $\theta = 0°$.
- Non-intersection of the ϕ- and the θ-axis.

The script is able to address and correct first the misalignment issue, but the second problem must be manually corrected. The script performs a flip-test, which entails taking a horizontal cut of the AUT, rotating the AUT through 180° and remeasuring the horizontal cut. By comparing the amplitude patterns of the two cuts, the θ-stage zero error can be calculated and corrected. Figure 3.8 show the flip-test results, before and after correction. The phase pattern is used to determine the off-set between axes and will recommend what mechanical adjustments must be made to minimise the error.

A good signal-to-noise ratio is essential for an accurate flip-test. To optimise the signal-to-noise ratio, the IFBW and the output power level of the PNA-X can be adjusted by the NSI2000-software internally. Refer to the software operational manual [15] for instructions on how to accomplish this.

Figure 3.9 displays the calculated misalignment of the flip-test before and after adjustments were made. It is clear how effective this method is to validate and rectify the θ-stage zero misalignment.

In summary, mechanical related errors are difficult to assess and a study by Hansen was used to show that on SNF-scanners, errors due to mechanical misalignment have a small influence on the uncertainty of a measurement. This statement, however, is only valid if the scanner's set-up is done with precision and the alignment is within the allowed specification of the system.

A comprehensive alignment process was presented and performed on the system. It is a tedious procedure to do the alignment properly, but it is a

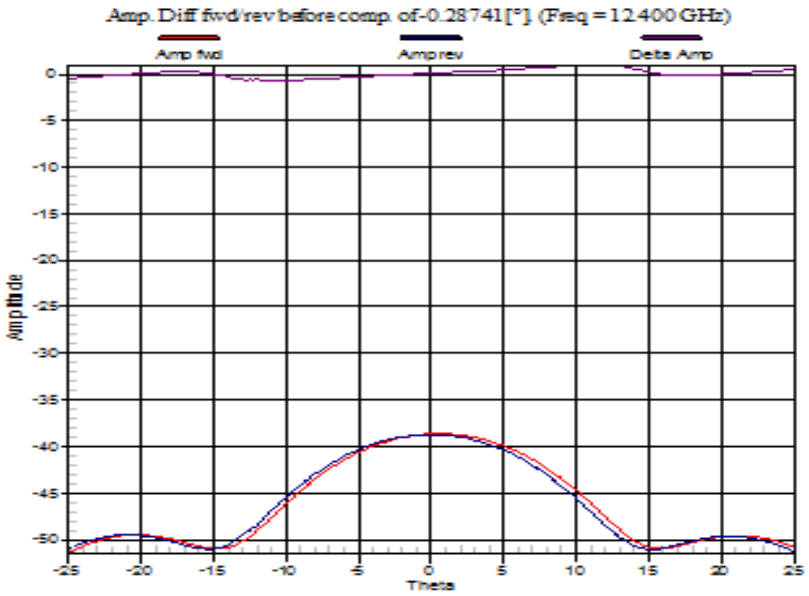

(a) Flip test before correction

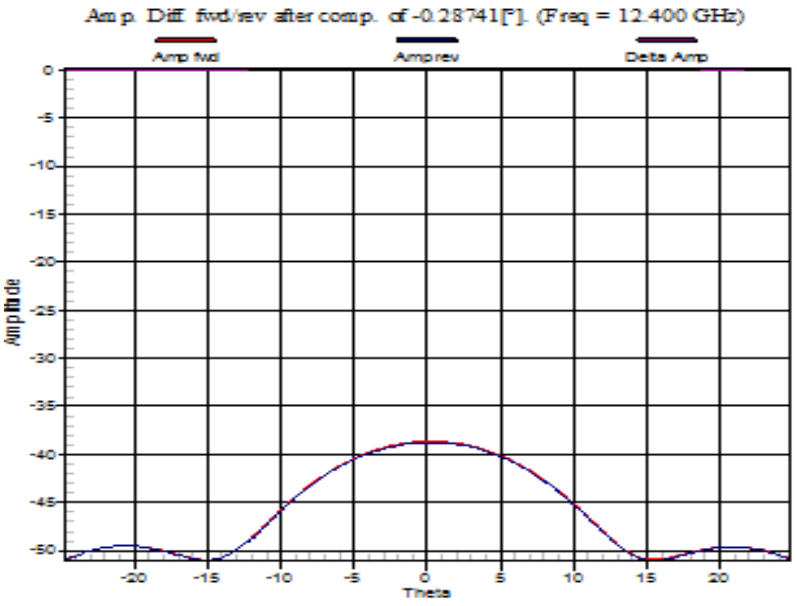

(b) Flip test after correction

Figure 3.8: Electrical alignment script's output - forward and reverse horizontal cut

process that can not be neglected because misalignment will have an influence on the accuracy of the measurements.

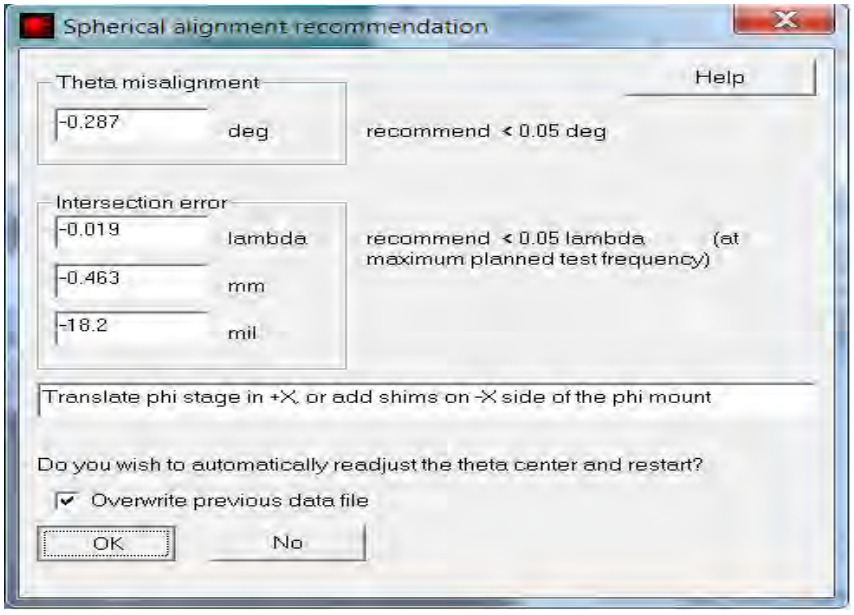

(a) Electrical alignment evaluation before corrections

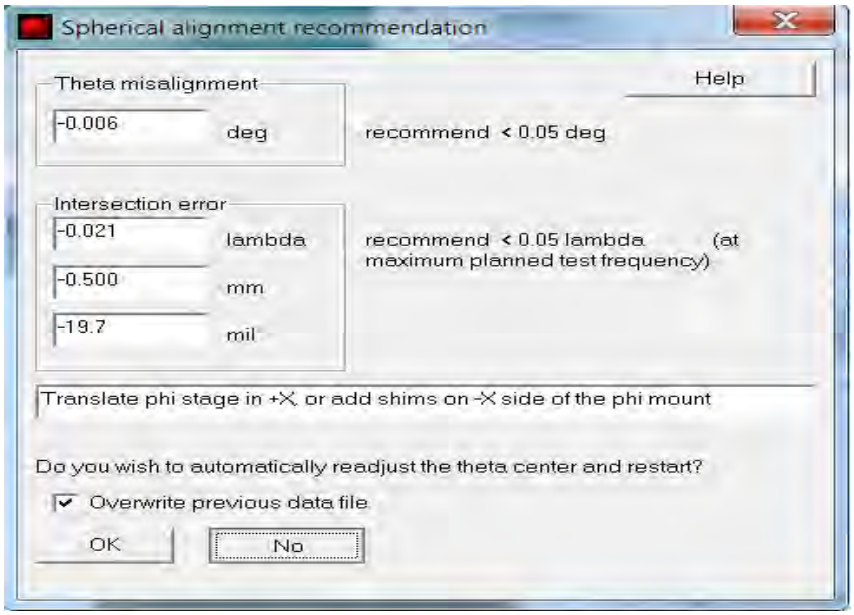

(b) Electrical alignment evaluation after corrections

Figure 3.9: Electrical alignment script results

3.3 Absolute power level related errors

These measurements have only an influence on the gain uncertainty budget and not on the shape of the radiation pattern.

3.3.1 Gain standard

As mentioned in section 2.4.3, this error term applies to comparative gain measurements and not to the absolute measurements done at the University of Stellenbosch. This error term is therefore not applicable to the current measurement processes and will not be assessed.

For use as a reference in the future, standard gain horns that comply with the U.S. Naval Research Lab Report Report No. 4433, (NRL standard gain horns) may be used. The gain uncertainty of these is ±0.3 dB according to the NSI2000 software operating manual and this value is used in the gain uncertainty budget [15].

3.3.2 Normalisation constant

The normalisation constant was measured by repeating the same measurement a few times. The only difference between the measurements was that the cables to the probe and AUT were fastened and loosened in between measurements. The temperature was kept constant for the duration of the measurements.

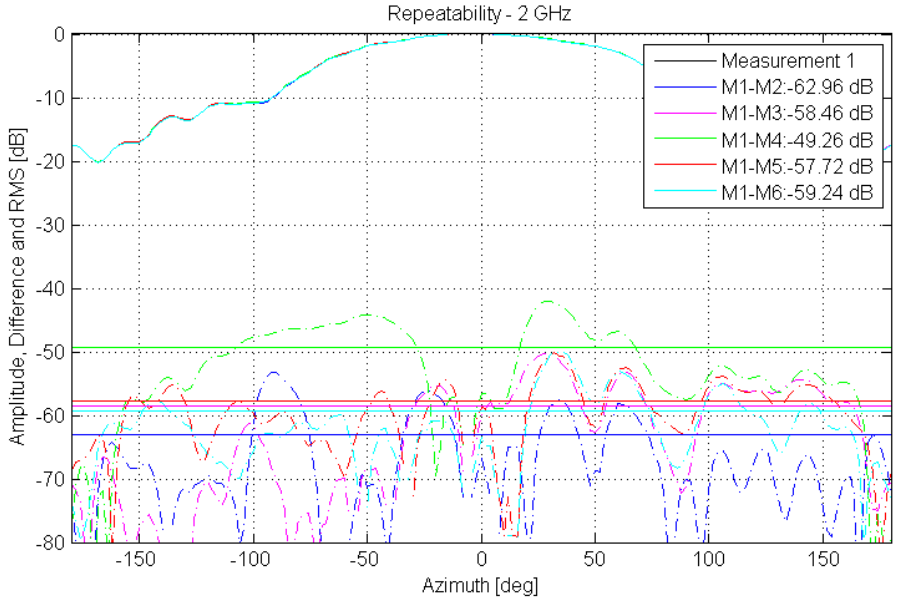

Figure 3.10: Repeated measurement, difference between measurement 1 and sequential measurements

The results of the measurement are shown in figure 3.10. All measurements were completed within a time-frame of 3 hours. As can be seen, the biggest deviation was between the first and the fourth measurement. An RMS-value of -49.26 dB was calculated between the difference of these two measurements. This represents an uncertainty of 0.03 dB for the main lobe and, since absolute

power levels are considered, it is not necessary to calculate the uncertainty on the sidelobe level.

3.3.3 Impedance mismatch error

Impedance mismatch errors do not apply to realised gain that is measured using the two- and three- antenna gain measuring method. The two- and three-antenna gain methods fall under the category of absolute gain measurement methods. This is discussed in section 2.4.3 and depicted in figure 2.1. The reason is that when absolute gain measurements are done as is the case when the two- and three-antenna gain measurement method are used, the impedance mismatch form part of the measured gain. For this reason, impedance mismatch errors are not considered in this evaluation.

3.3.4 Absolute gain methods evaluation and results

To evaluate the accuracy of the absolute gain methods that are done at the measuring facility of the university, antennas with published gain values were measured and the results were compared with the known results. As stated in section 2.2.2 the absolute gain method-measurements must be done in the far-field of both antennas.

Two types of calibration can be done. The first and most common calibration type used at the facility is the "thru"-response calibration. A full two-port calibration can also be performed, but it takes much longer and is only done in special circumstances.

Comparing results of the two- and three-antenna gain methods

To compare and evaluate the two-antenna gain method, the results of such a measurement were compared with results from a different measurement of the same antenna. The measurement used for the comparison is described in the next sub-section. It formed part of the evaluation of three-antenna gain method. Equation 2.2.5, the formula for the gain of the two-antenna gain method, is used to calculate the gain of the antennas.

The set-up for the two antenna measurement:
Antennas: AEL-1 2-18 GHz, AEL-2 2-18 GHz
Frequency range: 2 - 5 GHz
Output power: 10 dBm
IF Bandwidth: 10 kHz
Calibration: Thru response calibration

The set-up for the three-antenna gain method:
Antennas: AEL 2-18 GHz, EMCO MODEL 3115 and NSI-RF-RGP10

Frequency range: 2 - 10 GHz
Output power: 10 dBm
IF Bandwidth: 10 kHz
Calibration: Thru response calibration

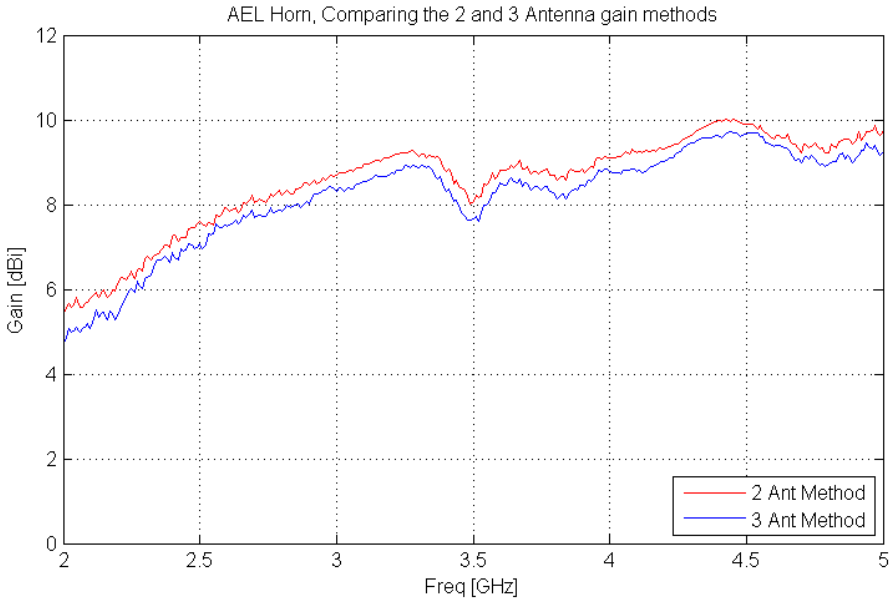

Figure 3.11: Comparison 2 and 3 antenna measurement method

As can be seen in figure 3.11, the results are within 1 dB of each other.

Evaluating the three-antenna gain method

To evaluate the three-antenna gain method, measurements were done which include the EMCO model 3115 horn antenna and the NSI-RF-GRP10 probe. These two antennas were chosen because the published gain values are available and the results of the three-antenna gain measuring method could be compared to the published values. Two sets of measurements were done in order to cover the whole frequency band of the antennas.

Low frequency band measurement:
Antennas: EMCO MODEL 3115, NSI-RF-RGP10 and the Schwarzbeck SBA9113 bi-conical antenna
Frequency range: 0.75 - 3 GHz
Output power: 10 dBm
IF Bandwidth: 10 kHz
Calibration: Thru response calibration

High frequency band measurement:
Antennas: Antennas: EMCO MODEL 3115, NSI-RF-RGP10 and AEL 2 - 18 GHz
Frequency range: Frequency range: 2 - 10 GHz
Output power: 10 dBm
IF Bandwidth: 10 kHz
Calibration: Thru response calibration

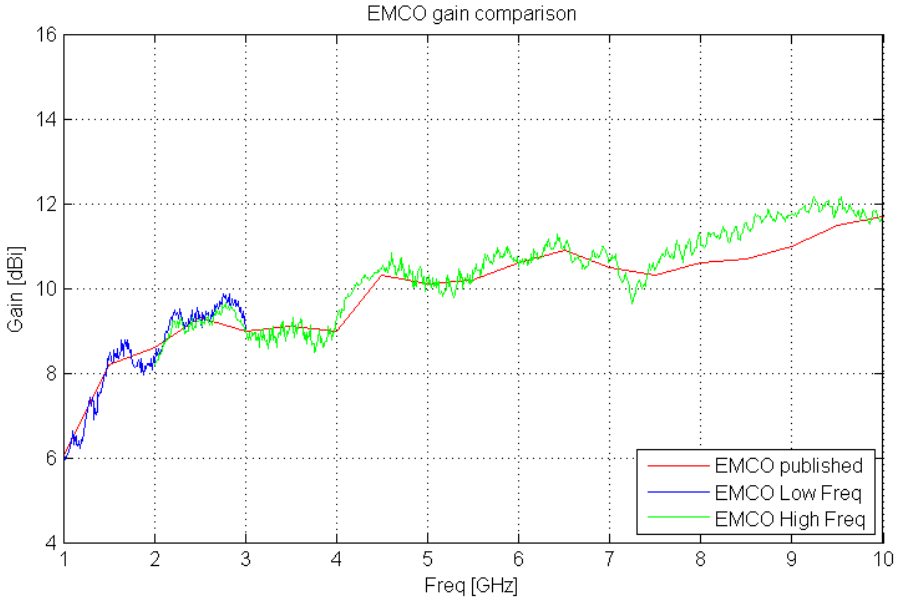

Figure 3.12: EMCO Model 3115 measured and published results

Equations 2.2.6 - 2.2.8 are used to calculate the gain of the three antennas. The results are displayed in figures 3.12 and 3.13. The results are within 1 dB of the published values.

In summary, with the instrumentation available, gain measurements are possible to within 1 dB of what would be considered the absolute truth.

3.4 Processing related errors

3.4.1 Aliasing

As described in section 2.4 aliasing can be avoided if the sampling criteria are satisfied. In the case of linear scans, the Nyquist sampling criteria must be met and when angular scans are done, the minimum number of samples on the circumference of the sphere is described by equation 2.4.5 and 2.4.6.

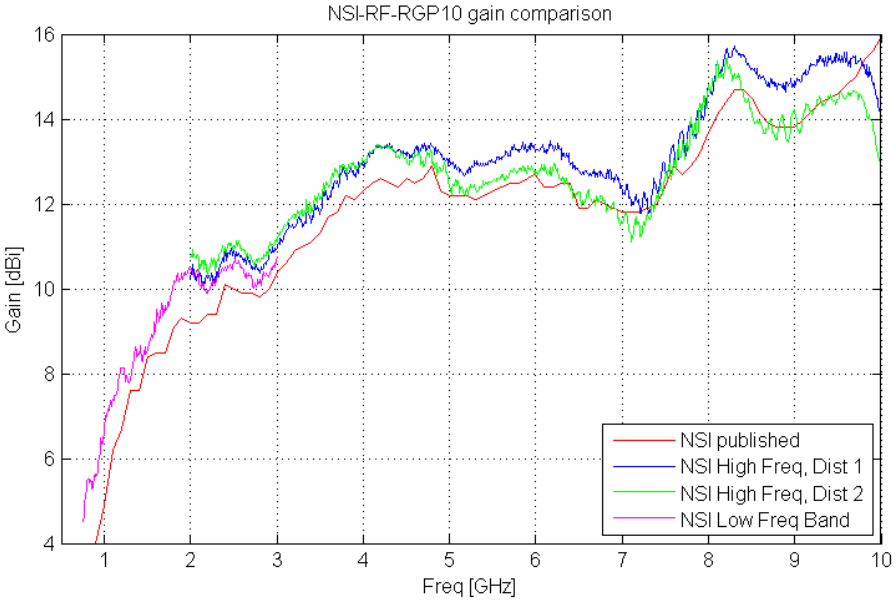

Figure 3.13: NSI-RF-RGP10 - varied distances and methods

When this is adhered to, the highest order spherical modes that still contain a significant amount of power, are captured.

To illustrate this, the AEL horn was measured at 5 GHz. The maximum radial extent (MRE) was 0.148 m and λ at 5 GHz is 0.060 m.

$$\begin{aligned} N &= \left(\frac{2\pi MRE}{\lambda}\right) + 10 \\ &= \left(\frac{2\pi 0.148}{0.06}\right) + 10 \\ &= 15.50 \end{aligned} \tag{3.4.1}$$

$$\begin{aligned} \Delta\theta = \Delta\phi &= \frac{360^\circ}{2N+1} \\ &= 6.93^\circ \\ &\approx 6^\circ \end{aligned} \tag{3.4.2}$$

The angular step size needs to be adjusted to comply with the software requirements that 360° must be a multiple of the step size. In other words, there should be an integer multiplied by the step size that has 360° as a result; the angular step size value should not be smaller than 0.125° and not larger than 10° [15]; $\Delta\theta$ and $\Delta\phi$, must be rounded down to avoid violating the sample density conditions.

Figure 3.14 displays the results of the recommended test for aliasing. A benchmark measurement with the suggested sample density of 6° was done. A second scan with half the first sampling increment was done and compared to

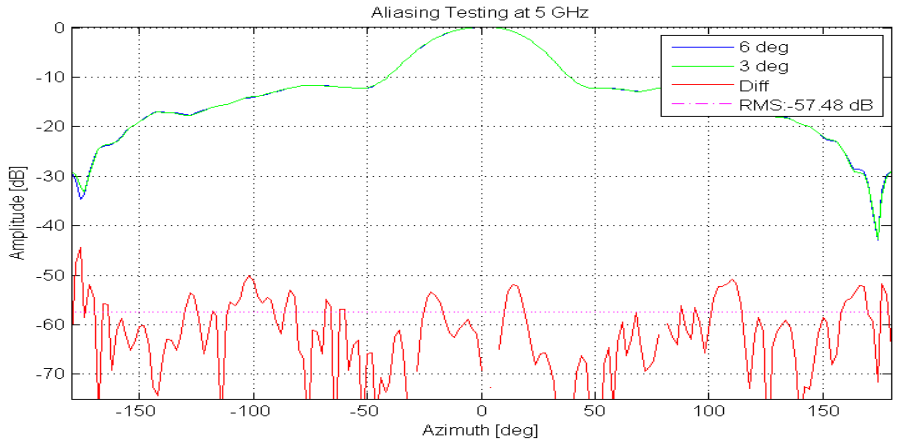

(a) Over sampled, 6° vs. 3°

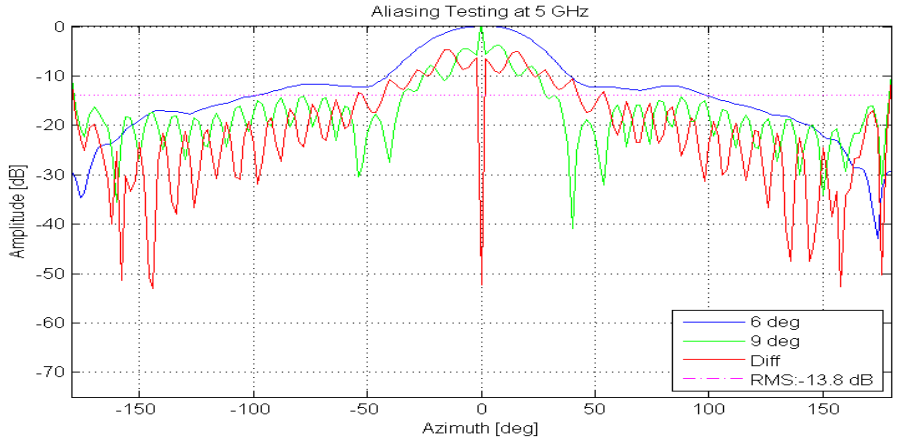

(b) Under sampled, 6° vs. 9°

Figure 3.14: Over- and under-sampling compared with the recommended sampling density

the first. If there is no significant difference between the two measurements, it can be concluded that the recommend sampling density is sufficient. It is clear from figure 3.14a that there is almost no difference when the sampling density is doubled. The RMS value of -57.48 dB renders an uncertainty of 0.012 dB.

An under sampled scan, with an angular increment of 9° was also done and compared with the benchmark test. From figure 3.14b it is obvious that to sample below the recommended sampling criteria are disastrous.

According to the specifications of the stepper motors used at the measuring

facility, the following are the minimum increments achievable:

X-axis 0.025 mm
Y-axis 0.0125 mm
Pol-axis 0.0125°
θ-axis 0.0125°
ϕ-axis 0.0125°

Therefore, the motor's minimum increment makes it possible to avoid aliasing because the recommended step size is always achievable. It is, however, one of the common errors that occur when the MRE of the set-up is not measured correctly. Fortunately, when it occurs, it is quite obvious because results similar to figure 3.14b are obtained, which is easy to rectify.

3.4.2 Measurement area truncation

Measurement area truncation is more problematic in PNF-scans than SNF-scans because the scan area must be large enough to capture most of the radiating energy and the neglected portion should not influence the near- to far-field transformation.

It was stated in section 2.4.4 that near-field scan extent must be large enough that the power level at the span edge should be at least -30 dB below the peak value to avoid the influence of data truncation [3]. The effect of neglecting the recommendation is demonstrated in figure 3.15. Four SNF-scans, with a decreasing θ-span were done (figure 3.15a). As soon as the recommendation was ignored the error became clearly visible, as can be seen in the transformed far-field patterns in figure 3.15b.

A closer look is taken at the effect of data truncation in figure 3.16. To make a valid comparison, the patterns were only compared from θ $-40°$ to 40°. It is clear how significant the error becomes when the -30 dB recommendation is ignored. The RMS-value of -19.65 dB for the 40°-span renders an uncertainty of 0.86 dB and the RMS of -24.49 dB causes an uncertainty of 0.50 dB, whereas the uncertainty for the 90°, which was the only scan that heeds the recommendation, is only 0.03 dB.

It is therefore appears that data truncation should not be a problem, as long as the "at least -30 dB"-recommendation is adhered to or the spherical scan is done over a full sphere.

3.5 RF sub-system

3.5.1 Receiver amplitude linearity

The proposed method by the NSI Software Maunual [15] to determine the receiver amplitude linearity, is to perform two near-field scans. One is done

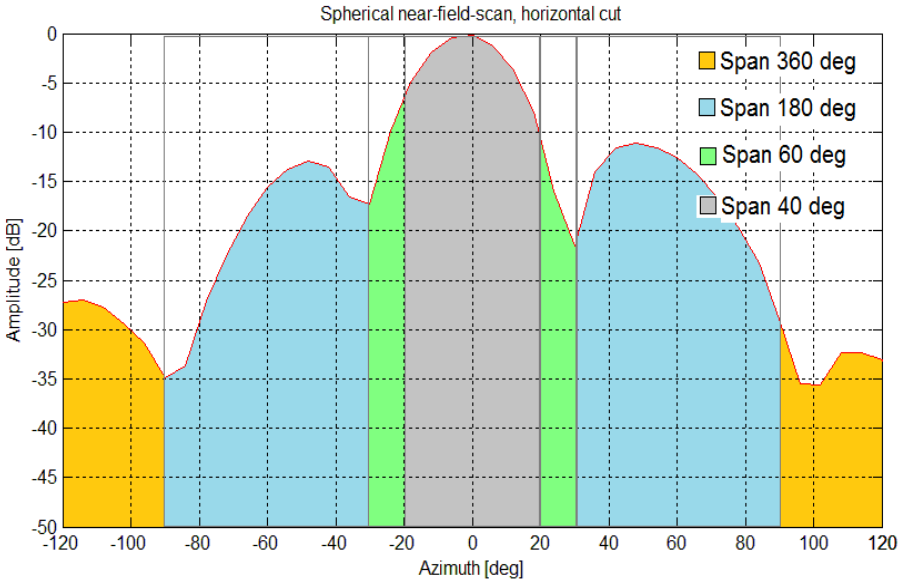

(a) Unprocessed near-field-data, different spans used for far-field transformation

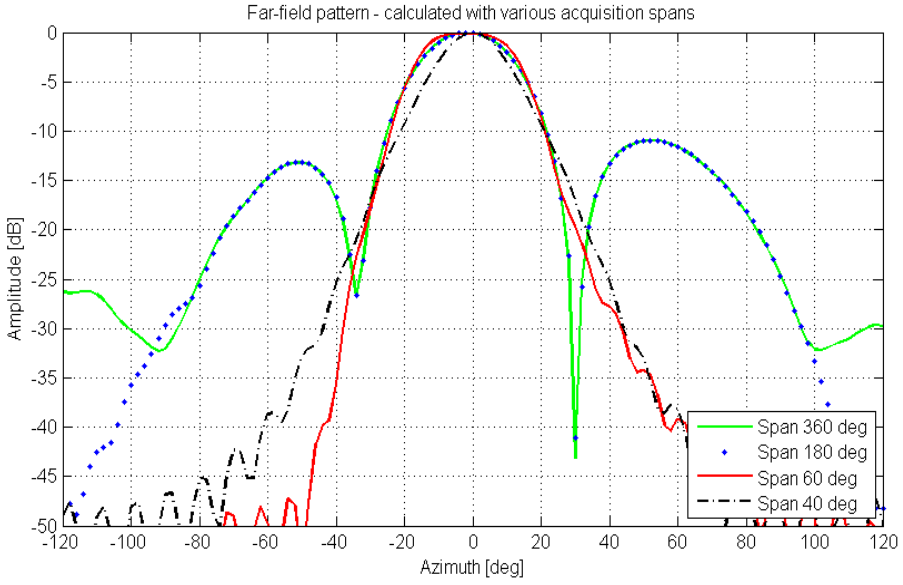

(b) Far-field radiation patterns, with different near-field data capturing spans

Figure 3.15: The effect of data truncation in the near-field is visible in the far-field radiation patterns

with a standard set-up, and repeated with 30 dB attenuation added. The difference between the transformed far-fields is determined and the RMS value calculated, which in turn is used to compute the uncertainty.

Figure 3.17 shows the results of such a test in the Stellenbosch anechoic chamber. The AEL 2-18 GHz horn (as AUT) and the NSI-RF-RGP10 (as probe) were used in the set-up. This antenna selection limits the frequency

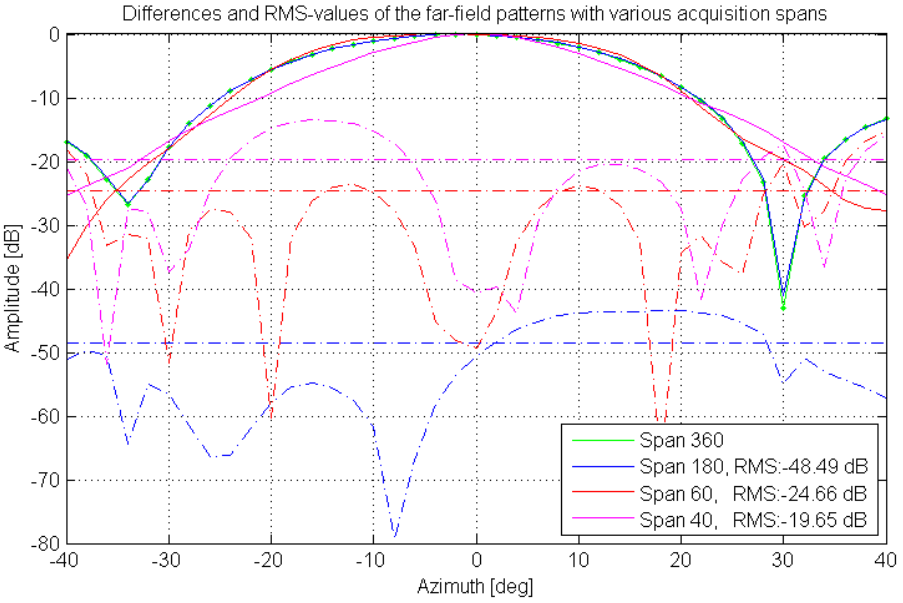

Figure 3.16: The difference between the 360 degrees span measurement and various narrower spans

band of the test to 2 - 5 GHz, since this is the overlapping frequency band of the antennas utilised. As can be seen in figure 3.17 at 2 GHz, an RMS-value of -50.27 dB was calculated. The uncertainty associated with -50.27 dB is 0.027 dB for the main beam and 0.804 dB for the -30 dB sidelobe level.

Although this is the proposed test for amplitude linearity, the noise on the 5 GHz pattern can be attributed to the fact that the amplitude level is below -95 dB when the 30 dB attenuation is added. This is confirmed in figure 3.23b, a figure that shows the dynamic range of the facility. The results of this particular test at higher frequencies become inconclusive because the amplitude of the received signal is not significantly higher than the noise floor.

What became clear is that the operator should ensure that the power level is significantly higher than the noise floor.

3.5.2 System phase error

As part of the near-to-far-field transformation, complex number data is required. Therefore phase stability and not only amplitude stability is important. According to Parini [10], receiver stability, cables and rotary joints are the the biggest contributing factors to the phase stability of a measuring range.

To investigate the changes in phase over time, the phase variation was observed by taking nine S21 measurements, with a time lapse of 20 minutes between measurements, as shown in figure 3.18. The temperature inside the chamber was also monitored and a drift of 2° in temperature was recorded. During this period no changes to the system were made. The S21-

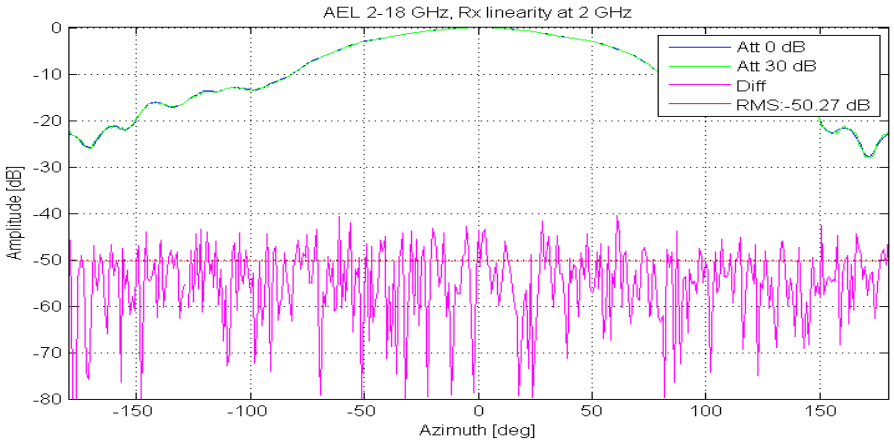

(a) 2 GHz, 0 dB, 30 dB attenuation and RMS

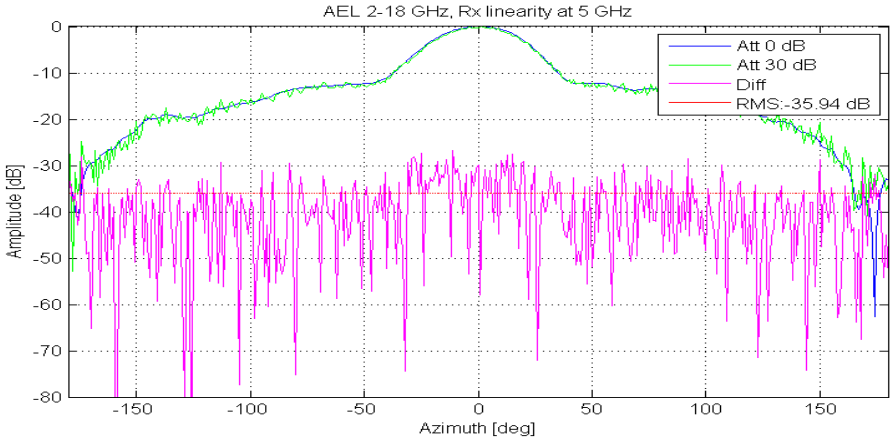

(b) 5 GHz, 0 dB, 30 dB attenuation and RMS

Figure 3.17: RX Linearity test, AEL 2-18 GHz Horn

measurements were done after a full two-port calibration was performed inside the chamber. The frequency band (2 - 10 GHz) for the measurements was determined by the combination of the two antennas used, the NSI-RF-RGP10 horn and the AEL 2-18 GHz horn. The separation distance between antenna apertures was 1.2 m.

The standard deviation of the phase for the nine measurements was calculated by using equation 2.3.11. The standard deviation was plotted over frequency and the results are plotted in figure 3.18c. For the sake of completeness the standard deviation of the amplitude is displayed in figure 3.19.

It can be seen that above 6.5 GHz the phase become less stable and more variances can be observed. For measurements higher than 8.2 GHz, an amplifier is usually used in the system to compensate for the chamber's diminished dynamic range, as will be discussed in section 3.5.4.

The introduction of an amplifier would change the dynamic of the system

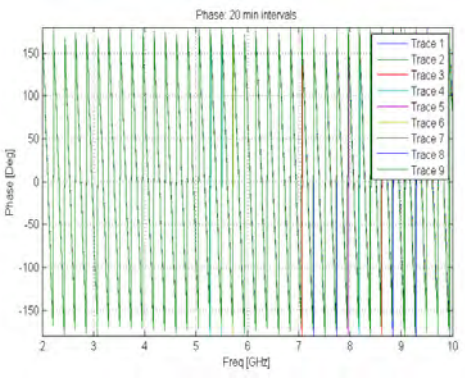

(a) Phase plots at nine instances

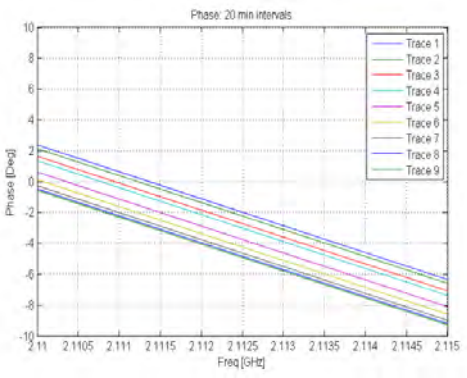

(b) Frequency snippet of phase variation

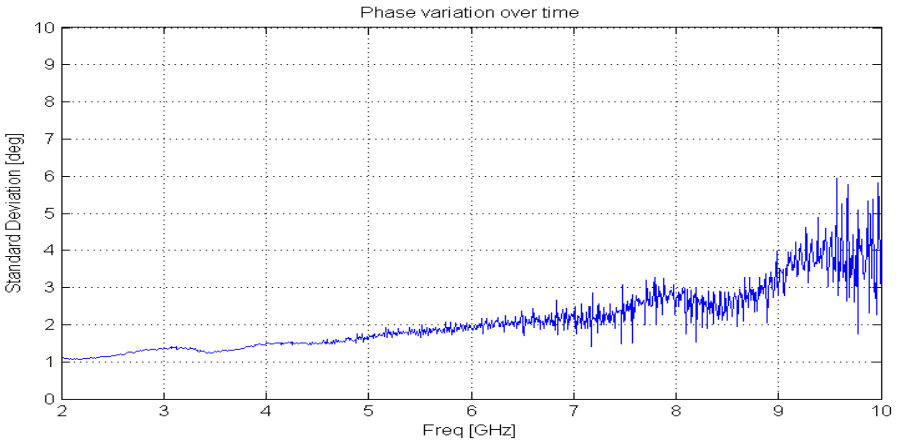

(c) System Phase Error

Figure 3.18: Variation and standard deviation of phase over time

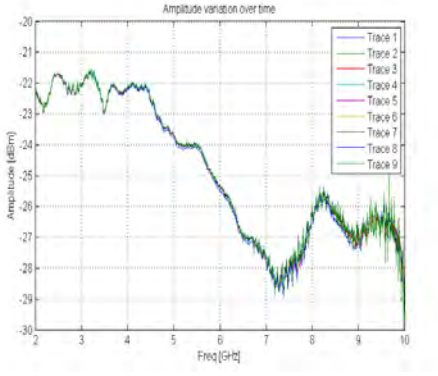

(a) Amplitude variation over time

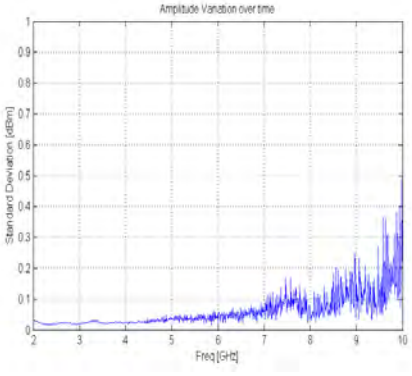

(b) Standard deviation

Figure 3.19: Variation and standard deviation of amplitude over time

and produce different results. The added amplifier is not evaluated as part of this investigation into the chamber's performance.

The phase variation as a result of the movement of the rotary joints and

Frequency [GHz]	**Magnitude (dB/°C)**	**Phase(°/°C)**
0.5 - 3.2	0.01	0.29
3.2 - 8.5	0.02	0.13
8.5 - 10.0	0.02	0.13
10.0 - 13.5	0.02	0.13
13.5 - 16.0	0.02	0.13
16.0 - 20.0	0.03	0.40

Table 3.2: PNA-X specification - stability over temperature

cables is not highligted in the above test, only the receiver's amplitude and phase stability or instability. The phase stability over temperature is an important factor to take into consideration. The specification of the PNA-X is shown in Table 3.2 [23].

The next aspect considered was the phase stability when SNF-scans are done. Three SNF-scans were done, over a time period of 2 hours.

During a SNF-scan the rotary joints in the θ-, ϕ- and pol-axis are rotating. However there is very little to no cable movement during a SNF-scan because it is possible to secure the cables in fixed positions. The raw near-field data is displayed in figure 3.20. It can be seen that there are extremely small changes in amplitude between all three measurements, but there is a more significant change in phase between measurement 1 and 3 than between measurement 1 and 2. When these near-field patterns are transformed to the far-field and compared (figure 3.21), it can be seen that there are more significant differences between the first and third measurement than between the first and second measurement. It can be concluded that since the amplitude is nearly constant, the cables are fixed, and the antennas are not removed from their mounting positions, the phase change must largely be responsible for the differences in the far-field patterns.

A conclusion can be reached that changes in phase can significantly contribute to errors creeping into measurements. This highlights the importance of taking precautions, such as keeping temperature constant and securing cables, to lessen phase changes during measurements as much as possible.

3.5.3 Leakage and crosstalk

Leakage and crosstalk in the system occur when a portion of the transmitted signal escapes somewhere along the transmission path and couples back into the transmit or the receive path. This is possible when, for example, a cable is broken or a connector not properly torqued.

To establish whether there is any leakage or crosstalk present, the following three SNF-scans are done: a standard SNF-scan, an SNF-scan in which the AUT feed-point (transmit-port) is terminated with 50 Ω, and an SNF-scan in

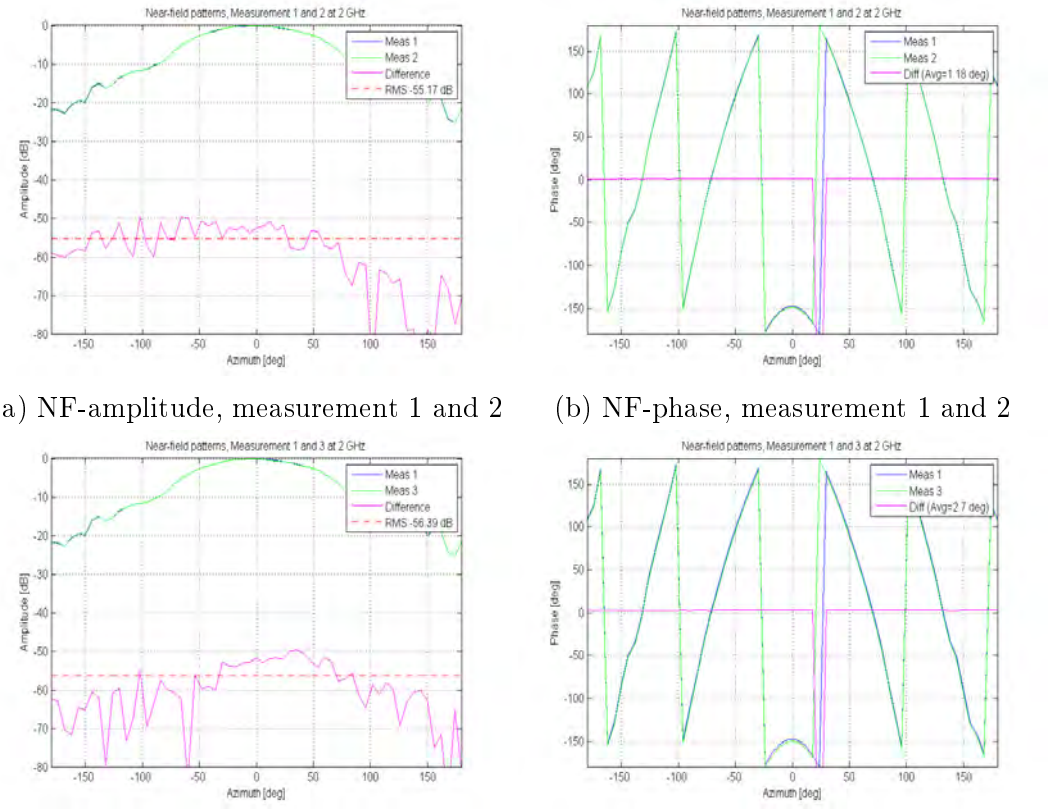

(a) NF-amplitude, measurement 1 and 2

(b) NF-phase, measurement 1 and 2

(c) NF-amplitude, measurement 1 and 3

(d) NF-phase, measurement 1 and 3

Figure 3.20: Near-field-amplitude and -phase comparison of measurements 1, 2 and 3

which the probe feed-point (receive-port) is terminated with 50 Ω. These near-field scans are then transformed to the far-field. In this test, the transformed far-field of the standard SNF-scan pattern is normalised to give a 0 dBm peak pattern value. The same offset value that was used to normalise the standard measurement, is added to the leakage patterns. By doing this, the leakage can be directly compared with the standard measurement patterns. The RMS-values of the far-field "normalised" leakage patterns are calculated. The RMS-value in this instance is the error-to-signal level. Once an error-to-signal level is established, the uncertainty can be calculated by using equation 2.3.7.

Two measurement sets were done to cover the frequency range from 750 MHz to 5 GHz. The first measurement was made using the Schwarzbeck SBA9113 bi-conical antenna to cover the range from 750 MHz to 3 GHz. The second measurement was performed with the AEL 2-18 GHz-horn to cover the range from 2 GHz to 5 GHz. Examples of the measurement results are displayed in figure 3.22. It is important to note that SNF-scans are relative measurements and no calibration is done. Therefore, internal leakage forms

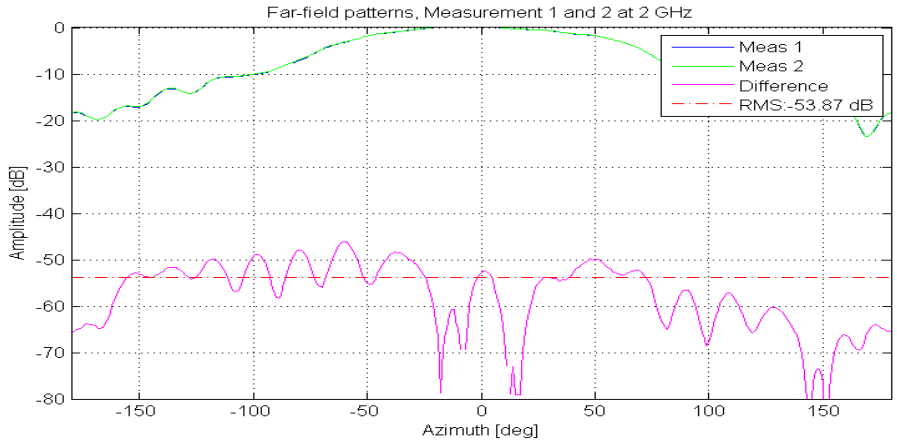

(a) Far-field pattern comparison of measurement 1 and 2

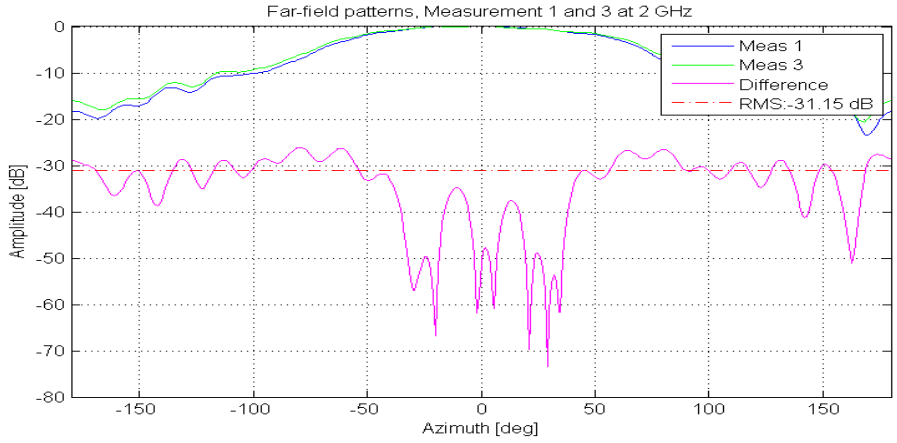

(b) Far-field pattern comparison of measurement 1 and 3

Figure 3.21: Far-field pattern comparison, with near-field phase variation as source for pattern differences

part of these results. The software and measurement set-up, do not make provision for doing a full two-port calibration, including isolation to rid the measurement of the internal leakage.

As with most of the tests in the NIST 18-term error analysis, the results are dependant on the set-up of the particular measurement. Therefore the results shown in Table 3.3 are only an indication of the system performance with regard to leakage and crosstalk. It can however be concluded that the system leakage and crosstalk are small and should not be a concern as long as components such cables and rotary joints are in excellent working condition.

3.5.4 Receiver dynamic range

According to the Agilent PNA-X specification sheet [23] (section on the corrected system performance), the receiver's dynamic range can be calculated

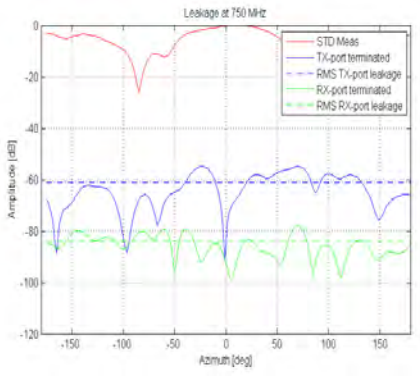

(a) 750 MHz

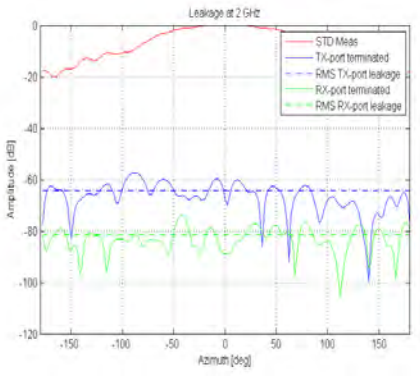

(b) 2 GHz

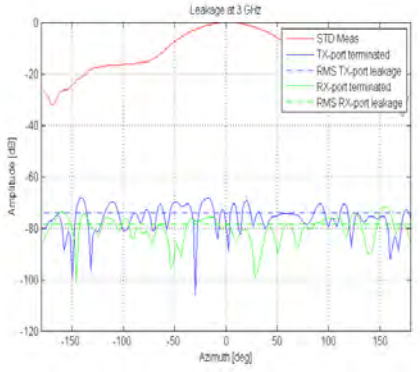

(c) 3 GHz

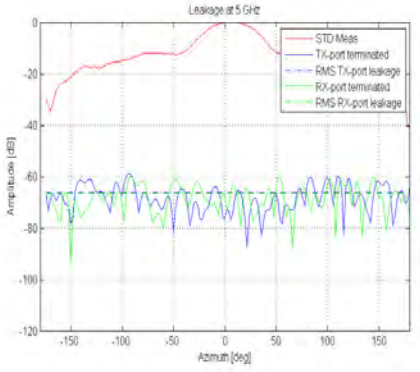

(d) 5 GHz

Figure 3.22: Leakage measurements

Freq [GHz]	**Tx-port: RMS**	**Uncertainty** Main	30dB SL	**Rx-port: RMS**	**Uncertainty** Main	30dB SL
0.75	-60.91	0.008	0.244	-84.05	0.001	0.017
2	-64.34	0.005	0.165	-81.35	0.001	0.023
3	-74.11	0.002	0.054	-78.47	0.001	0.033
4	-72.30	0.002	0.066	-73.20	0.002	0.060
5	-65.89	0.004	0.138	-66.25	0.004	0.133

Table 3.3: The measured leakage when firstly Tx-port and then the Rx-port were terminated. The associated uncertainty for the main and a -30 dB side-lobe level for each scenario are listed.

by taking the difference between the power level at which the receiver's test port is at 0.1 dB compression and the level at which the signal would be indistinguishable from the noise floor.

Table 19 of the PNA-X specification sheet [23], specifies the typical 0.1 dB compression point for the PNA-X input port as 13 dBm from 750 MHz to 18 GHz, the frequency range of interest. Since the system is lossy the input to

the receiver is limited to the incident power received. Therefore, the upper limit is set by the maximum levelled output of the PNA-X minus the loss of the system. The lower limit is the noise floor of the PNA-X. This is specified at -114 dBm at an IFBW of 10 Hz (Table 18, [23]).

The loss of the system has two components. The loss within the cables, rotary joints and adaptors are typically constant for a particular frequency, but there is also a component that is unique for every set-up. This portion is frequency dependent and determined by the distance between antennas and the antenna gains.

The linearity test of the system was done over two frequency bands to illustrate the degradation of the dynamic range as the frequency increases. The first using the AEL 2-18 GHz horn and the NSI-RF-RGP10 horn (probe) to cover the frequency range from 2 - 8.2 GHz, the second using an open-ended-waveguide probe (NSI-RF-WR9) in conjuntion with the AEL horn for the frequency range from 8.2 - 12.4 GHz.

The HP8496A stepped attenuator was placed in the transmission path at the transmit port of the PNA-X. Newell [25] suggests that one-dimensional cuts are sufficient for the test. Azimuth sweeps (S21-parameter over θ measurements) were done for each attenuation level. The effect of the attenuation can be seen in figure 3.23.

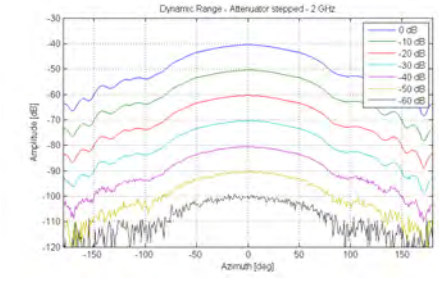

(a) 2 GHz, 0 dB to 60 dB attenuation

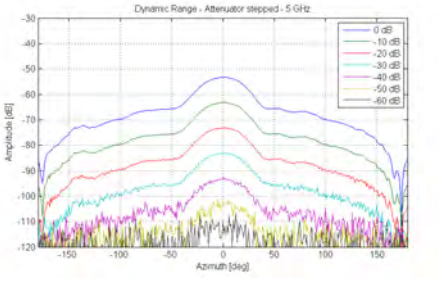

(b) 5 GHz, 0 dB to 60 dB attenuation

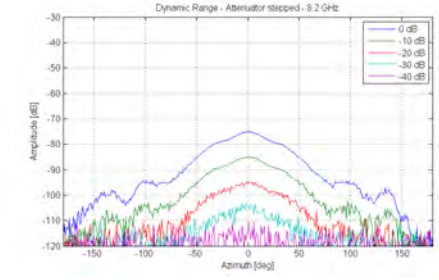

(c) 8.2 GHz, 0 dB to 40 dB attenuation

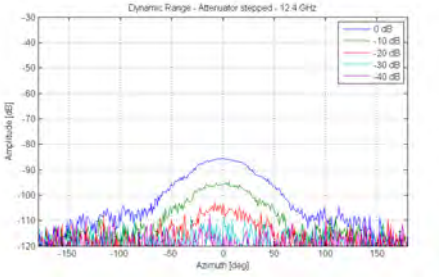

(d) 12.4 GHz, 0 dB to 40 dB attenuation

Figure 3.23: System dynamic range, AEL 2-18 GHz Horn

From these graphs we can conclude that the dynamic range diminishes as frequency increases. For this particular set-up (output power/antenna

gain/separation distance) the dynamic range at 2 GHz was about -70 dB. The effect of the noise floor begins to creep into the measurement results when the receive power level is in the order of -90 dBm below the output power of the transmit port. Figure 3.23d shows that the dynamic range at 12.4 GHz is only about 25 dB. This is due to the high loss at these frequencies, and the limits on the maximum levelled output power of the VNA.

A second approach was taken to confirm the measurement. The losses of the transmit and receive paths were physically measured using the Anritsu MS46122B VNA. These losses are a combination of cable loss and loss through connectors and rotary joints. Figure 3.24 gives a simplified block diagram of the components in the system. A power budget was composed using these measured results, namely the AUT gain, the probe gain, the free space loss and the output power of the VNA. The received power for the maximum output power determines the maximum power level of the system, and therefore the upper limit of the dynamic range. The lower limit is the noise floor which is specified as -114 dBm. The dynamic range is calculated by subtracting the noise floor from the received power. The results of this measurement can be seen in Table 3.4. These measured results correlate well with the scanned results seen in figure 3.23.

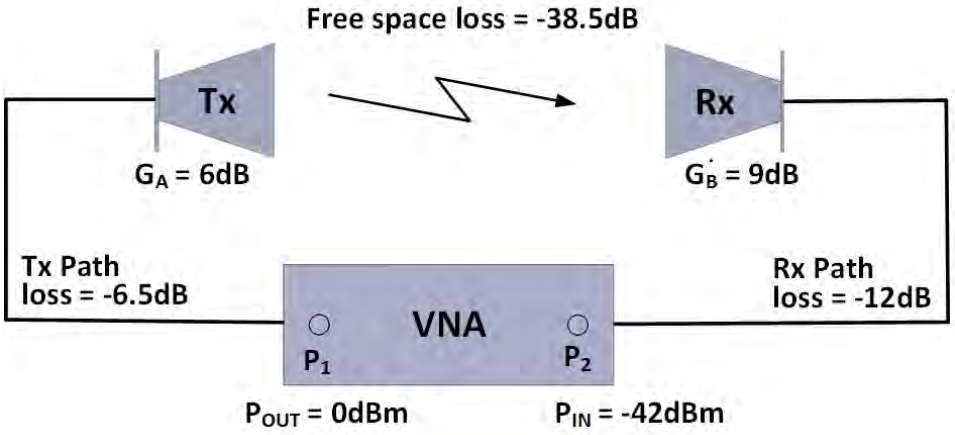

Figure 3.24: System block diagram, displaying as an example the measured gain/loss values of the system at 2 GHz

Another noteworthy aspect of dynamic range is that phase is more sensitive to the proximity of the noise floor than is amplitude. An output of the NSI2000-software is real-time amplitude and phase readings at specified frequencies. These were recorded during the step attenuator test and captured in Table 3.5. In most instances, displayed phase become unmeasurable with 20 dB less attenuation than when the amplitude disappears in the noise floor. Phase stability forms an integral part of the near-field to far-field transforma-

Freq [GHz]	**Tx Path [dB]**	**Tx Ant [dB]**	**FSL [dB]**	**Rx Ant [dB]**	**Rx Path [dB]**	**Rx Power [dBm]**	**Dynamic Range [dB]**
2	-6.55	6	-38.47	9	-12.12	-42.14	71.86
5	-10.49	9	-46.43	12.5	-18.58	-54.00	60.00
8.2	-13.52	11	-50.72	6	-23.07	-70.31	43.69
10	-15.56	11	-52.45	6	-25.5	-76.51	37.49
12.4	-16.99	11	-54.32	6	-28.71	-83.02	30.98

Table 3.4: Measured dynamic range, a noise floor of -114 dBm is used for calculations

tion and must certainly be taken into consideration when dynamic range is evaluated.

The practical implications are that when antennas are scanned in the near-field, sidelobes and nulls of the pattern will be affected first by a degraded dynamic range at higher frequencies. It is proposed that a power budget is used as a tool to determine at what stage an amplifier should be included in the system to enhance the dynamic range.

3.6 Environmental related errors - reflections

Reflections in an anechoic chamber can be one of the biggest sources of error and therefore contribute most to uncertainty in measurements [28]. Reflections that occur in the chamber can mainly be divided into two categories, namely reflections that are attributed to the structures within the chamber, and reflections from the chamber itself, such as the walls, floor and ceiling [10]. A contributing factor to the amount of reflection that is present in the chamber is the performance of the absorbing material and whether there is adequate or inadequate absorber coverage of the structures.

The performance of the anechoic chamber at the University of Stellenbosch at lower frequencies has always been under question because the chamber is primarily lined with 12" pyramidal absorbers. The 12" absorber's reflection performance is specified as -40 dB at 3 GHz, -35 dB at 1 GHz and -25 dB at 0.5 GHz [29].

The tests that were conducted to determine the reflections in the chamber, were therefore mainly done in the lower frequency band, as it is here that the highest reflections are expected. The frequency range selected for the reflection tests was 750 MHz to 3 GHz.

Att [dB]	Amp [dBm]	Phase [deg]	S/N
Freq: 2 GHz			
0	-40.50	-18.79	75
-10	-50.49	-21.67	65
-20	-60.46	-19.77	56
-30	-70.36	-22.51	49
-40	-80.47	-15.39	38
-50	-90	Noise	17
-60	-100	Noise	9
Freq: 5 GHz			
0	-53.33	54.79	63
-10	-63.26	47.93	53
-20	-73.27	52.64	45
-30	-83.97	46.5	32
-40	-93.45	61.69	22
-50	-102.7	Noise	15
-60	-114	Noise	Noise
Freq: 8.2 GHz			
0	-75.19	94.92	42
-10	-85.05	-108.5	31
-20	-95.14	100	23
-30	-105	Noise	12
-40	-112	Noise	6
Freq: 12.4 GHz			
0	-85.40	-88.85	31
-10	-95.90	-105.00	19
-20	-105	Noise	9
-30	-115	Noise	2

Table 3.5: NSI2000-software output: amplitude, phase and signal-to-noise readings during the stepped attenuation measurements

3.6.1 Probe structure reflections

Probe structure reflection errors are an unavoidable part of near-field scanning. This is due to the fact that the AUT and the probe are in close proximity to each other and a portion of the transmitted signal is reflected back from the probe and surrounding structures towards the transmit antenna. Yaghijian [24] describes the radiation that the probe receives as an "infinite series of rapidly decreasing terms". This implies that it is not only the direct signal that is received but in fact the direct signal with a sum of reflected signals, which all add up to what is ultimately received by the probe. This is illustrated in figure 3.25.

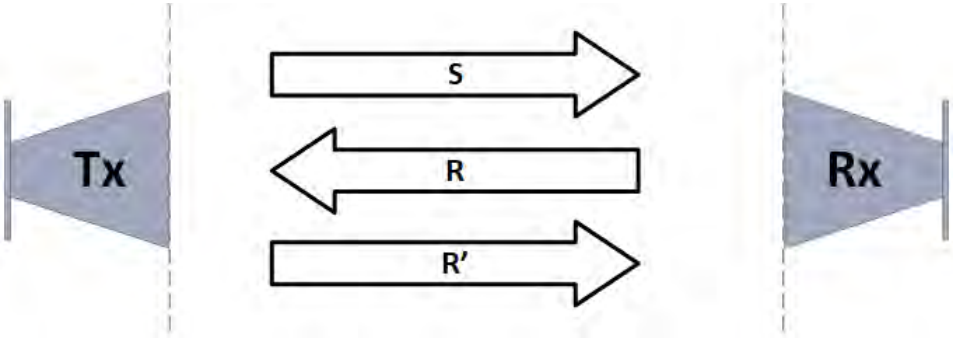

Figure 3.25: Multiple reflections, where S is the direct signal, R the reflected signal from the Rx-antenna and R' portion of the R that is reflected from the Tx-antenna

If these reflections are large enough, they will have an influence on the measurement itself, and therefore introduce an error in the calculated far-field pattern. The proposed method to measure these reflections, is to increase the separation distance between the AUT and the probe by steps of Δd and compare the measurements[10][3][30]. As a result of the increased distance, the phase of the direct signal changes by $k\Delta d$, but for the reflected signal that travels back and forth between the antennas the phase changes by $3k\Delta d$. The suggested step size for the procedure is a $\frac{1}{8}$ of a wavelength. If there is reflection between the antennas, it will become visible as a change in $|S21|$ as the separation distance increases.

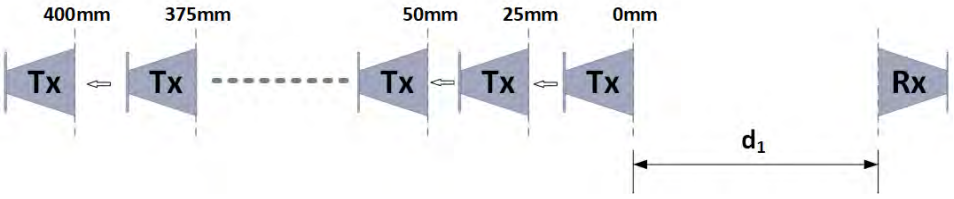

Figure 3.26: Multiple reflections measurement set-up

A cyclic amplitude response of $\frac{1}{2}\lambda$ is to be expected because if the antenna separation distance has increased by $\frac{1}{2}\lambda$, the primary signal, travelling in the forward direction, and the reflected signal, travelling in the opposite direction, is in phase and constructive interference will occur.

As illustrated in figure 3.26, the AUT was translated on the z-axis with a step size of 25 mm. The measurement was done in the region where the AUT is usually mounted when a SNF-scan is done. Therefore, this measurement gives a good indication of what the expected amplitude variation can be if the scanner is moved forward or backward on the z-axis.

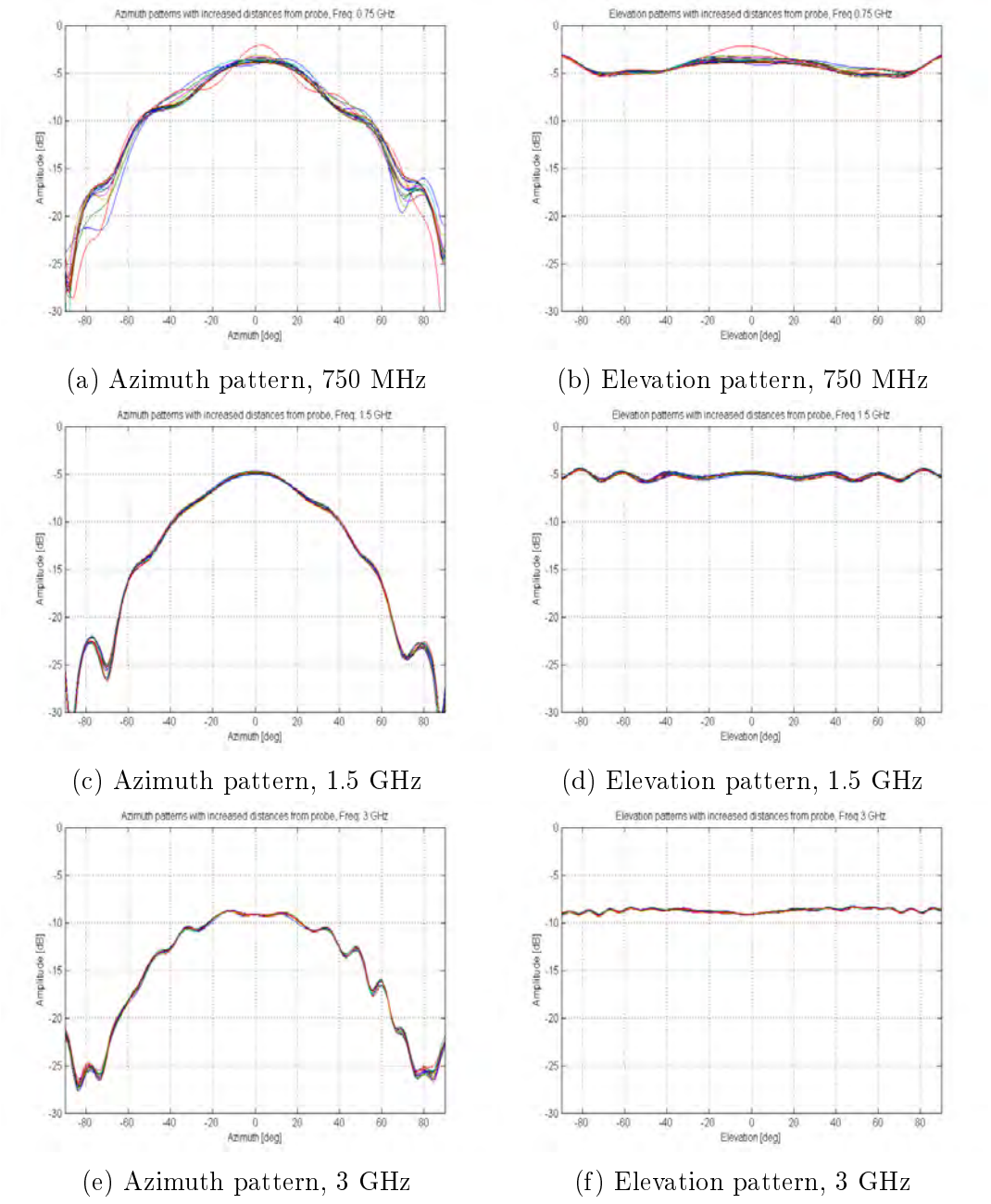

(a) Azimuth pattern, 750 MHz

(b) Elevation pattern, 750 MHz

(c) Azimuth pattern, 1.5 GHz

(d) Elevation pattern, 1.5 GHz

(e) Azimuth pattern, 3 GHz

(f) Elevation pattern, 3 GHz

Figure 3.27: Azimuth and elevation patterns of 750 MHz, 1.5 GHz and 3 GHz for an increased distance from the probe

Figure 3.27 displays the azimuth and elevation patterns of the SNF-scans done in different positions. The variation in the patterns can be observed, especially at 750 MHz, which is the lowest frequency.

In figure 3.28 the variation in amplitude at boresight is displayed as it changes with distance. From 1.5 GHz upward the $\frac{1}{2}\lambda$ cyclic response can be seen. At frequencies below 1.5 GHz, cyclic variation is not visible and

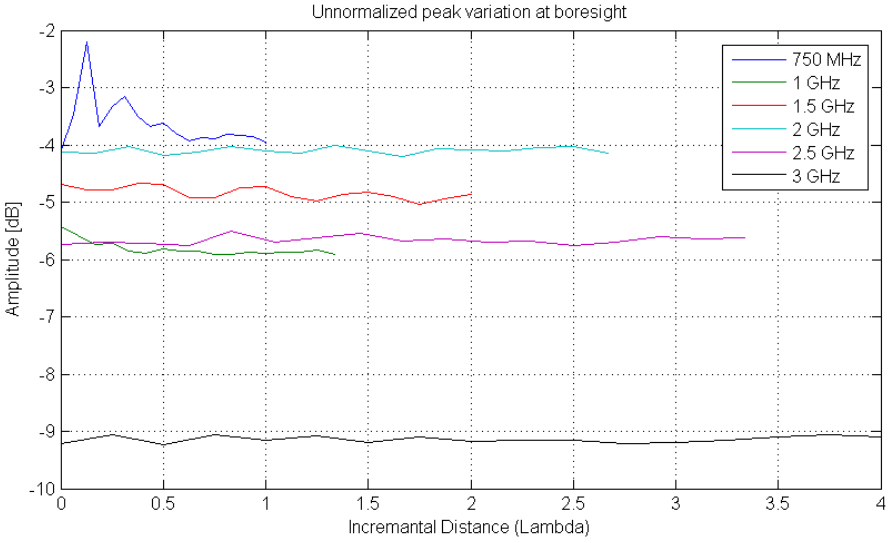

Figure 3.28: Amplitude variation of various frequencies over an incremental distance of 400 mm

at 750 MHz there is an amplitude value that is much larger than what is expected. This amplitude peak is a result of the close proximity of the two antennas to each other. This causes an undesired interaction between the probe and the AUT. The recommended separation distance [3] is 3λ to 5λ. This separation distance is necessary to minimise multiple reflections and to ensure that evanescent modes do not have an influence on the measurement. In this instance, the total separation distance at the 50 mm-position was 973 mm, which is less than 3λ at 750 MHz.

In figure 3.29 an in-depth look is taken at the amplitude variation at boresight as well as the amplitude variation at $\theta = 45°$ of the azimuth and elevation patterns. It confirms the observation that reflections are present, and that below 1.5 GHz large amplitude variations are more prominent than at frequencies from 1.5 GHz upwards.

The error-to-signal level was calculated by subtracting the two patterns with the minimum and maximum amplitude values at the angle of interest (figure 3.30). The error could therefore be determined and by using equation 2.3.7 the uncertainty was calculated. Table 3.6 displays the results across the selected frequency band at specific cuts and angles. It is interesting to note that in the azimuth pattern at 2 GHz at 45° the E/S-level is rather large compared to 0° and 45°. The reason for the irregularity is because the azimuth pattern's beamwidth is narrower than at the other frequencies and at 45° the slope is quite steep, the minimum pattern amplitude is -14.74 dB and although the error level is at -32.70 dB, the error-to-signal level is -17.96 which results in an uncertainty of 1.034 dB. This demonstrate that a small error can lead to a large uncertainty if it is compared to a signal with a small amplitude. It

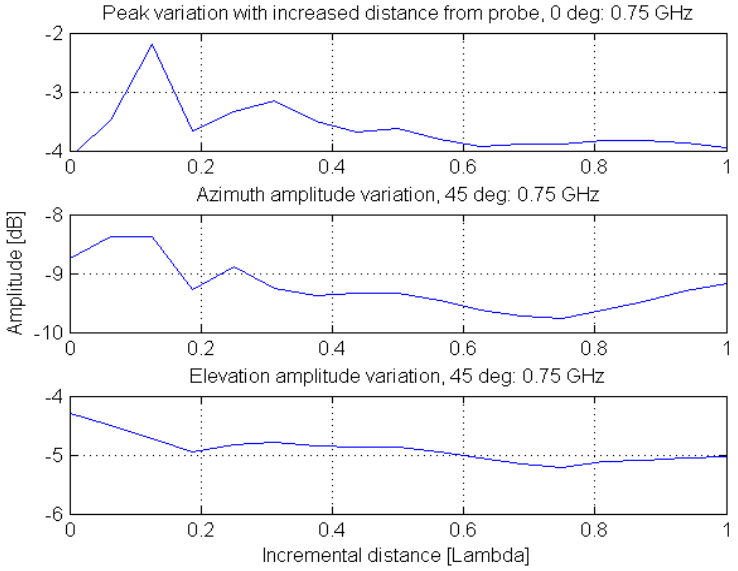

(a) Amplitude variation at boresight and 45°, frequency 750 MHz

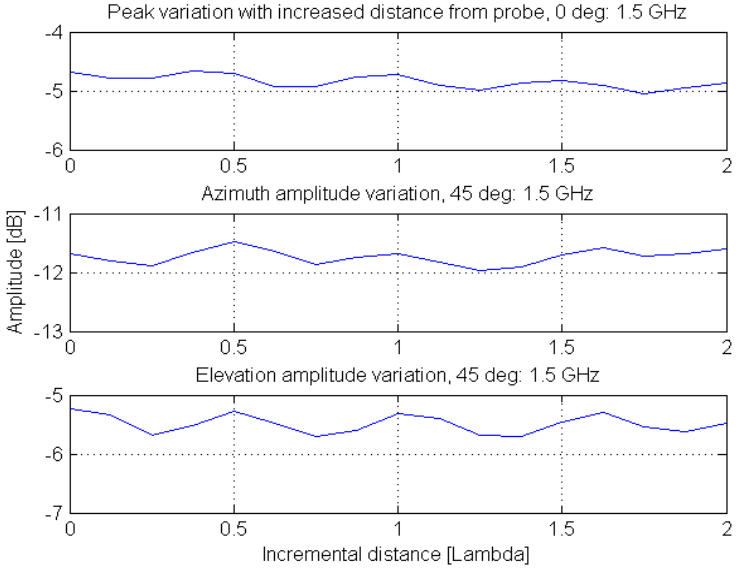

(b) Amplitude variation at boresight and 45°, frequency 1.5 GHz

Figure 3.29: Amplitude variation at 0° and 45°, measurements were done over a distance of 400 mm with increments of 25 mm

must be pointed out that although this uncertainty is only for a small angular range, the RMS-value (error) for the azimuth cut is -40.03 which would give an error-to-signal of -35.84 dB, which renders an uncertainty of 0.14 dB.

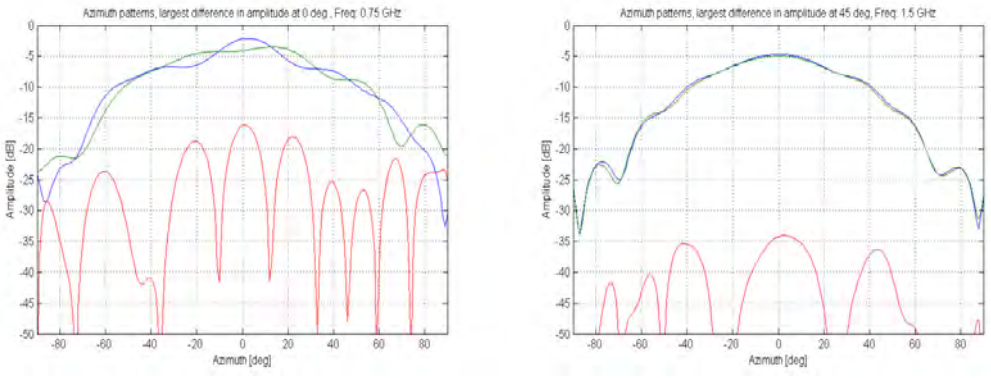

(a) Frequency, 750 MHz (b) Frequency, 1.5 GHz

Figure 3.30: The azimuth patterns with minimum and maximum amplitude at boresight. The difference between the patterns is also displayed.

Freq [GHz]	**Cut**	**Angle**	**E/S level [dB]**	**Uncertainty [dB]**
0.75	Az/El	0°	-12.13	1.92
0.75	Az	45°	-16.31	1.24
0.75	El	45°	-19.88	0.84
1.0	Az/El	0°	-24.44	0.51
1.0	Az	45°	-23.55	0.56
1.0	El	45°	-26.56	0.40
1.5	Az/El	0°	-27.06	0.38
1.5	Az	45°	-24.78	0.49
1.5	El	45°	-25.30	0.46
2.0	Az/El	0°	-33.06	0.19
2.0	Az	45°	-17.96	1.03
2.0	El	45°	-31.59	0.23
2.5	Az/El	0°	-30.62	0.25
2.5	Az	45°	-27.48	0.36
2.5	El	45°	-35.19	0.15
3.0	Az/El	0°	-34.51	0.16
3.0	Az	45°	-24.93	0.48
3.0	El	45°	-29.18	0.30

Table 3.6: Structure reflections

3.6.2 Chamber reflection

As mentioned above, one of the contributing factors to the frequency limit of the chamber is the absorber with which the chamber was lined. The absorption specified by Emerson & Cuming [29] at 750 MHz for the 8" material is -28 dB and for the 12" material, -35 dB. The floor, walls and roof are mainly covered

by the 12" material.

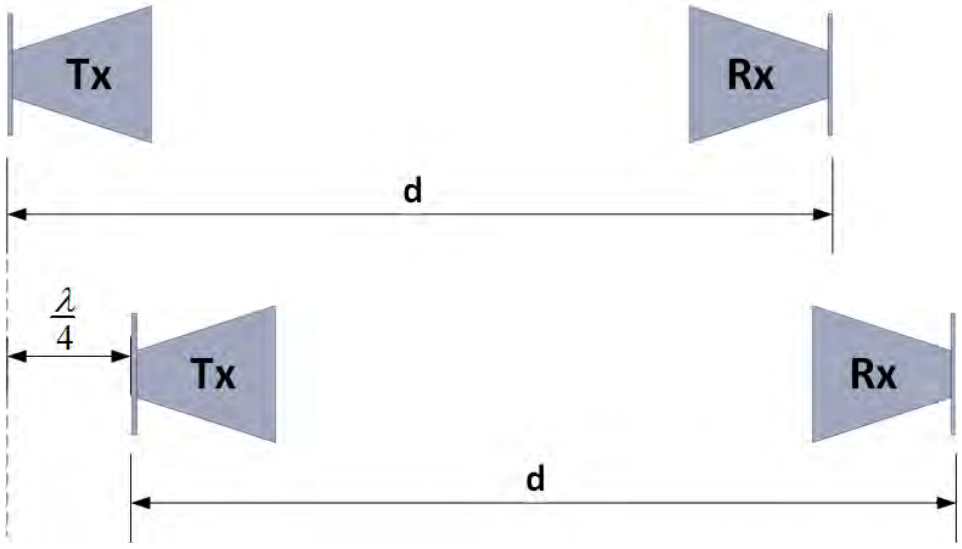

Figure 3.31: Chamber reflection measurements set-up

To test how much the chamber reflection is contributing to the measurement error, a method recommended by Parini [10] and which is also described in the IEEE recommendations [3] was used. The two antennas are simultaneously translated along the z-axis, with a suggested step size of $\frac{1}{4}\lambda$, as can be seen in figure 3.31. The AUT and the probe are translated simultaneously to eliminate the effect of the structure reflection and isolate only signals that are added as a result of the multipath effect.

Two approaches were taken to evaluate the results. Firstly the established technique was applied, whereby the calculated far-field patterns at the two positions were subtracted and the RMS-value was determined for that specific cut, as seen in figure 3.32.

The second approach was not just to subtract the cuts of interest from each other, but to subtract the whole three-dimensional far-field pattern of the first position from the three-dimension far-field pattern of the second position and calculate the RMS-value for difference over the whole sphere. The argument for doing this is that since the error is induced from the environment that encapsulates the set-up, it would make sense to take all the data points simultaneously into consideration and not only a single cut from the sphere.

Table 3.7 presents the results of the azimuth and the elevation cuts, as well as the RMS-value over the sphere. It is interesting to note that RMS-values are of the same order of magnitude. The uncertainty of the RMS-value calculated over the sphere is also included in the table.

The chamber reflections are considerably less than the structure reflections given in table 3.6. The results indicates that after 35 years of use, the absorbing material is still in good condition.

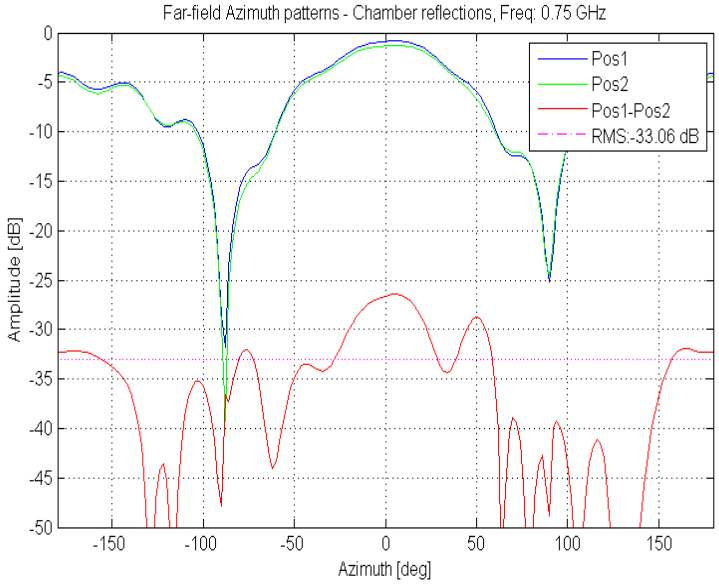

(a) Chamber reflection measurement, azimuth pattern, 750 MHz

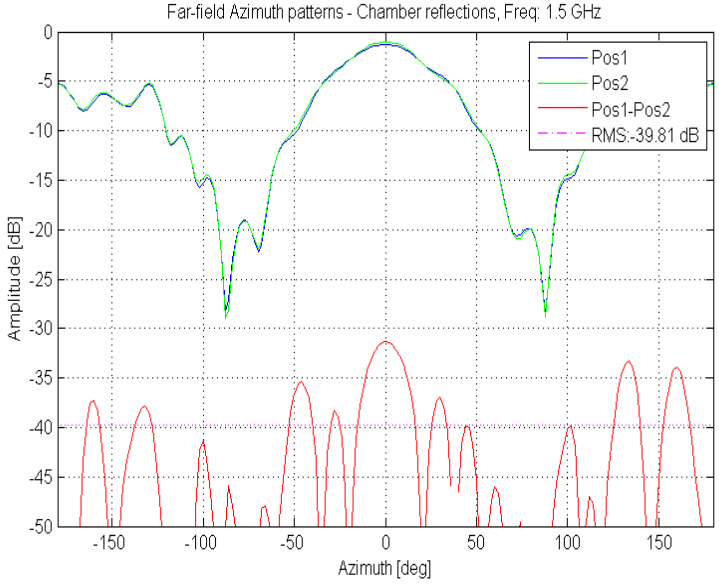

(b) Chamber reflection measurement, azimuth pattern, 1.5 GHz

Figure 3.32: Variation in the pattern with the AUT and the probe simultaneously translated by $\frac{1}{4}\lambda$

3.6.3 Environmental related errors - random amplitude/phase errors

Random errors occur as a result of noise in the electrical or mechanical systems [3]. To measure random error, repetitive measurements are done without any change to the system. The difference between the patterns is considered to be

Freq [GHz]	**Dist [mm]**	**RMS Az [dB]**	**RMS El [dB]**	**RMS Sphere [dB]**	**Uncertainty Sphere [dB]**
0.75	100	-33.06	-33.95	-34.38	0.16
1.0	75	-43.68	-46.66	-43.31	0.06
1.5	50	-39.81	-36.64	-37.58	0.11
2.0	37.5	-44.03	-44.53	-43.54	0.06
2.5	30	-42.65	-43.24	-39.55	0.09
3.0	25	-46.86	-46.82	-45.27	0.05

Table 3.7: Chamber reflections

due to random errors.

The calculated error would be considered the uncertainty floor of the range assessment because it would not be possible to measure uncertainty levels lower than what was measured during this particular test due to the favourable measurement conditions that existed [10].

From figure 3.33 it can be seen that the differences between measurements are extremely small and we can conclude that random errors do not have a large influence on the uncertainty of the measurement. When the results are considered, we can conclude that the uncertainty level increases as the frequency increases. At 2 GHz, the highest level of an uncertainty at boresight was 0.01 dB and 0.37 dB at a -30 dB sidelobe level. In the case of 5 GHz, the uncertainty levels rise to 0.033 dB at boresight and 1 dB at the -30 dB sidelobe levels.

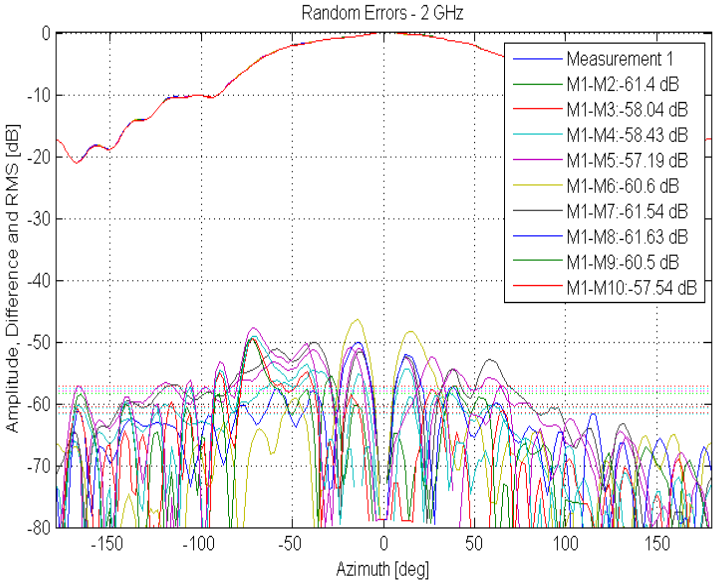

(a) Random Errors measurements, 2 MHz

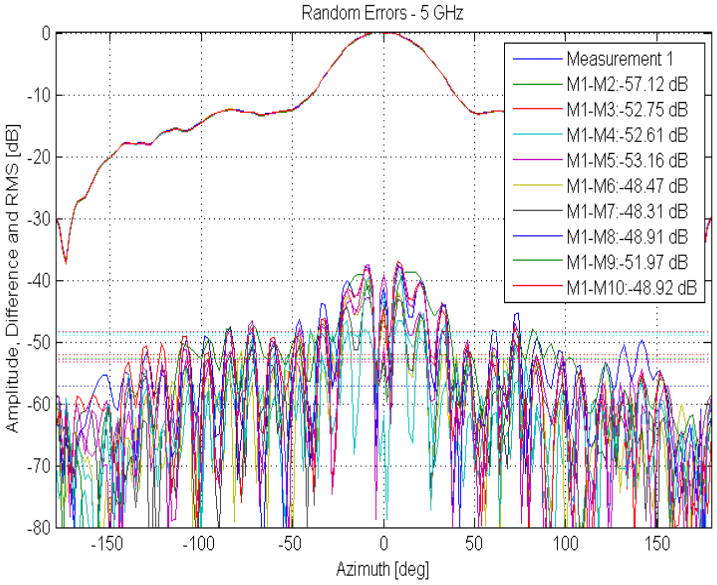

(b) Random Errors measurements, 5 MHz

Figure 3.33: Repetitive measurements to determine whether random errors are present in the system

Chapter 4

Conclusion

At the onset of this investigation, the idea was to have graphs which map the uncertainty over frequency for the US measuring facility. This, however, proved an impossible task since every error term of the NIST18-term error analysis proved unique at each frequency and some are negligible at high frequencies while others have an influence across the frequency range. The initial aim was adapted to the observation of trends at applicable frequencies or frequency ranges. These observations are listed below as a conclusion to the study.

Probe/Illuminator related errors

Probe pattern correction for SNF: It was proven with a measurement that the influence of the probe's pattern on the spherical near-field scan results is extremely small, especially on boresight. This is the case because the probes orientation towards the AUT does not change significantly when an SNF-scan is done. There is an influence on the sidelobe level of the pattern when a the NSI-RF-RGP10 probe is used because its beamwidth is much narrower than the OEWG-probe. Therefore, whenever there is an option to use the OEWG-probe instead of the wideband horn, preference should be given to the OEWG-probe.

Probe polarisation purity: By means of theoretical analysis, it was shown that the probe polarisation purity has only an influence on the cross-polarisation patterns. It is important to take note that when OEWG-probes are used, no probe cross-polarization correction is done by the NSI2000-software. It does, however, have such a small influence on the measurements that this is by no means an oversight from the software developers.

Probe alignment: The two subsections of probe alignment - probe tilt misalignment and probe axial misalignment have also very little influence on the co-polarization pattern results done by a spherical near-field scan. This is directly related to the wide beamwidth of probes used. This error has the biggest influence on the cross-polarisation patterns.

Mechanical related errors

The Hansen study results were used to evaluate how much mechanical misalignment contributes to measurement uncertainty.

Spherical scanner alignment: It can be concluded from the Hansen study that small errors in the spherical scanner's alignment, have an insignificant influence on the uncertainty. The exception is that the ϕ-axis alignment is more sensitive and changes in the sidelobe level can be expected.

Polarisation-stage alignment: The polarisation-stage misalignment would give the same errors as probe misalignment because it is essentially the same thing and would have the same effect on the measurement. Therefore the conclusion can be made that if the polarisation-stage is misaligned, it has only an influence on the cross-polarization patterns.

Inter-stage pointing vector alignment: On the basis of the Hansen study it can be concluded that when the ϕ-axis and the pol-axis are not aligned, it influences the beamwidth as well as the sidelobe level. Considering all the possible mechanical errors that were looked at, the inter-stage pointing vector could have potentially the biggest influence on the sidelobe levels.

Absolute power level related errors

Gain standard: This error term has not been considered since at the US measuring facility absolute gain is measured and not comparative gain to which this term applies.

Normalisation constant: Amplitude stability is described by the normalisation constant. This potential error is caused by amplitude drift, repeatability in connections made and receiver linearity. Six measurements were done with only one that differs significantly from the others. The effect of this outlier causes uncertainty of 0.3 dB on the absolute power level. There is no need to consider the effect on the sidelobe level since we are dealing with the absolute power level.

Impedance mismatch error: As was the case with the gain standard errors, errors from an impedance mismatch also do not apply to absolute gain measurements done at the US measuring facility and are therefore not considered.

Processing related errors

Aliasing: With correctly defined measurement parameters, aliasing does not occur. It, therefore, has no influence on measurement uncertainty.

Measurement area truncation: Measurement area truncation is not applicable when a full spherical scan is done. If for some reason it is necessary to truncate the scan area, care should be taken that enough energy is captured to avoid errors due to area truncation.

RF sub-system

Receiver amplitude linearity: It was established that the proposed test for the receiver linearity is not valid in all circumstances because at higher frequencies the absolute amplitude of the patterns is close to the noise floor which results in a diminished dynamic range. This adds noise to the pattern with the lower amplitude.

However, where the frequencies were low enough and the dynamic range did not dominate the results, it can be concluded that the receiver amplitude is linear and does not have a significant influence on the results.

System phase error: During the investigation, it was established that near- to far-field transformations is extremely sensitive to phase changes. It is therefore important to implement precautions to keep the phase as stable as possible during the measurements.

Leakage and crosstalk: The leakage and crosstalk are extremely small and it can be concluded that as long as all the connections are secure and the rotary joints and cables are in good working order, leakage and crosstalk add no uncertainty to the results.

Receiver dynamic range: Dynamic range is dependent on the operating frequency, antenna gain, loss in the system and antenna separation distance. It is obvious from the measurements that above 8.2 GHz it becomes necessary to add an amplifier to the system to increase the dynamic range. It was also noted that the phase becomes unstable with less attenuation than the amplitude. Phase instability is for that reason the dominant limiting factor to dynamic range.

Environmental related errors

Multiple reflections: It is very clear that multiple reflections between the structures, on which the antennas are mounted, is the largest contributor to measurement uncertainty for AUT's with operating frequencies below 1.5 GHz. There is a partial remedy for the problem and that is to move the structures further apart for the lower frequency measurements. This will limit the reflections between the structures.

Chamber reflections: As was the case with multiple structure reflections, the rise in uncertainty is associated with frequencies below 1.5 GHz. Unfortunately, there is not an easy solution as was the case with structure reflections. The error and related uncertainty are, however, significantly less than structure reflections.

Random amplitude/phase errors: The random errors in a system are of great importance because they represent the minimum level of uncertainty in the system. The random errors in the measuring facility are very low and not of any concern. It was, however, seen that the uncertainty relating to

random errors increases as the frequency increases.

To summarise, it is possible to make accurate measurements at the measuring facility with the equipment in its current operational state. Most errors in the measuring facility can be avoided if the set-up is done very carefully because set-up errors can be avoided with meticulous preparation and uncertainty can be minimized. Below 1.5 GHz the chamber structure reflections pose a problem and it might be worthwhile to increase the separation distance between the structures onto which the probe and the AUT are mounted. In conclusion, it is possible to measure reliable patterns above 1.5 GHz with the spherical near-field scanner at the University of Stellenbosch.

Bibliography

[1] J. H. Cloete, W. M. Stassen, and D. A. G. Morgan, "Antenna radiation patterns from cylindrical near-field measurements," *South African Institute of Electrical Engineers*, vol. 78, no. 2, pp. 46–52, December 1987.

[2] C. A. Balanis, *Antenna Theory Analysis and Design, Third edition.* Hoboken, New Jersey, USA: Wiley, 2005.

[3] "IEEE Recommended Practice for Near-Field Antenna Measurements," IEEE, Tech. Rep. 1720-2012, 2012.

[4] J. E. Hansen, *Spherical Near-Field Antenna Measurements.* London, UK: IET, 2008.

[5] A. D. Yaghjian, "An overview of near-field antenna measurements," *IEEE Transactions on Antennas and Propagation*, vol. 34, no. 1, pp. 30–45, January 1986.

[6] J. H. Cloete, L. J. du Toit, and W. I. George, "Linear near-field measurements on a slotted waveguide array," *SAIEE Joint Symposium on Antennas and Propagation and Microwave Theory and Techniques*, August 1986.

[7] J. H. Cloete and P. W. van der Walt, "Antenna and microwave research at Stellenbosch," *South African Journal of Science*, vol. 84, pp. 864–865, November/December 1988.

[8] C. F. du Toit, J. Solms, K. D. Palmer, and J. H. Cloete, "Recent research progress on cylindrical near-field antenna measurements at the University of Stellenbosch," *Proceedings of Joint Symposium on AP/MTT*, August 1988.

[9] D. M. P. Smith, D. B. Davidson, A. Bester, and J. Andriambeloson, "Modernising, upgrading and recommissioning the indoor antenna range at Stellenbosch University," *South African Institute of Electrical Engineers*, vol. 107, pp. 4–16, March 2016.

[10] C. Parini, S. Gregson, J. McCormick, and D. J. J. van Rensburg, *Theory and Practice of Modern Antenna Range Measurements.* London, UK: IET, 2015.

[11] D. Slater, *Near-Field Antenna Measurements.* Norwood, Massachusetts, USA: Artech House, 1991.

[12] "Antenna Measurement Range Characterization and Compensation," Georgia Institute of Technology, School of Electrical and Computer Engineering, Atlanta, Georgia, USA, Tech. Rep.

[13] A. C. Newell and Z. Newbold, "Reducing measurement time and estimated uncertainties for the NIST 18 term error technique," *Antenna Measurement Techniques Association Annual Symposium Proceedings*, pp. 138–143, October 2006.

[14] A. Newell and G. Hindman, "Antenna pattern comparison using pattern subtraction and statistical Analysis," *EuCAP*, pp. 2537–2540, 2011.

[15] "NSI 2000, Software Operating Manual (Nearfield Edition)," NSI-MI Technologies, Torrance, USA, Tech. Rep. SOM-NSI2000-V4, Rev F, August 2011.

[16] "IEEE Standard for Definitions of Terms for Antennas," IEEE, Tech. Rep. 145-2013, 2013.

[17] D. M. Pozar, *Microwave Engineering.* Hoboken, New Jersey, USA: John Wiley & Sons, Inc., 2012.

[18] "IEEE Standard Test Procedure for Antennas," IEEE, Tech. Rep. 149-1979, 1979.

[19] D. E. Baker, "Development and evaluation of the 500 m ground-reflection antenna test range of the CSIR, Pretoria, South Africa," *AMTA Proceedings*, October 1988.

[20] R. E. Collin and F. J. Zucker, *Antenna Theory Part I.* New York, USA: McGraw-Hill, 1969, p. 578.

[21] F. Jensen and A. Frandsen, "On the number of modes in spherical wave expansions," *AMTA 26th Annual Meeting and Symposium*, pp. 489–494, October 2004.

[22] A. C. Newell, J. Guerrieri, and K. MacReynolds, "Methods to estimate and reduce leakage bias errors in planar near-field antenna measurements," *AMTA Annual Meeting and Symposium*, 2002.

[23] "Keysight 2-Port PNA-X Network Analyzer Data Sheet and Technical Specification," Keysight Technologies, Santa Rosa, USA, Tech. Rep. N5242-90007, February 2017.

[24] "Upper-Bound Errors in Far-Field Antenna Parameters Determined from Planar Near-Field Measurements. Part 1," National Bureau of Standards, Boulder, Colorado, USA, Tech. Rep., October 1975.

[25] A. C. Newell, "Error Analysis Techniques for Planar Near-Field Measurements," *IEEE Transactions on Antennas and Propagation*, vol. 36, no. 6, pp. 754–768, June 1988.

[26] P. Pelland, G. Hindman, and D. J. van Rensburg, "Spherical near-field alignment sensitivity for polar and equatorial antenna measurement," *AMTA Proceedings*, November 1998.

[27] A. C. Newell and G. Hindman, "The alignment of a spherical near-field rotator using electrical measurements," *AMTA Proceedings*, June 1998.

[28] G. Hindman and A. C. Newell, "Reflection suppression in a large spherical near-field range," *AMTA 27th Annual Meeting and Symposium*, October 2005.

[29] "ECCOSORB VHP-NRL Specification Sheet," EC Anechoic Chambers, Belgium, Tech. Rep. V01/2, April 2010.

[30] Z. Newbold, B. Williams, and A. Newell, "Identifying Pointing Errors for the NIST 18 Term Error Technique," L-3 Communications, CS-W, Salt Lake City, Utah, USA, Tech. Rep.